Vol.2 | No 2
2024

IJONFEST

International Journal of New Findings in Engineering, Science and Technology

e-ISSN: 3023-4379

IJONFEST

INTERNATIONAL JOURNAL OF NEW FINDINGS IN ENGINEERING, SCIENCE AND TECHNOLOGY (IJONFEST)

IJONFEST

EDITORIAL BOARD (FIELD EDITORS)

IJONFEST

ADVISORY BOARD

IJONFEST

IJONFEST

2024
Vol.2
No.2

TABLE OF CONTENT

IJONFEST

IJONFEST

FROM EDITOR

Dear researchers,

We are happy to be publishing the first issue of the International Journal of New Findings in Engineering, Science and Technology (IJONFEST). In this regard, we would like to thank both our authors who prepared and submitted their scientific studies, which require intensive labor, and our valuable referees, who put forward their experiences, knowledge and dedication, without any other motivating factor other than the academic responsibility and the happiness of contributing to the field, in order to turn these studies into a more qualified and scientific study. In addition, I would like to thank all the members of our jounal team, who, as the third part of the trivet, ensure that the articles meet the relevant readership.

This issue (Vol.2, No.2) includes seven research and one review articles. Considering the topics of the articles published in this issue, it is obvious that our journal complies with the principle of subject diversity, which is one of our publishing principles.

We hope that our current new issue will contribute to the relevant areas and look forward to your valuable researches/articles to be published in the next issue of our journal.

Assoc. Prof. Dr. Redvan Ghasemlounia
Editor-in-Chief
International Journal of New Findings in Engineering, Science and Technology (IJONFEST)

September 2024

IJONFEST

September 2024, Vol:2, Issue:2

International Journal of New Findings in Engineering, Science and Technology

journal homepage: *https://ijonfest.gedik.edu.tr/*

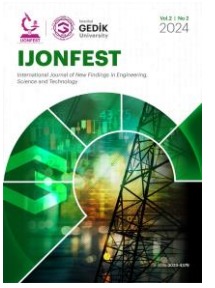

Output Parameters Estimation in A Broadband Substrate Integrated Waveguide Two- Channel T- Type Power Divider Using Adaptive Network-Based Fuzzy Inference System

Vala Tadshvigh [a], Mesut Kartal [a] , Mahmood Abbasi Layegh [b*] , Aran Abbasi Layegh [c]

[a] *Department of Electronics and Communication Engineering, Istanbul Technical University, Istanbul, Turkey*
[b] *Electrical Engineering Department, Urmia University, Urmia, Iran*
[c] *Department of Electrical Engineering, Tabriz University, Iran*

Abstract

A novel substrate integrated waveguide (SIW), power divider is proposed. It consists of two channels made by SIW with the same length and width. The bandwidth of 5GHz to 14 GHz is studied here. The propagation constant of the output signals can be adjusted by only four vias in the middle of the output arms. Hence, the position of four metalized inductive vias used here are chosen as a variable ranging from 0 mm to 1 mm and they are shifted in four different positions: up, down, right and left sides. Our studies reveal that moving the vias up and down has no effects on the resonant frequency and other related parameters. However, the values of output powers and phases are changed as the vias are shifted to the right or left sides. Conventionally, artificial neural networks are tested out to obtain resonant frequency, output powers and output phases. However, they do not lead to a promising result. Finally, adaptive network-based fuzzy inference system (ANFIS) is applied in three different steps to obtain resonant frequency, output powers and output phases. As can be seen, ANFIS can determine S parameters as output signals with a high accuracy when the resonant frequency and phases of output ports are given and the average error of less than 10% can be achieved. Nevertheless, the estimation of output phases or resonant frequency results in less satisfactory results.

Keywords: Substrate integrated waveguide, Power divider, Artificial neural networks, Adaptive network-based fuzzy inference system.

1. INTRODUCTION

Creating microwave gadgets with superior quality and affordable pricing is imperative for emerging wireless communication networks. Essential elements like power dividers find extensive utility across multiple applications within microwave integrated circuits (MIC), including balanced mixers, amplifiers, phase shifters, and feed networks within antenna arrays. Significant advancements, optimizations, and theoretical breakthroughs have evolved over numerous decades [1]-[6]. Although numerous designs of N-way planar power dividers have undergone scrutiny [2]-[4], issues persist regarding unequal power distribution and accommodating dual-band applications.

Since then, a plethora of innovative methodologies have emerged to advance power dividers, encompassing dual-band performance [7], [8], bandwidth augmentation [9], and high-power utilization [10], [11]. Recent years have

https://doi.org/10.61150/ijonfest.2024020201

witnessed the emergence of numerous novel dual-band distributed-circuit power dividers, boasting both equal [13]-[15] and unequal power distributions [17], [18]. However, a predominant limitation of these dual-band power dividers lies in their restricted two-way configuration. To achieve optimal port matching and isolation across a wide frequency range, a novel coupled-line tunable Wilkinson power divider has been introduced [19]. Similarly, a groundbreaking filtering power divider boasting a wide stop band has been conceived, implementing a discriminating coupling scheme in both input and output coupling regions [20]. Reference [21] introduces an innovative substrate integrated waveguide (SIW) phase shifter, featuring phase channels crafted from SIW with uniform length but varied width. This configuration enables adjustment of the propagation constant of output signals solely by modifying the width of output arms. Previous studies have demonstrated the efficacy of Artificial Neural Networks (ANNs) in computing diverse parameters of microstrip antennas, including triangular, rectangular, and circular shapes, as well as pyramidal horn antennas [22-29]. References [30-33] utilize ANNs to accurately determine the resonant frequency of rectangular Microstrip Antennas (MSAs). Additionally, Guney and Sarikaya [34-37] successfully employ Adaptive Neuro-Fuzzy Inference System (ANFIS) to compute various parameters of rectangular, circular, and triangular MSAs. In [38], they apply the Adaptive Neuro-Fuzzy Inference System to compute the resonant frequency of electrically thin and thick rectangular microstrip antennas. ANFIS exhibits utility in modeling nonlinear functions and time series [39-40].

This paper introduces a novel substrate integrated waveguide (SIW) two-channel T-type power divider. The divider comprises two SIW channels of identical length and width. The positioning of four metalized inductive vias along the middle of the output arms serves as a variable, allowing for shifting in various directions. The study evaluates the output powers and phases for all conceivable positions of the vias and frequency variations. Notably, altering the vias' vertical position demonstrates no impact on resonant frequency, output powers, or phases. Conversely, horizontal displacement of the vias affects these parameters significantly. Subsequently, artificial neural networks are employed to predict operational frequency, output powers, and phases, albeit without precise estimations. Finally, the paper discusses simulated and measured results, concluding that the adaptive neuro-fuzzy inference system (ANFIS) represents the most suitable machine learning algorithm for such power dividers.

2. ANALYSIS AND DESIGN

Figure 1 illustrates the configuration of the envisioned power divider. The substrate integrated waveguide (SIW) is a quasi-rectangular waveguide established through periodic via-hole connections between two metal layers. In the TE mode (predominant mode), SIW behaves comparably to a traditional rectangular waveguide, exhibiting minimal leakage losses. Consequently, SIW and its analogous dielectric field waveguide possess identical TE10 mode cut-off frequencies, expressed as:

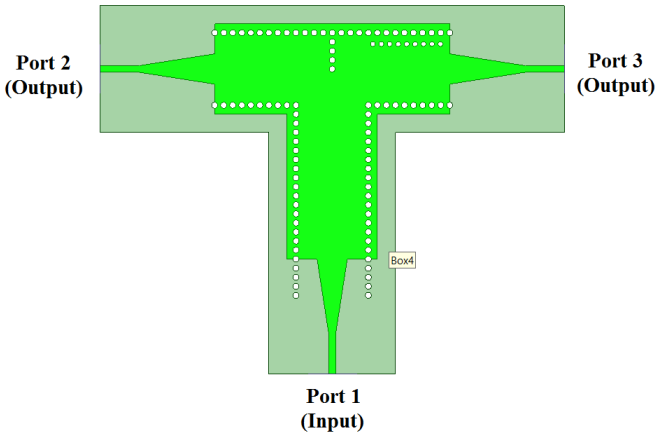

Figure 1. Structure of power divider.

$$f_c = \frac{1}{2a\sqrt{\mu\varepsilon}} \quad (1)$$

Where "a" represents the width of the rectangular waveguide equivalent to SIW, μ and ϵ denote the permittivity and permeability of said equivalent rectangular waveguide. The fundamental characteristics of SIW are approximately given as follows:

$$a = A - \frac{D^2}{0.95P} \quad (2)$$

Where a is the width of the equivalent rectangular waveguide, A is the width of SIW, D is the diameter of metalized via holes and P is the pitch between adjacent via holes as shown in figure 2.

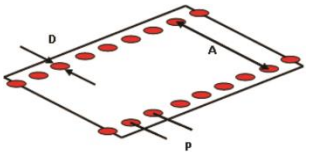

Figure 2. Rectangular waveguide integrated into a substrate.

2.1 T- Type SIW power divide with equal outputs

Substrate integrated waveguide T- type power dividers are usually appropriate for equal power division because they are symmetric and have a typical structure.

Four metalized inductive vias have been added centrally across from port 1 (input) to split the input signals equally between two output channels. Furthermore, centrally located vias act as inductive matching posts to nullify the effect of the T-junction capacitance. Hence, lower return loss can be achieved in the input. The position of these four inductive vias has an important effect in return loss and transition coefficients of the outputs. The output arms have the same width and length. Thus, the propagation constant and the phase of the output signals are expected to be the same.

The power divider design is etched onto a Rogers 4003 substrate with εr =3.55, tanδ =0.0027 featuring a substrate layer thickness of 0.508mm. At the operation frequency, the transmission coefficients at the outputs approach -3dB, accompanied by commendable return loss. Refer to figure 3 and Table I for visual and tabulated representations of the proposed power divider, respectively.

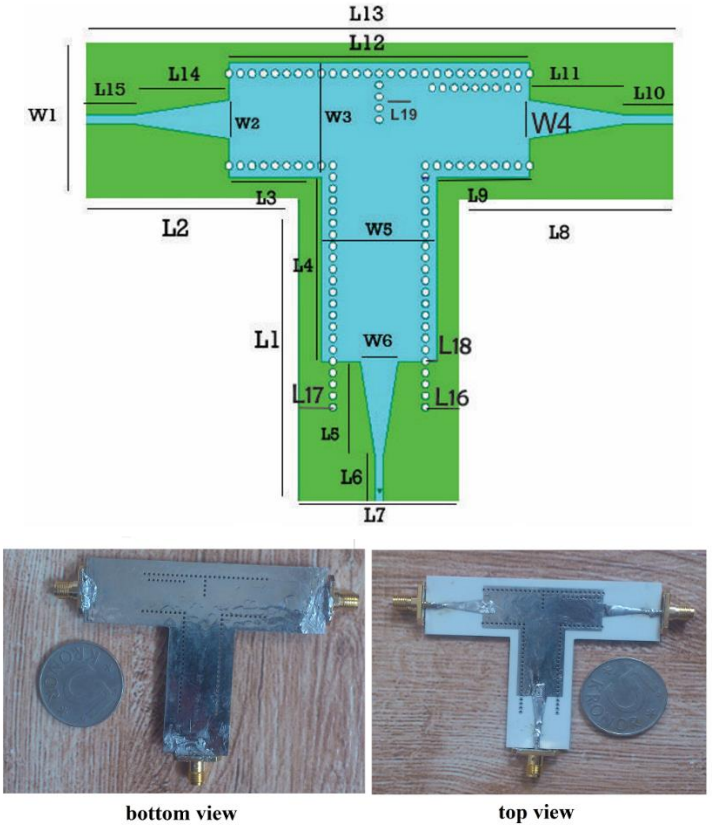

Figure 3. Geometry of the power divider.

Furthermore, the dimensions of the proposed power divider are given in details in Table 1.

Table 1. Dimensions of the proposed power divider (mm)

Parameter	mm	Parameter	mm	Parameter	mm
L1	40	L2	28	L3	12
L4	24	L5	12.5	L6	6.5
L7	21	L8	28	L9	12
L10	6.5	L11	12.5	L12	39
L13	39	L14	12.5	L15	6.5
L16	4.5	L17	4.5	L18	1.5
L19	k	W4	5	W1	21
W2	5	W3	15	W5	5

Simulation results for the prototype substrate integrated waveguide power divider are shown in figure 4. According to figure 4.(a) representing the return loss the bandwidth of 4.68 GHz is obtained from the frequency of 7.68 to 12.36. figure 4(b) illustrates that for equal signal outputs transmission coefficients for port 2 and port 3 occur at the same operation frequency. Meanwhile, figure 4.(c) shows S- parameters at the operating bandwidth.

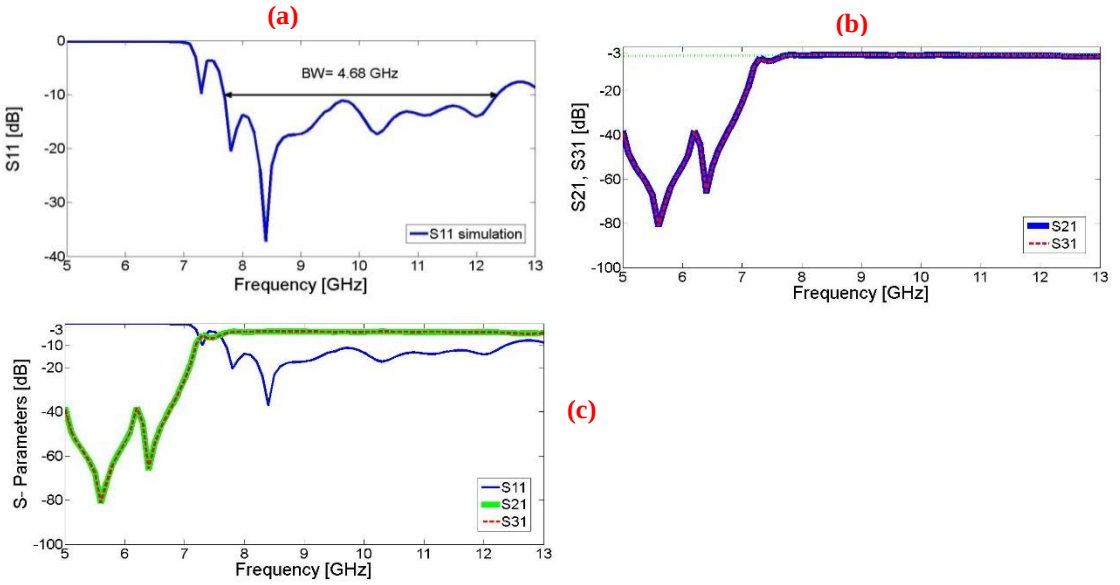

Figure 4. Simulation results for the return loss of SIW power divider (a) transmission coefficients (b) S-parameters of SIW power divider.

In figure 5, the results of both simulation and measurement of S-parameters for the whole ports are shown. It is noticeable that the simulation results of two output channels are similar.

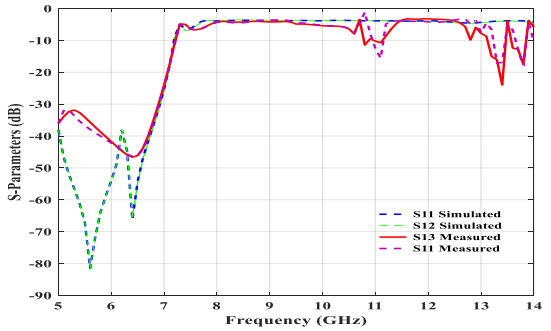

Figure 5. Results of both simulation and measurement of S-parameters for the whole ports

2.2 T- Type Unequal Power divider SIW

After optimizing the results of simulation using HFSS software, the appropriate parameters of the structure can be obtained to make desired power divider. With changing the parameter of L19= k (changing the position of central vias to left or right side) different values of power division are obtained. It is necessary that for the prototype, equal power division be applied. The values of (P) and (D) for these 4 vias are equal to 1.5 mm and 1 mm respectively.

Different values of S21 and S31 can be obtained by changing the positions of central vias to left or right hand as shown in table 2. According to table 2, when the position of central vias (L19) is shifted with the increase of 0.1 in each steps, output powers will consequently be unequal.

Table 2. S21 and S31 values for different positions

Position change (mm)	S31 (dB)	S21 (dB)	Position change (mm)	S31 (dB)	S21 (dB)
0.1	-3.6	-4	0.6	-2.8	-0.5
0.2	-3.4	-402	0.7	-2.6	-5.28
0.3	-3.3	-4.4	0.8	-2.5	-5.53
0.4	-3.16	-4.6	0.9	-2.4	-5.78
0.5	-2.9	-4.87	1	-2.3	-5.93

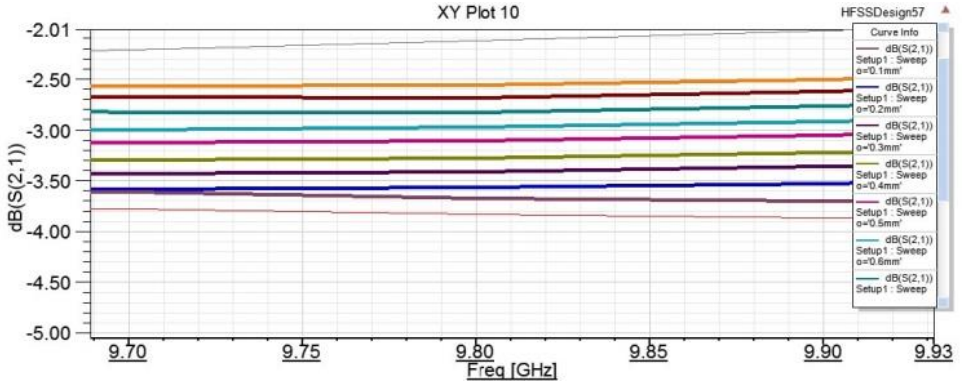

Figure 6. The value of S21 for different positions of SIW power divider

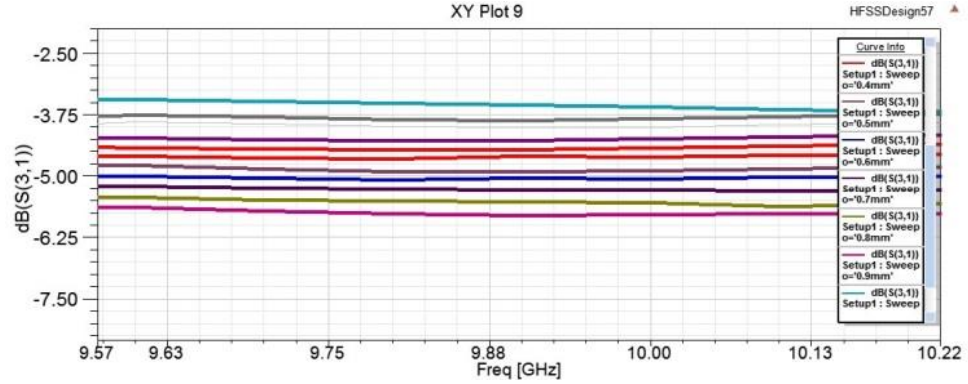

Figure 7. The value of S31 for different positions of SIW power divider

Figure 6 and figure 7 depict different values of S21 and S31 for different positions respectively. In the case that the position of central vias is shifted 1 millimeter, the value of power division in port 2 will be twice as much as that in port 3. Table 2 corroborates this matter. Figure 8 and figure 9 also show different values of power and phase outputs in port 3.

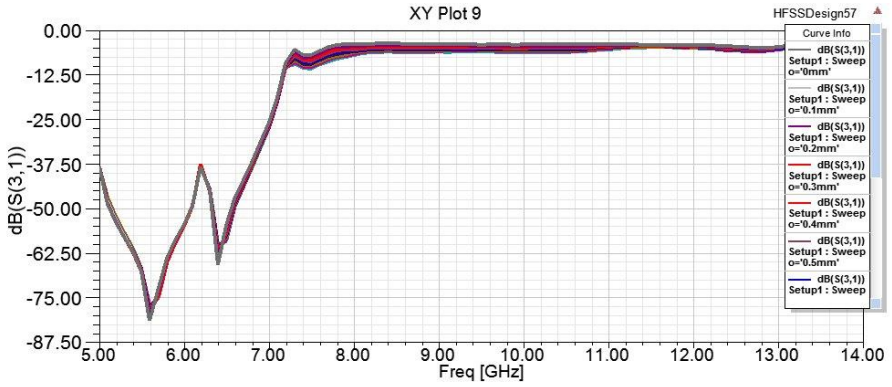

Figure 8. Output power of port 3 based on different positions of vias ranging from 5GHz to above 13 GHz

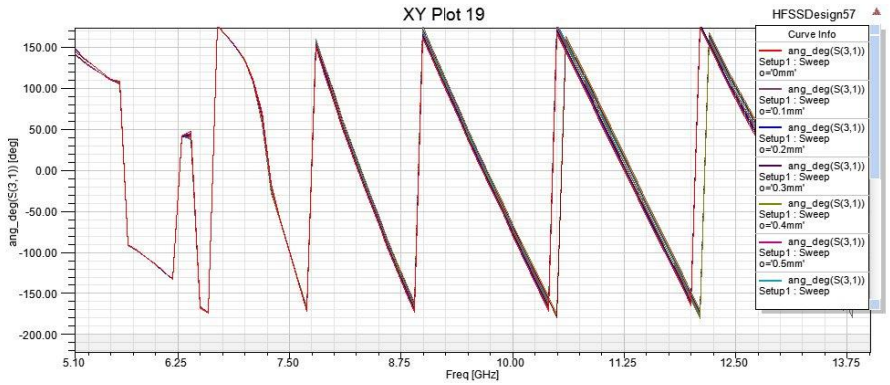

Figure 9. Output phase of port 3 based on different positions of vias ranging from 5GHz to above 13 GHz

The main purpose here is to predict the main parameters of the power divider such as resonant frequency, S-parameters and the phases of two outputs using machine algorithms based on neural networks. This study is carried out in three different steps:

a) The prediction of resonant frequency when two output powers and two output phases of the power divider are available. In addition, the position of vias is varied between 0 mm and 1mm.

b) The prediction of S21 and S31 when resonant frequency and phases of two outputs are given and the position of vias is changed between 0mm and 1mm.

c) The prediction of φ21, φ31 when resonant frequency and powers of the two outputs are given and the position of vias is changed between 0 mm and 1mm.

In the present work, artificial neural networks were employed to predict such parameters. Surprisingly, they had a very weak and unreliable performance in proceeding the process. Moreover, as can be seen in figures 10, 11 and 12, artificial neural networks represent a significant error in the recognition of the aforementioned outputs.

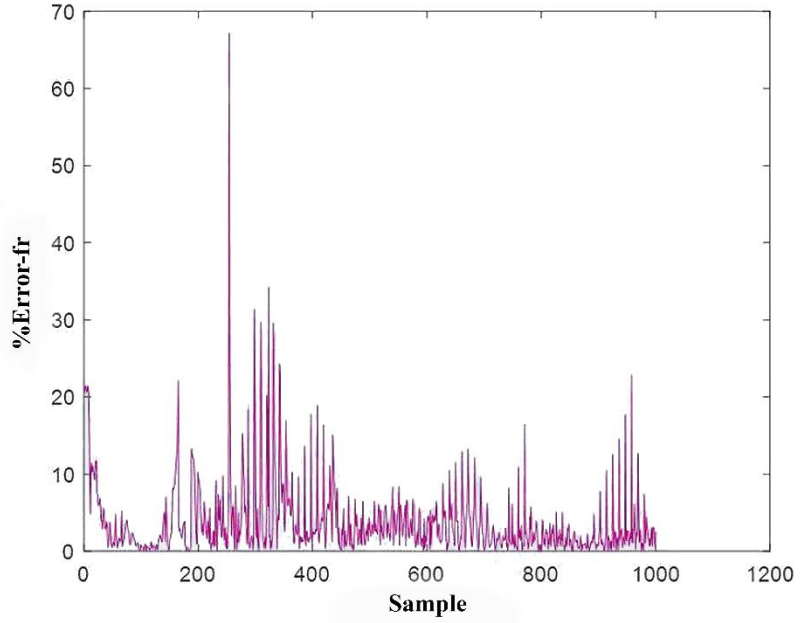

Figure 10. Error percentage of frequency estimation when S21, S31, φ21 are φ31are given as inputs.

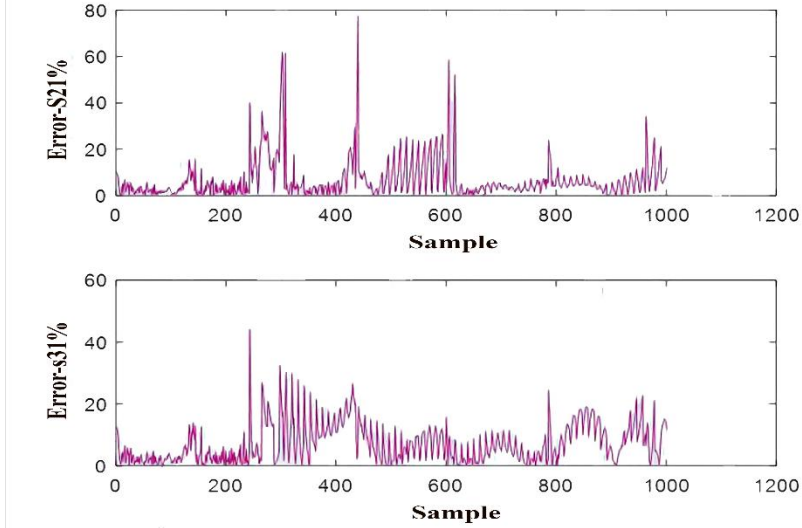

Figure 11. Error percentage of power estimation when φ21 are φ31 and resonant frequency are given as inputs

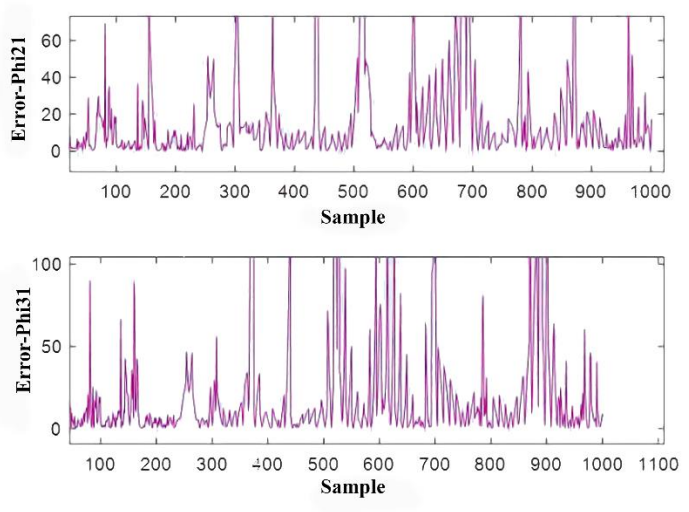

Figure 12. Error percentage of phase estimation when S21, S31 and resonant frequency are given as inputs.

2.3 Adaptive neuro fuzzy inference system

Fuzzy inference systems are alternatively referred to as fuzzy-rule-based systems, fuzzy models, fuzzy associative memories (FAM), or fuzzy controllers in controller applications. Fundamentally, a fuzzy inference system comprises five functional blocks, as depicted in Figure 13.

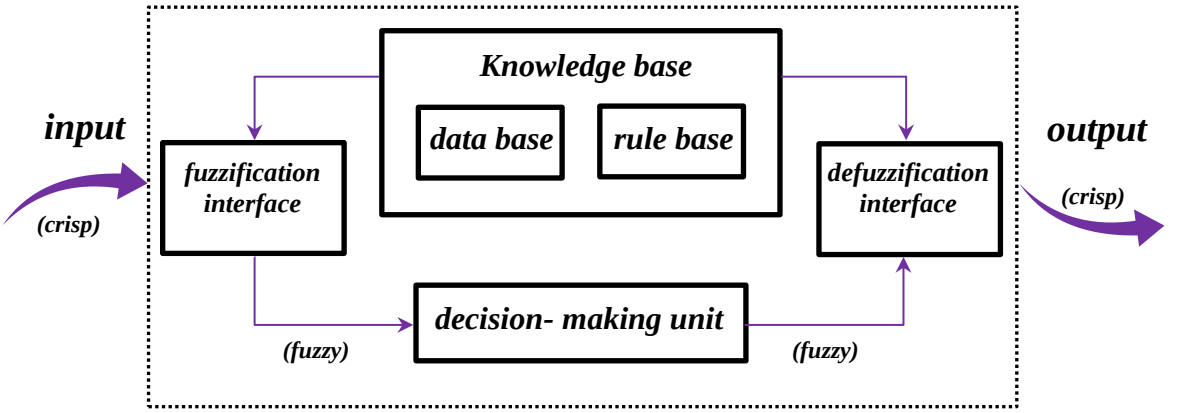

Figure 13. A fuzzy inference system.

- A rule base housing a set of fuzzy if-then rules.
- A database specifying the membership functions of the fuzzy sets utilized in the fuzzy rules.
- A decision-making unit executing the inference operations based on the rules.
- A fuzzification interface converting crisp inputs into degrees of match with linguistic values.
- A defuzzification interface converting the fuzzy outputs of the inference into a crisp output.

Typically, the rule base and the database are commonly referred to collectively as the knowledge base. The process of fuzzy reasoning in fuzzy inference systems involves the following steps:

1- Assessing the input variables against the membership functions on the premise section to derive the membership values (or compatibility measures) for each linguistic label. This stage is frequently termed fuzzification.

2- Merging the membership values on the premise section using a specific T-norm operator, typically multiplication or min., to determine the firing strength (weight) of each rule.

3- Producing the qualified consequent (either fuzzy or crisp) for each rule based on the firing strength.
4- Aggregating the qualified consequents to yield a crisp output. This process is known as defuzzification.

The ANFIS model, which integrates concepts from both fuzzy control and neural networks, combines the strengths of neural networks and fuzzy control systems. This approach enables the integration of the learning capabilities and computational power of neural networks into fuzzy control systems, while also incorporating the high-level reasoning capabilities of fuzzy control systems into neural networks. Essentially, neural networks can enhance their transparency to resemble fuzzy control systems more closely, whereas fuzzy control systems can adapt autonomously to resemble neural networks. Various methods have been proposed for partitioning the input space and addressing the structure identification problem. Essentially, ANFIS represents a graphical network depiction of a Sugeno-type fuzzy system, enriched with neural learning capabilities. The network comprises nodes with specific functions or roles organized into layers with designated functions. To exemplify the representational capabilities of ANFIS, the neural fuzzy control system under discussion is founded on Tagaki-Sugeno-Kang (TSK) fuzzy rules. In this framework, the consequent parts are formulated as linear combinations of their preconditions. The TSK fuzzy rules adhere to the following structure:

$$R^{j}: \text{IF } x_1 \textit{ is } A_1^j \text{ AND } x_2 \textit{ is } A_2^j \text{ AND}\ldots\text{AND } x_n \textit{ is } A_n^j \quad \text{THEN } y = f_j = a_0^j + a_1^j x_1 + a_2^j x_2 + \ldots + a_n^j x_n \tag{3}$$

where x_i (i = 1, 2, …, n) A_i^j are input variables (evaporation effecting factors), y is the output variable (daily evaporation measurements), are linguistic terms of the precondition part with membership functions $\mu_{A_i^j}(x_i)$ and a_1^j ЄR are coefficients of linear equations f_i (x_1, x_2, …, x_n) (j = 1, 2, ..., m, i = 1, 2, …, n). To streamline the discussion, let's narrow our focus to a particular neuro-fuzzy controller (NFC) known as an adaptive neural-based fuzzy inference system (ANFIS).

Assume that the fuzzy control system under consideration has two inputs x_1 and one output y and that the rule base contains two TSK fuzzy rules as follows:

$$R^{1}: \text{IF } x_1 \textit{ is } A_1^1 \text{ AND } x_2 \textit{ is } A_2^1 \text{ , THEN } y = f_1 = a_0^1 + a_1^1 x_1 + a_2^1 x_2 \tag{4}$$

$$R^{2}: \text{IF } x_1 \textit{ is } A_1^2 \text{ AND } x_2 \textit{ is } A_2^2 \text{ , THEN } y = f_2 = a_0^2 + a_1^2 x_1 + a_2^2 x_2 \tag{5}$$

In fuzzy logic approaches, for given input values x_1 and x_2, the inferred output y^* is calculated by:

$$y^* = (\mu_1 f_1 + \mu_2 f_2)/(\mu_1 + \mu_2) \tag{6}$$

Where μ_j are firing strengths of R_j (j = 1, 2), and are given by:

$$\mu_j = \mu_{A_1^j}(x_1) \times \mu_{A_2^j}(x_2) \qquad j = 1, 2 \tag{7}$$

If product inference is employed, the corresponding ANFIS architecture is depicted in figure 14, where the node functions within the same layers adhere to the following descriptions. Figure 1 is sourced from the reference book by Lin & Lee (1995). In this ANN architecture, each layer can be attributed with the following meanings:

Layer 1: Every node within this layer represents an input and merely transmits external signals to the subsequent layer.

Layer 2: Every node in this layer acts as a membership function $\mu_{A_i^j}(x_i)$, and its output specifies the degree to which the given x_i satisfies the quantifier A_i^j. Generally, $\mu_{A_i^j}(x_i)$ is selected as bell-shaped with a maximum equal to 1 and minimum equal to 0, such as:

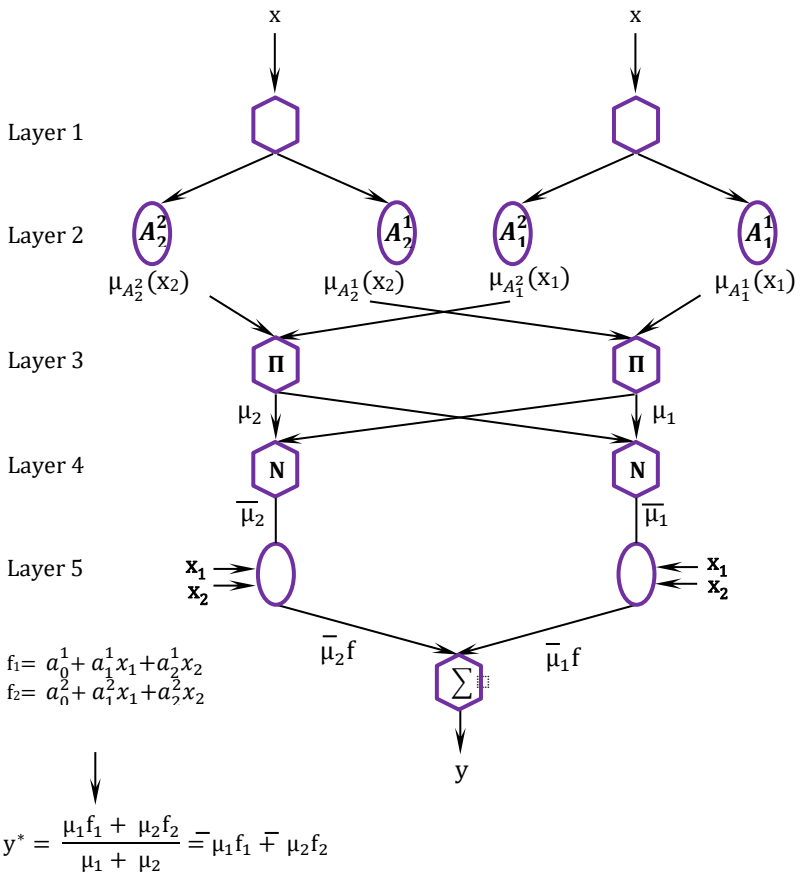

Figure 14. A fuzzy inference system.

$$\mu_{A_i^j}(x_i) = 1 \Big/ \left\{ 1 + \left[\left((x_i - m_i^j)/\sigma_i^j \right) \right]^2 \right\}^{b_i^j} \tag{8}$$

or

$$\mu_{A_i^j}(x_i) = \exp\left\{-\left[\left(\left(x_i - m_i^j\right)/\sigma_i^j\right)\right)^2\right]^{b_i^j}\right\} \quad (9)$$

where $\{ m_i^j, \sigma_i^j, b_i^j \}$ is the parameter set to be tuned. In fact, continuous and piecewise differentiable functions, such as the commonly employed trapezoidal or triangular membership functions, are also suitable candidates for node functions within this layer. The parameters within this layer are denoted as precondition parameters.

Layer 3: Every node in this layer is labelled Π and multiplies the incoming signals $\mu_j = \mu_{A_1^j}(x_1) \times \mu_{A_2^j}(x_2)$ and sends the product out. Each node output represents the firing strength of a rule.

Layer 4: Every node in this layer is labelled by N and calculates the normalized firing strength of a rule. That is the jth node calculates the ratio of the firing strength of the jth rule to that of all the rules as:

$$\overline{\mu_j} = \mu_j / \sum \mu \quad (10)$$

Layer 5: Every node j in this layer calculates the weighted consequent value as ;

$$\overline{\mu_j}(a_0^j + a_1^j x_1 + a_2^j x_2) \quad (11)$$

where $\overline{\mu_j}$ is the output of Layer 4 and $\{ a_0^j, a_1^j, a_2^j \}$ is the set to be tuned. Parameters in this layer are referred to as consequent parameters.

Layer 6: The only node in this layer is labelled as ∑, and it sums all incoming signals to obtain the final inferred result for the whole system (Lin & Lee, 1995).

Figure 15 shows resonant frequency estimation and error percentage when S21, S31, φ21 and φ31 as well as the changes in vias position are selected as inputs and ANFIS simulates the output data. The results here are not precise enough and hence less satisfactory.

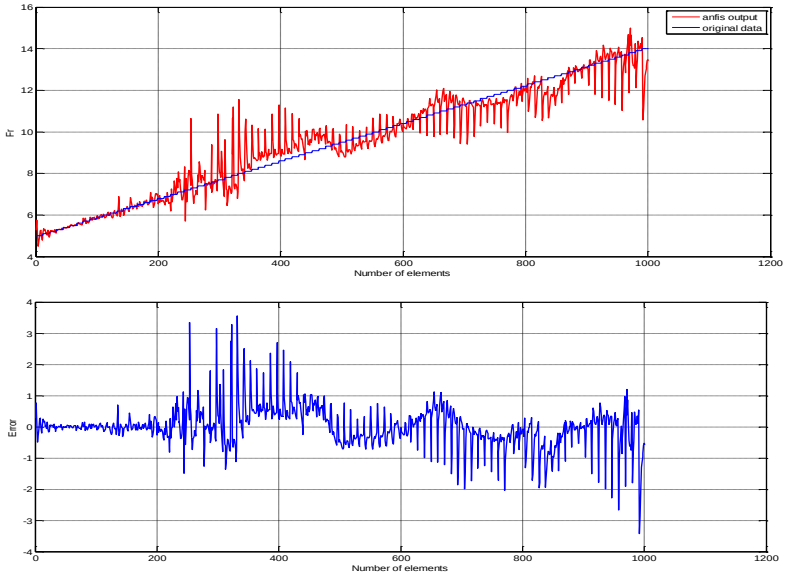

Figure 15. Resonant frequency estimation and its error using ANFIS.

Then S21 and S31 are predicted when resonant frequency and phases of two outputs as well as the position of vias are given as inputs. As can be seen from figure 16 and figure 17, the S-parameters can be recognized with a high accuracy and very low percentage of error.

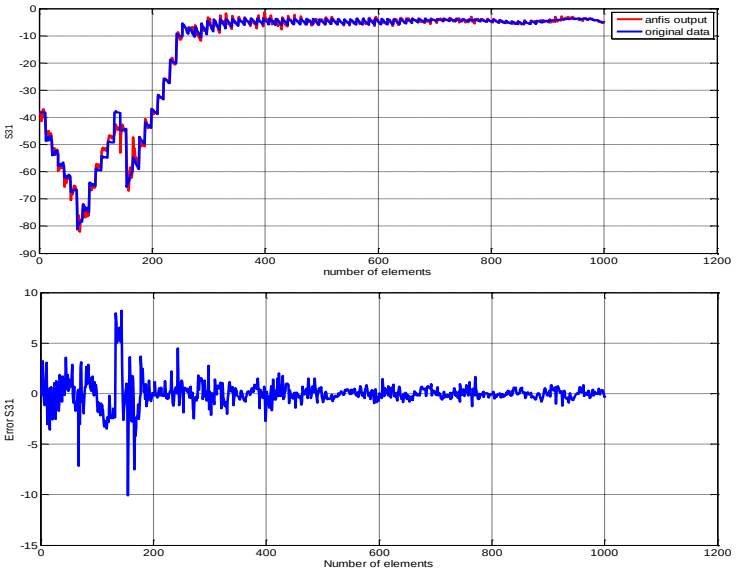

Figure 16. S31 parameters estimation and its error using ANFIS.

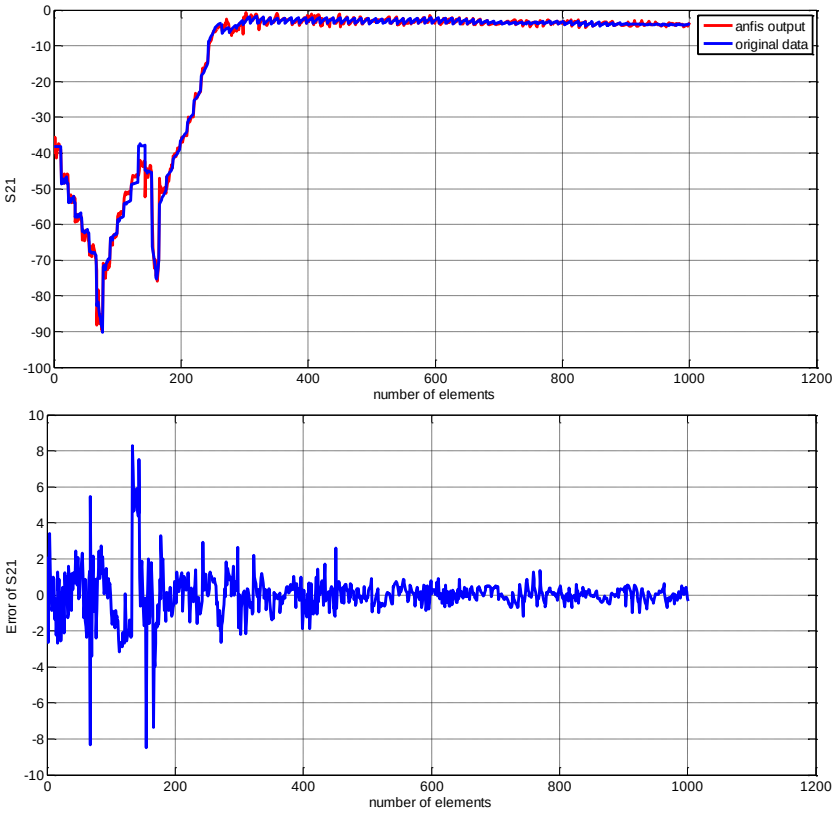

Figure 17. S21 parameters estimation and its error using ANFIS.

Finally, φ21, φ31 are predicted when resonant frequency and powers of the two outputs in addition to the position of vias are given as inputs. As can be seen from the figure 18 and figure 19, ANFIS fails to predict output phases appropriately.

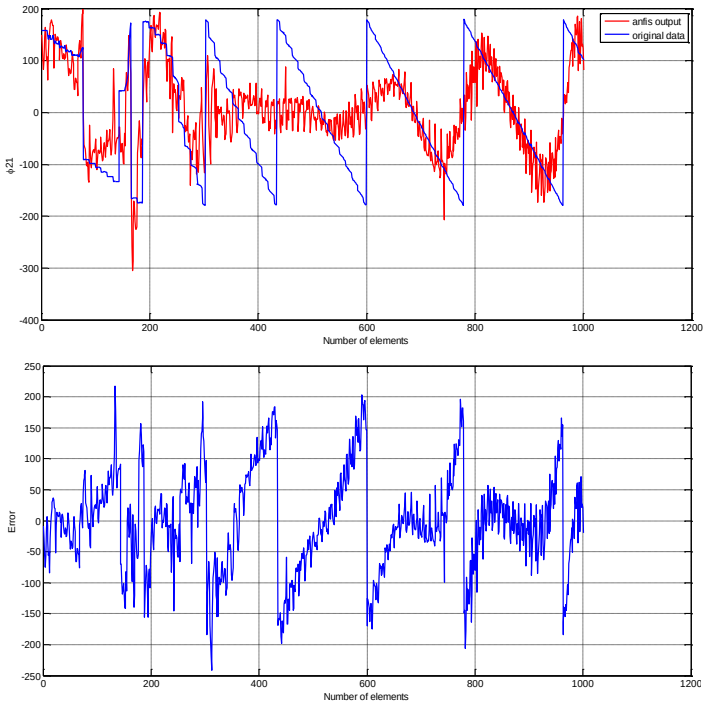

Figure 18. φ21 estimation and its error using ANFIS

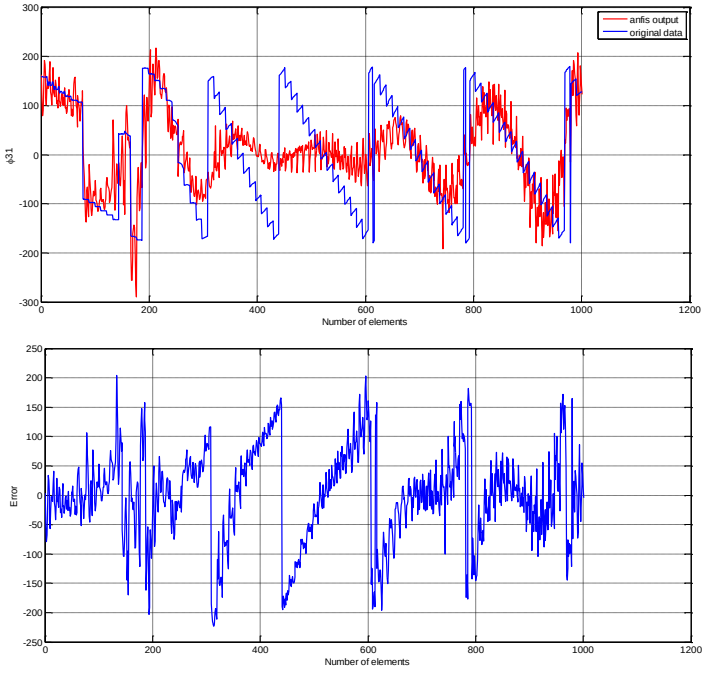

Figure 19. φ31 estimation and its error using ANFIS

3. CONCLUSION

Advanced machine algorithms such as neural networks and fuzzy logic systems have gained widespread recognition and have been extensively utilized across various engineering and scientific domains for numerous years. This paper focuses on calculating the resonant frequency, S-parameters, and output phases of a power divider constructed on a substrate integrated waveguide (SIW) structure with vias whose positions were shifted, resulting in asymmetry. To estimate these parameters, artificial neural networks and adaptive neuro-fuzzy inference systems were employed. The results indicate that ANFIS could predict S-parameters effectively, but the accuracy of output phases and resonant frequency prediction was limited. However, ANFIS results showed good agreement with experimental data, while other machine algorithms exhibited a high percentage of error due to either close proximity of input data or minimal differences in input values in some cases. It's worth noting that this method is not restricted to power dividers alone and can be easily applied to other microwave devices like phase shifters and antennas.

References

[1] E. J. Wilkinson, “An N-way hybrid power divider,” IRE Trans. Microwave Theory Tech., vol. MTT-8, pp. 116-118, Jan. 1960.
[2] L. I. Parad and R. L. Moynihan, “Split-tee power divider.” IEEE Trans. Microwave Theory Tech., vol. MTT-13, pp. 91-95, Jan. 1965.
[3] S. B. Cohn, “A class of broadband three-port TEM-mode hyhrjds,” IEEE Trans. Microwave Theory Tech., vol. MTT-16, pp. 110-116, Eeb. 1968.
[4] R. B. Ekinge, “A new method of synthesizing matched broad-hand TEM mode three ports,” IEEE Trans. Microwave Theory Tech., vol. MTT-19, pp. 81-88, Jan. 1971.
[5] A. M. Saleh, “Planar electrically symmetric N-way hybrid power dividers/combiners,” IEEE Trans. Microwave Theory Tech., vol. MTT-28, pp. 555-563, June 1980.
[6] D. Kother, B. Hopf, T. Sporkmann, and I. Wolff, “MMIC Wilkinson couplers for frequencies up to 110 GHz,” in IEEE MW-S Int. Microwave Symp.. Dig., pp. 663-666, 1995.
[7] Y. Wu, Y. Liu, Q. Xue, S. Li, and C. Yu, “Analytical design method of multiway dual-band planar power dividers with arbitrary power division,” IEEE Trans. Microw. Theory Techn., vol. 58, no. 12, pp. 3832–3841, Dec. 2010.
[8] Y. Wu, Y. Liu, and Q. Xue, “An analytical approach for a novel coupled line dual-band Wilkinson power divider,” IEEE Trans. Microw. Theory Techn., vol. 59, no. 2, pp. 286–294, Feb. 2011.
[9] F. Xu, G. Guo, E. Li, and J. Wu, “An ultra-broadband 3-dB power divider,” in Proc. 5th Global Symp. Millim. Waves (GSMM), May 2012, pp. 347–350.
[10] X. Wang, K.-L. Wu, and W.-Y. Yin, “A compact Gysel power divider with unequal power-dividing ratio using one resistor,” IEEE Trans. Microw. Theory Techn., vol. 62, no. 7, pp. 1480–1486, Jul. 2014.
[11] Abitrary power ratios and filtering responses using coupling structure,” IEEE Trans. Microw. Theory Techn., vol. 62, no. 3, pp. 431–440, Mar. 2014.
[12] L. Wu, Z. Sun, H. Yilmaz, and M. Berroth, “A dual-frequency Wilkinson power divider,” IEEE Trans. Microw. Theory Tech., vol. 54, no. 1, pp. 278–284, Jan. 2006.
[13] K.-K. M. Cheng and C. Law, “A novel approach to the design and implementation of dual-band power divider,” IEEE Trans. Microw. Theory Tech., vol. 56, no. 2, pp. 487–492, Feb. 2008.
[14] M.-J. Park and B. Lee, “A dual-band Wilkinson power divider,” IEEE Microw. Wireless Compon.Lett., vol. 18, no. 2, pp. 85–87, Feb. 2008.
[15] T. Yang, J.-X. Chen, and X. Y. Z. Xue, “A dual-band out-of-Phase power divider,” IEEE Microw. Wireless Compon.Lett., vol. 18, no. 3, pp. 188–190, Mar. 2008.
[16] Y. Wu, Y. Liu, and X. Liu, “Dual-frequency power divider with isolation stubs,” Electron. Lett., vol. 44, no. 24, pp. 1407–1408, Nov. 2008.
[17] Y. Wu, Y. Liu, Y. Zhang, J. Gao, and H. Zhou, “A dual band unequal Wilkinson power divider without reactive components,” IEEE Trans.
[18] Y.Wu,Y. Liu, and S. Li, “An unequal dual-frequency Wilkinson power divider with optional isolation structure,” Progr. Electromagn. Res., vol. 91, pp. 393–411, 2009.
[19] Xiaochuan Shen ; Yongle Wu ; Siyue Zhou ; Yuanan Liu,” A Novel Coupled-Line Tunable Wilkinson Power Divider With Perfect Port Match and Isolation in Wide Frequency Tuning Range,” IEEE Transactions on Components, Packaging and Manufacturing Technology (Volume: 6, Issue: 6, June 2016)
[20] Xiao-Lan Zhao; Li Gao, ; Xiu Yin Zhang ; Jin-Xu Xu,” Novel Filtering Power Divider With Wide Stopband Using Discriminating Coupling” IEEE MICROWAVE AND WIRELESS COMPONENTS LETTERS, VOL. 26, NO. 8, AUGUST 2016
[21] Eslamloo, Masoud Khoubroo, and Pejman Mohammadi. "Compact size, equal-length and unequal-width substrate integrated waveguide phase shifter." 2016 18th International Conference on Advanced Communication Technology (ICACT). IEEE, 2016
[22] Sagiroglu. S.: Guney, K.: Calculation of resonant frequency for an equilateral triangular microstrip antenna with the use of artificial neural networks. Microwave and Optical Technology LetI. 14(1997). 89-93.

[23] Sagiroglu. S.; Guney. K.; Erler, M.: Resonant frequency calculation for circular microstrip antennas using artificial neural networks. mt. J. of RF and Microwave Computer-Aided Engineering 8 (1998), 270-277.
[24] Guney. K.; Sagiroglu. S.; Erler. M.: Design of rectangular microstrip antennas with the use of artificial neural networks, Neural Network World 4 (2002). 361-370.
[25] Guney, K.; Sagiroglu, S.; Erler. M.: Generalized neural method to determine resonant frequencies of various microstrip antennas. mt. J. 01 RE and Microwave Computer-Aided Engineering 12 (2002). 131139.
[26] Yildiz, C.; Gultekin. S. S.; Guney. K.; Sagiroglu, S.: Neural models für the resonant frequency of electrically thin and thick circular microstrip antennas and the characteristic parameters of asymmetric coplanar waveguides hacked with a conductor. AEU-lnternational J. of Electronics and Communications 56(2002), 396-406.
[27] Guney. K.: Sarikaya, N.: Artificial neural networks for calculating the input resistance of circular microstrip antennas, Microwave and Optical Technology Lett, 37(2003), 107-111.
[28] Gultekin. S. S.; Guney. K.: Sagiroglu. S.: Neural networks for the calculation of bandwidth of rectangular n microstrip antennas. Applied computational Electromagnetics Society (ACES) Journal 18 (2003). 46-56.
[29] Guney, K.: Sarikaya, N.: Artificial neural networks for the narrow aperture dimension calculation of optimum gain pyramidal horns. Electrical Engineering 86(2004). 157-163.
[30] Karaboga, D.: Guney, K,: Sagiroglu. S.; Erler, M.: Neural computation of resonant frequency of electrically thin and thick rectangular microstrip antennas. lEE Proc. Mierow. Antennas Propagat. 146 (1999), 155-159.
[31] Sagiroglu, S.: Guney, K.; Erler, M.: Calculation of bandwidth for electrically thin and thick rectangular microstrip antennas with the use of multilayered pcrceptrons. Tnt. J. of RF and Microwave Compulter -Aided Engineering 9(1999), 277-286.
[32] Guney, K.; Erler, M,; Sagiroglu, S.: Artificial neural networks for the resonant resistance calculation of electrically thin and thick rectangular microstrip antennas, Electromagnetics 20(2000), 387-400.
[33] Guney. K.: Sagiroglu, S.: Erler. M.: Comparison of neural networks lhr resonant frequency computation of electrically thin and thick rectangular microstrip antennas. J. of Electromagnetic Waves and Applications 15 (2001), 1121—1145.
[34] K. Guney and N. Sarikaya, ‘‘Adaptive neuro-fuzzy inference system for the input resistance computation of rectangular microstrip antennas with thin and thick substrates’’, J. Electr. Wav. Appl., 18, pp. 23–39, 2004 .
[35] K. Guney and N. Sarikaya, ‘‘Adaptive neuro-fuzzy inference system for computing the resonant frequency of circular microstrip antennas’’, Appl. Comput. Electr. Soc. J., 19, pp. 188–197, 2004 .
[36] K. Guney and N. Sarikaya, ‘‘Computation of resonant frequency for equilateral triangular microstrip antennas using adaptive neuro-fuzzy inference system’’, Int. J. RF and Micr.
Comput.-Aid. Engin., 14, pp. 134–143, 2004 .
[37] K. Guney and N. Sarikaya, ‘‘Input resistance calculation for circular microstrip antennas using adaptive neuro-fuzzy inference system’’, Int. J. Infr. Millim. Wav., 25, pp. 703–716, 2004 .
[38] K. Guney and N. Sarikaya, “Adaptive neuro-fuzzy inference system for computing the resonant frequency of electrically thin and thick rectangular microstrip antennas’, International Journal of Electronics ,Volume 94, 2007 - Issue 9
[39] J.S.R. Jang, ‘‘Anfis: Adaptive-network-based fuzzy inference system’’, IEEE Trans. Syst., Man, Cyber., 23, pp. 665–685, 1993.
[40] M. EROL KESKIN , DILEK TAYLAN & ÖZLEM TERZI (2006) Adaptive neuralbased fuzzy inference system (ANFIS) approach for modelling hydrological time series, Hydrological Sciences Journal, 51:4, 588-598, DOI: 10.1623/hysj.51.4.588

September 2024, Vol:2, Issue:2

International Journal of New Findings in Engineering, Science and Technology

journal homepage: *https://ijonfest.gedik.edu.tr/*

The Characterization of Electrospun PANI/PEO Nanofibers at Different Electrospinning Conditions at Room Temperature

Gözde KONUK EGE [a*], Özge AKAY SEFER [b], Hüseyin YÜCE [b]

[a] *Istanbul Gedik University, Istanbul, 34913, Turkey, gozde.konuk@gedik.edu.tr (*corresponding author)*
[b] *Marmara University, Istanbul, 34722, Turkey, ozge.akay@marmara.edu.tr, huseyin@marmara.edu.tr*

Abstract

Nanofiber structures boast a broad range of applications due to their excellent properties, spanning from sensor technologies and biomedical systems to tissue engineering and drug delivery systems.
Nanofiber structures have wide usage area thanks to their excellent properties from sensor technologies, biomedical systems to tissue engineering, drug delivery systems. Electrospinning method is a versatile method that can produce very fine nanofibers with a simple production mechanism. On the other hand, it is important to optimize the fabrication parameters in order to obtain the appropriate nanofiber structure. In this study, PANI/PEO (Polyaniline/Polyethylene oxide) electrospun nanofibers are fabricated under ambient conditions and the effects of solution viscosity and collector rotation speed on fiber structure are discussed. Electrospun PANI/PEO nanofibers structures are investigated by scanning electron microscope (SEM). According to the SEM results, it is seen that the high viscosity nanofibers have straight and rigid structures. However, the low viscosity nanofiber structures break down at each collector speed, but the fiber orientations increase as the collector rotation speed increases. It is estimated that this study will be guide for future work on PANI.

Keywords: *PANI, Nanofiber, Electrospining, Viscosity*

1. INTRODUCTION

Nowadays, technological developments are quite related to the properties of new generation materials. Especially one-dimensional (1-D) nano-materials (nanotubes, nanowires, nanofibers, etc.), offers innovative approaches in terms of miniaturization, lightweight, flexibility and unique electrical, mechanical, optical and magnetic properties [1–5]. Nanofibers are utilized across a vast array of applications due to their exceptional qualities, straightforward manufacturing processes, and the diversity of materials available [6]. High surface-area-to-volume ratio and porosity [3, 4, 7] is unique specifications of nanofibers that ensure high performance in gas sensing process [8]–[12] and it allow multidisciplinary usage area such as membrane utilization [13–15], biomedical applications-tissue engineering [3, 16, 17], textile [5] and defense industry [18, 19].

In addition to the electrospinning method, which is one of the well-known techniques in nanofiber production, mechanical drawing, self-assembly, hydrothermal processing, melt blowing, extraction, phase separation, vapor phase polymerization, mold synthesis and solvent casting methods have also been used [20]. Polymeric materials,

https://doi.org/10.61150/ijonfest.2024020202

metals, small molecules, composites, colloids are used in the production of nanofibers by electrospinning [20, 21]. Electrospinning has a simple set-up structure due to its simple working principle which is based on electrohydrodynamic process and high electrical voltage [21]. Electrospinning set-up consists of three parts: the supply unit, where the power supply is located, the spinneret and the collector unit. Electrospinning suspension parameters such as viscosity, conductivity, molecular weight and the solvents used to prepare the solution are important for the success of nanofiber production. Besides, feed speed, application voltage, distance between needle-collector and needle diameter are factors that affect nano-fiber diameter and quality. Along with these specifications, environmental temperature and humidity are another important factors that should not be ignored in fiber production [21].

Polyaniline (PANI) is one of the most well-known conductive polymers due to its easily reversible conductor-insulator properties with dopants, easy synthesis/processability and fine optical and magnetic properties [4, 6]. 1-D applications of PANI have quite remarkable features compared to conventional PANI and its thin-film applications. As well as the only-PANI nanofiber structure can be produced with electrospinning, the composite structures of PANI with metal oxides or natural fibers are also have quite application area especially in sensor and membrane processes [8, 9, 22–25].

In this study, PANI/PEO composite nanofibers were produced by electrospinning method. PEO were used as a carrier polymer in electrospinning suspension. Electrospun nanofibers are fabricated under ambient conditions and the effects of solution viscosity and collector rotation speed on fiber structure are discussed.

2. EXPERİMENTAL SETUP

2.1 Materials

PANI emeraldine-base (Mw = 50,000), PEO (Mv = 900,000), camphor sulfonic acid (CSA) and sodium dodecyl sulfate (SDS) were purchased from Sigma-Aldrich. Chloroform and dimethylformamide (DMF) which are used to prepare PANI/PEO solution and other chemicals were purchased from Merck and other commercial sources as guaranteed-grade reagents and used without further purification.

2.2 Preparation of PANI/PEO Suspension

PANI solution were prepared two different concentrations at 2% and 3% v/w ratios. CSA was added at 1:1,5 (PANI:CSA) to protonate the PANI and they were stirred in Chloroform:DMF 1:1 suspension for 24h at room temperature. Then, PEO were added 1:1 (PANI:PEO) in the PANI suspension and the mixed PANI/PEO suspension stirred at 1000 rpm for 24h at room temperature. Viscosity and conductivity values of each polymer solution were measured by Brookfield viscometer and electrical conductivity device (Table1).

Table 1. Viscosity and conductivity values of polymer suspensions

Polymer Suspension	Viscosity (cp)	Conductivity (µS/cm)
PANI-1	220	653 - 21,5°C
PANI-2	117,5	623 - 21,5°C

2.3 Electrospining parameters of polymer suspensions

Electrostatic force is used to produce nanofibers. Due to the electrostatic force, the surface tension of the electrically charged polymer solution is overcome and the polymer jet is formed. The polymer solution, which is

sent to the nozzle in a controlled manner with a pump, tends to elongate owing to the electrical force and is collected on the collector by forming a cone form called a taylor cone [26].

Table 2. Electrospining parameters of polymer suspensions

Polymer Suspension	Viscosity (cp)	Collector Speed (rpm)	Voltage(kV)
A-PANI-1	220	100	25
B-PANI-1	220	300	25
C-PANI-2	117,5	100	25
D-PANI-2	117,5	300	25
E-PANI-2	117,5	500	25

In this electrospining process, NE300 Nano Spinner device were used. Electrospining set-up is shown in Figure 1.

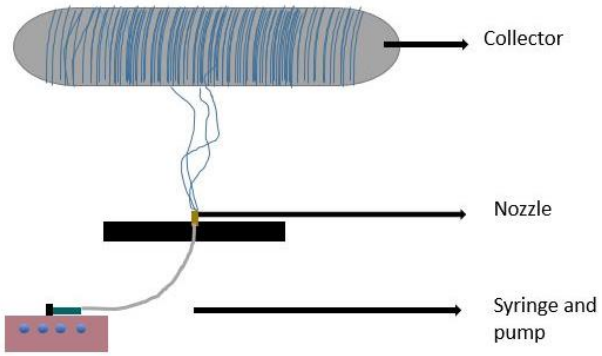

Figure 1. Electrospining Set-Up

PANI/PEO suspensions were added in 10mL syringe. The feed rate was 1.3 mL/h and the applied voltage was 25kV to generate potential difference between the nozzle and the collector. The distance between the nozzle and the collector was 20cm. The electrospining process were performed with 18-gauge nozzle. Each electrospinning process were performed 30 minutes at 23°C-38%RH.
PANI/PEO suspensions were added in 10mL syringe. The feed rate was 1.3 mL/h and the applied voltage was 25kV to generate potential difference between the nozzle and the collector. The distance between the nozzle and the collector was 20cm. The electrospining proses were performed with 18-gauge nozzle. Each electrospinning process were performed 30 minutes at 23°C-38%RH. Electrospining parameters of polymer suspensions are shown in Table 2. PANI/PEO polymer solutions prepared at a ratio of 1.5% v/w and 1.35% v/w with viscosity of 220 cp and 117.5 cp were electrospinned at collector rotational speeds of 100, 300, 500 rpm. (Table 2). In the optimization studies, the effects of electrospinning parameters, polymer concentration, solution viscosity on the nanofiber structure were investigated. The obtained nano-fiber structures were examined with the SEM analysis device, and the appropriate production conditions and solution concentration values were determined.

3. RESULTS AND DISCUSSION

The Electro-spinning parameters affecting the properties of nano-fibers have been the focus of attention of researchers in electrospining processes. In our work, we focused effects of the polymer suspension viscosity and

collector speed on the nano-fiber orientation. PANI is one of the most studied polymers among conductive polymers [25]. Although there are studies on electrospinning of PANI in the literature, the effect of collector speed has not been discussed yet. In this respect, our study is important for the literature. Structural and morphological analyzes of nano-fibers were analyzed by SEM and FT-IR methods.

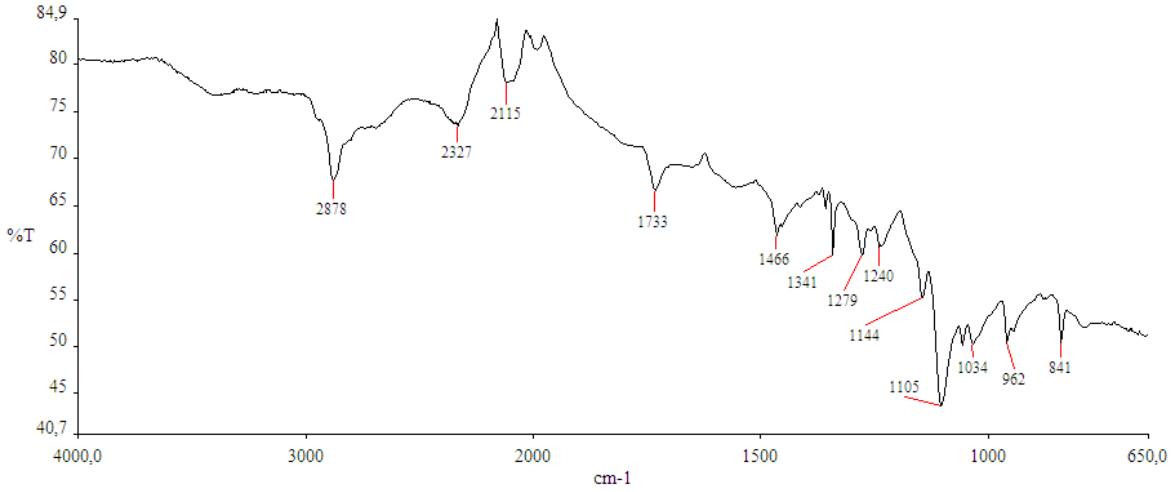

Figure 2. FT-IR Spectra of PANI/PEO

The Perkin-Elmer FT-IR Spectrometer were used to determined functional groups of the PANI /PEO nanofibers. Structures of electrospun PANI/PEO nano-fibers were investigated by Zeiss-Evo Ma10 Scanning Electron Microscope. Through the electrospining process varying conditions affects nano-fiber properties. In this present work, we want to investigate the effects of polymer solution viscosity and collector speed.

Figure 2 shows FT-IR Spectra of PANI/PEO. It is seen a broad peak at the 3,330 cm^{-1} region because of the O—H groups. C—H aliphatic bond were shown at 2878 cm^{-1} peaks region. Peaks at 1,466cm^{-1} region because of C═N, 341 cm^{-1} and 1,279 cm^{-1} were corresponding C—N, peaks at 1034 cm^{-1} and 962 cm^{-1} regions relevent to C—H aromatics and also 841 cm^{-1} peaks were demonstrated of SO_3 group [1].

Figure 3 demonstrates the SEM images of PANI/PEO nanofibers with the difference of viscosity and collector speed of PANI/PEO changes the morphology of the nanofibers. Two different PANI solutions with 220 cp and 117,5 cp viscosity were produced on a collector at different speeds at constant feed rate and voltage. The structure of the electrospun PANI nano-fibers were investigated. The syringe feed rate was 1.3 mL/h and the voltage was 25 kV. The distance between the nozzle and the collector is 20 cm. PANI nanofibers (sample A and B) with a solution viscosity of 220 cp were produced in a collector with a rotational speed of 100 rpm and 300 rpm. The structure of PANI nanofibers is shown in Figure 3 (A-B). PANI nanofibers with a solution viscosity of 117,5 cp were produced in a collector with a rotational speed of 100, 300 and 500 rpm at the same feed rate and power.

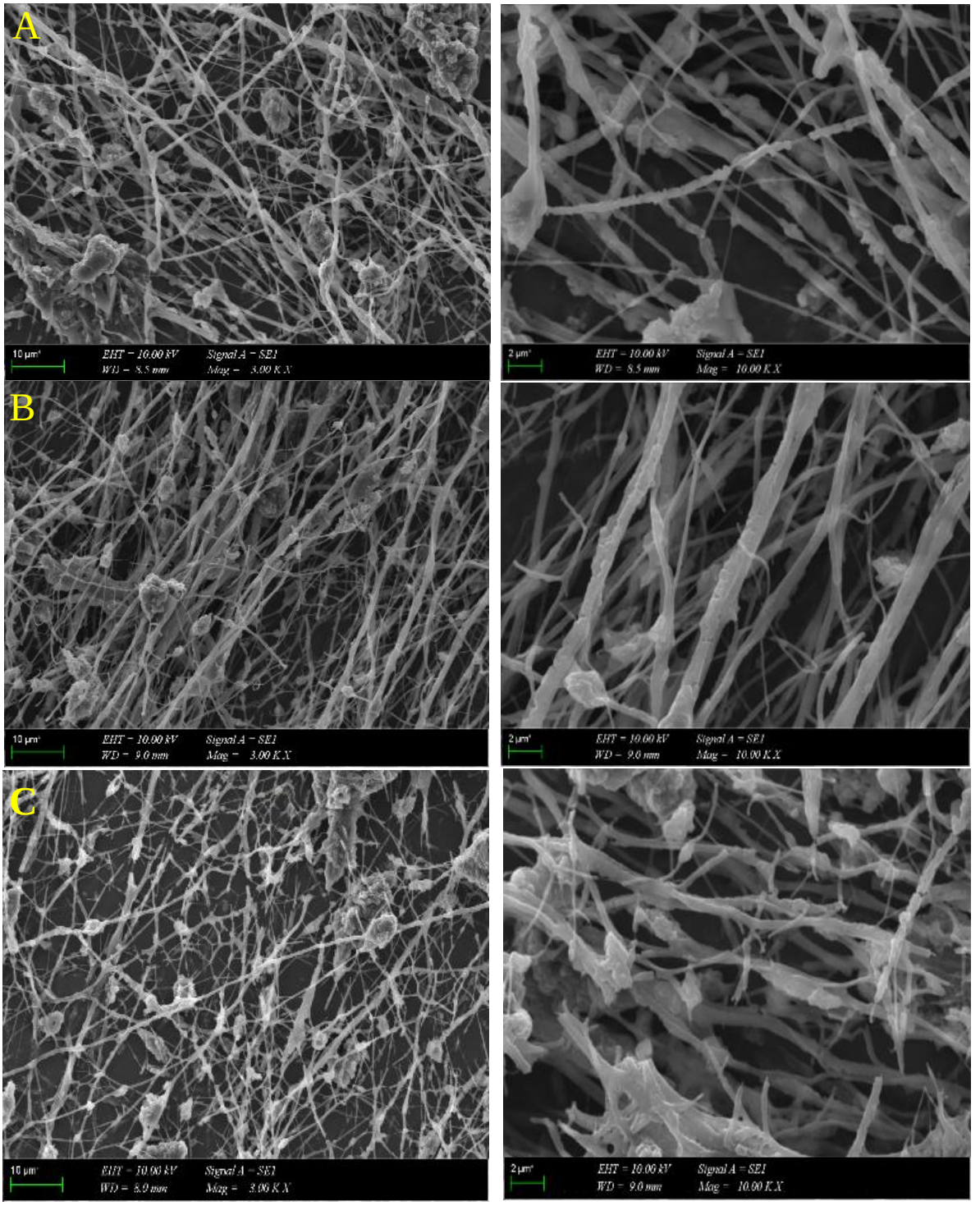

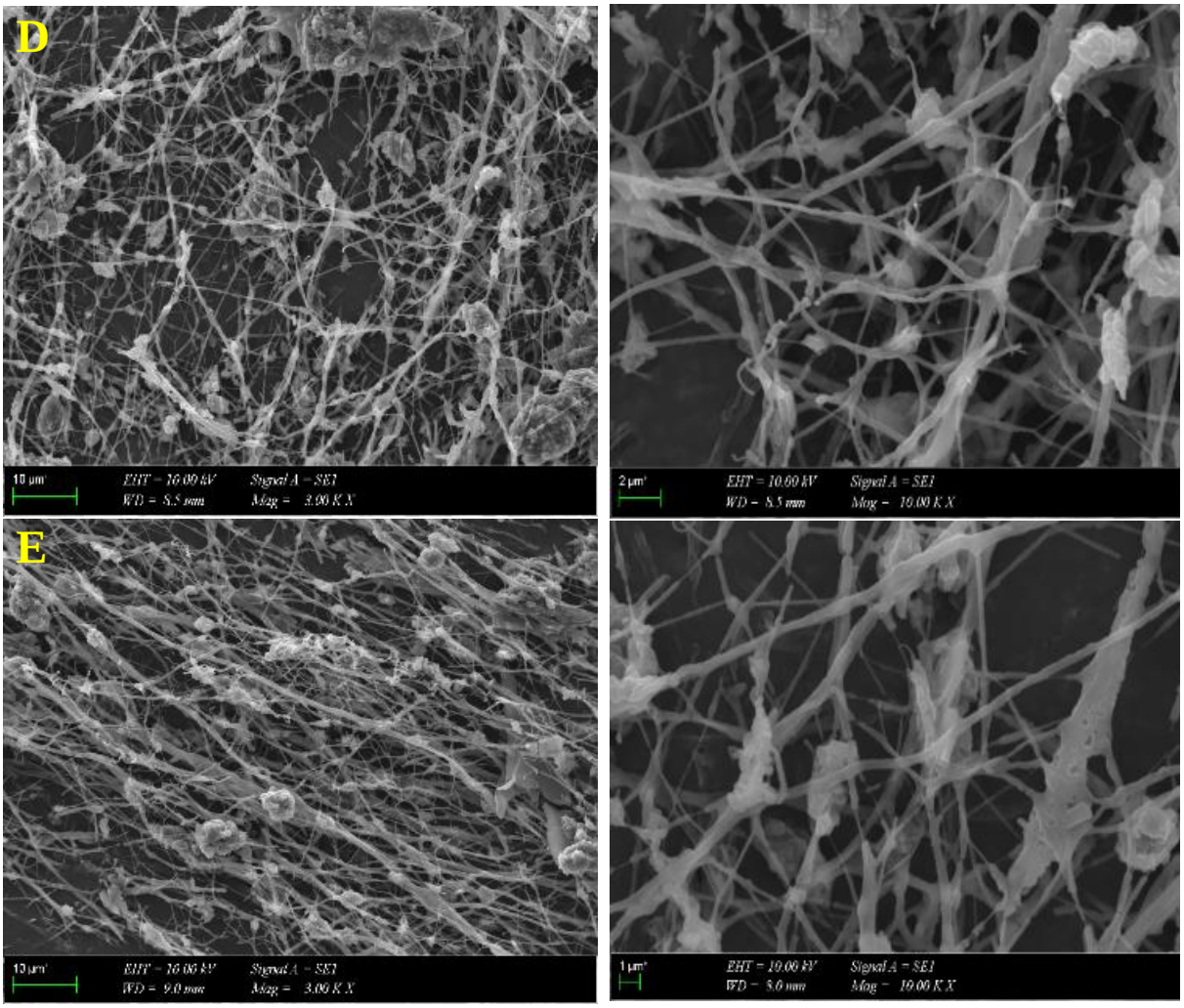

Figure 3. SEM images of PANI.CSA/PEO

Structures of these electrospun nanofibers are shown in Figure 3 (C-E). According the SEM results, as the polymer viscosity decreases, the polymer jet breaks up before it reaches the collector. Accordingly, when the fiber structures in Figure 3 are observed, it is seen that the nano-fiber structures with low viscosity are fragmented at each collector speed, however the fiber orientations increase as the collector roller speed increases [1]. At the same collector roller speed condition, the more continuous nanofibers are attained from the polymer has high viscosity as compared in Figure 3 (B, D). However, the width of the nanofibers cannot be compared in terms of the viscosity of the polymer and the collector speed of the device.

4. CONCLUSION

In this study, PANI/PEO nano-fibers were successfully fabricated by means of the solution electrospinning technique under ambient conditions. Then, the effects of solution concentration and the collector speed on the morphology of the electrospun PANI/PEO nano-fibers were thoroughly investigated. The SEM images indicated

that the increasing of the collector speed, nano-fiber orientations were increased. On the other hand, the lower solution concentration, the diameter distributions were break down and destroyed.

Acknowledgements

This work was supported by Scientific Research Projects Coordination Unit of Istanbul Gedik University, Project number “GDK201905-14”.

References

[1] Konuk Ege, G., Yüce, H., Akay, Ö., Öner, H. and Genç, G. (2023), "A fabrication and characterization of luffa/PANI/PEO biocomposite nanofibers by means of electrospinning", Pigment & Resin Technology, Vol. 52 No. 1, pp. 151-159. https://doi.org/10.1108/PRT-09-2021-0105

[2] S. R. Djafari Petroudy, S. Arjmand Kahagh, and E. Vatankhah, “Environmentally friendly superabsorbent fibers based on electrospun cellulose nanofibers extracted from wheat straw,” *Carbohydr. Polym.*, vol. 251, no. August 2020, p. 117087, 2021.

[3] B. Sun *et al.*, “Advances in three-dimensional nanofibrous macrostructures via electrospinning,” *Prog. Polym. Sci.*, vol. 39, no. 5, pp. 862–890, 2014.

[4] S. Izwan *et al.*, “A Review of Electrospun Conductive Polyaniline Based Nanofiber Composites and Blends: Processing Features, Applications, and Future Directions,” *Adv. Mater. Sci. Eng.*, vol. 2015, pp. 1–19, 2015.

[5] A. Chinnappan, C. Baskar, S. Baskar, G. Ratheesh, and S. Ramakrishna, “An overview of electrospun nanofibers and their application in energy storage, sensors and wearable/flexible electronics,” *J. Mater. Chem. C*, vol. 5, no. 48, pp. 12657–12673, 2017.

[6] C. Bavatharani *et al.*, “Electrospinning technique for production of polyaniline nanocomposites/nanofibres for multi-functional applications: A review,” *Synth. Met.*, vol. 271, no. October 2020, p. 116609, 2021.

[7] G. Acik, “A comprehensive study on electrospinning of poly (Vinyl alcohol): Effects of the tcd, applied voltage, flow rate, and solution concentration,” *J. Turkish Chem. Soc. Sect. A Chem.*, vol. 7, no. 2, pp. 609–616, 2020.

[8] Y. Li, J. Gong, G. He, and Y. Deng, “Fabrication of polyaniline/titanium dioxide composite nanofibers for gas sensing application,” *Mater. Chem. Phys.*, vol. 129, no. 1–2, pp. 477–482, 2011.

[9] Q. Wang *et al.*, “Ammonia sensing behaviors of TiO2-PANI/PA6 composite nanofibers,” *Sensors (Switzerland)*, vol. 12, no. 12, pp. 17046–17057, 2012.

[10] M. Imran, N. Motta, and M. Shafiei, “Electrospun one-dimensional nanostructures : a new horizon for gas sensing materials,” no. 2, 2018.

[11] Q. Nie *et al.*, “Facile fabrication of flexible SiO2/PANI nanofibers for ammonia gas sensing at room temperature,” *Colloids Surfaces A Physicochem. Eng. Asp.*, vol. 537, no. October 2017, pp. 532–539, 2018.

[12] S. Pandey, “Highly sensitive and selective chemiresistor gas/vapor sensors based on polyaniline nanocomposite: A comprehensive review,” *J. Sci. Adv. Mater. Devices*, vol. 1, no. 4, pp. 431–453, 2016.

[13] S. Neubert, D. Pliszka, V. Thavasi, and E. Wintermantel, “Conductive electrospun PANi-PEO / TiO 2 fibrous membrane for photo catalysis,” *Mater. Sci. Eng. B*, vol. 176, no. 8, pp. 640–646, 2011.

[14] W. Wang, Y. Zheng, X. Jin, Y. Sun, B. Lu, and H. Wang, “Nano Energy Unexpectedly high piezoelectricity of electrospun polyacrylonitrile nano fi ber membranes,” *Nano Energy*, vol. 56, no. November 2018, pp. 588–594, 2019.

[15] F. I. M. Ali, F. Awwad, Y. E. Greish, A. F. S. Abu-Hani, and S. T. Mahmoud, “Fabrication of low temperature and fast response H2S gas sensor based on organic-metal oxide hybrid nanocomposite membrane,” *Org. Electron.*, vol. 76, no. October 2019, p. 105486, 2020.

[16] F. K. Mwiiri and R. Daniels, “Chapter 3 - Electrospun nanofibers for biomedical applications,” in *Delivery of Drugs*, R. Shegokar, Ed. Elsevier, 2020, pp. 53–74.

[17] V. Leung and F. Ko, “Biomedical applications of nanofibers,” *Polym. Adv. Technol.*, vol. 22, no. 3, pp. 350–365, 2011.

[18] O. Akampumuza, H. Gao, H. Zhang, D. Wu, and X. H. Qin, “Raising Nanofiber Output: The Progress, Mechanisms, Challenges, and Reasons for the Pursuit,” *Macromol. Mater. Eng.*, vol. 303, no. 1, pp. 1–17, 2018.

[19] M. M. Harussani, S. M. Sapuan, G. Nadeem, T. Rafin, and W. Kirubaanand, “Recent applications of carbon-based composites in defence industry: A review,” *Def. Technol.*, 2022.

[20] G. Acik and C. Altinkok, “Polypropylene microfibers via solution electrospinning under ambient conditions,” *J. Appl. Polym. Sci.*, vol. 136, no. 45, pp. 1–6, 2019.

[21] J. Xue, T. Wu, Y. Dai, and Y. Xia, “Electrospinning and electrospun nanofibers: Methods, materials, and applications,” *Chem. Rev.*, vol. 119, no. 8, pp. 5298–5415, 2019.

[22] Z. Pang *et al.*, “A room temperature ammonia gas sensor based on cellulose/TiO2/PANI composite nanofibers,” *Colloids Surfaces A Physicochem. Eng. Asp.*, vol. 494, pp. 248–255, 2016.

[23] Z. Fan, Z. Wang, N. Sun, J. Wang, and S. Wang, “Performance improvement of polysulfone ultrafiltration membrane by blending with polyaniline nanofibers,” *J. Memb. Sci.*, vol. 320, no. 1–2, pp. 363–371, 2008.

[24] Y. Li, M. Jiao, H. Zhao, and M. Yang, “High performance gas sensors based on in-situ fabricated ZnO/polyaniline nanocomposite: The effect of morphology on the sensing properties,” *Sensors Actuators, B Chem.*, vol. 264, no. 2, pp. 285–295, 2018.

[25] V. Kumar, A. Mirzaei, M. Bonyani, K. H. Kim, H. W. Kim, and S. S. Kim, “Advances in electrospun nanofiber fabrication for polyaniline (PANI)-based chemoresistive sensors for gaseous ammonia,” *TrAC - Trends Anal. Chem.*, vol. 129, p. 115938, 2020.

[26] G. Acik, C. E. Cansoy, and M. Kamaci, “Effect of flow rate on wetting and optical properties of electrospun poly(vinyl acetate) micro-fibers,” *Colloid Polym. Sci.*, vol. 297, no. 1, pp. 77–83, 2019.

September 2024, Vol:2, Issue:2

International Journal of New Findings in Engineering, Science and Technology

journal homepage: *https://ijonfest.gedik.edu.tr/*

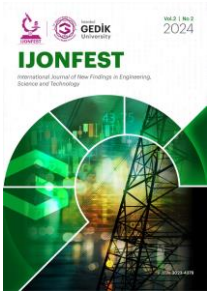

Investigation of an Exact Solution of a Mixed Boundary Value Problem Using the Residue Method

Bahaddin Sinsoysal[a*], Mahir A. Rasulov[b]

[a]*Department of Computer Engineering, Faculty of Engineering, Istanbul Gedik University, Kartal, Turkey*
*e-mail:bahaddin.sinsoysal@gedik.edu.tr (*Corresponding Author)*
[b]*Ministry of Science and Education of Azerbaijan, Institute of Oil and Gas, Baku, Azerbaijan e-mail:mresulov@gmail.com*

Abstract

In this study, a finite differences method is proposed for solving a mixed problem, which represents phenomena in hydrodynamics. To evaluate the approximate solution of the problem, its analytical solution is also constructed by the residue method developed by M.L. Rasulov, which is applied to find the solution of the partial differential equations containing time-dependent derivatives at boundary conditions. The formula for expansion of an arbitrary function in a series of residues of the solution of the corresponding spectral problem is used to show that the solution of the mixed boundary-value problem can be represented by the given residue formula. The use of the residual method gives an exact solution for the mixed boundary value problem, represented as a rapidly decreasing series. The derived formula makes it possible to formally establish both the existence and the uniqueness of the solution. Moreover, the derived formula provides a framework for evaluation, allowing a comparative analysis between the exact solution and the numerical approach.

Keywords: Residue method, Residue representation of the solution, Expansion formula, Boundary condition with higher order derivative.

1. INTRODUCTION

The Fourier method, also called the method of separation of variables, is one of the basic classical methods for integrating some linear partial differential equations under given boundary and initial conditions. The method is a powerful tool for finding an analytical solution to mixed problems of mathematical physics equations (Fourier, 1822). Other classical methods are the Fourier-Birkhoff method (Birkhoff, 1908a, 1908b), the potential method, the Laplace method, and the residual method, first proposed by Cauchy (1827). The application of the Fourier method to the solution of mixed problems reduces to the problem of the expansion of an arbitrary function from some class of eigenfunctions corresponding to the spectral problem (Fourier, 1822).

For a spectral problem with multiple points with discontinuous coefficients, the concept of regularity was given by M.L. Rasulov; unlike Tamarkin, the formula of multiple expansion was obtained, which is extremely important for the solution of related complex problems for partial differential equations (Rasulov, 1959 and 1963). In fact, he

https://doi.org/10.61150/ijonfest.2024020203

has developed the "method of contour integration" and "residual method," which have been applied with success to the solution of problems with both one-dimensional and multidimensional partial differential equations with discontinuous coefficients. Moreover, the residue method can be applied to equations that cannot be separated into their variables and to equations whose operator is not self-adjoint and may even be used in cases where they contain time-dependent derivatives at boundary conditions. It is proven that the formula for the expansion of an arbitrary vector function in the fundamental functions of a one-parameter boundary problem (Rasulov, 1959). The theory of non-self-adjoint operator equations is extensively investigated by M. Keldysh (Keldysh, 1951).

The residual method was applied, respectively, to obtain the exact solution of the boundary value problem with non-classical conditions for one- and two-dimensional heat equations and a one-dimensional linear wave equation in the form of a rapidly decreasing series (Rasulov and Sinsoysal, 2008; Sinsoysal and Rasulov, 2008; Sinsoysal, 2009). Also, it was used the Cauchy problem of a system of ordinary differential equations with constant coefficients to find the exact solution of the constant voltage problem of an RC circuit (Sinsoysal and Rasulov, 2013). Moreover, the solution of the first type of mixed problem for a two-dimensional linear parabolic equation in a bounded cylinder of Euclidean space is found in explicit form by using the residue method (Sinsoysal and Rasulov, 2020).

2. THE MAIN PROBLEM

Let R^2 be an Euclidean space of points (x,t) and let $Q_T = \{(x,t) \mid 0 \le x \le \ell, 0 \le t < T\} \subset R^2$. In Q_T we consider the following mixed problem

$$\frac{\partial u(x,t)}{\partial t} = \kappa \frac{\partial^2 u(x,t)}{\partial x^2} + f(x,t), \quad 0 \le x \le \ell, t \ge 0, \tag{1}$$

$$u(x,0) = u_0(x), \tag{2}$$

$$A\frac{\partial u(0,t)}{\partial x} + B\frac{\partial u(0,t)}{\partial t} = q(t), \tag{3}$$

$$u(\ell,t) = u_c(t), \quad t > 0 \tag{4}$$

where κ, ℓ, T, A and B are given positive real numbers with physical meaning and, $q(t)$ is a known function for any $t > 0$. t and x are time and spatial coordinates, respectively. The problem (1)-(4), which is called the main problem, is often frequently encountered during the theoretical study of many physical processes, both thermo- and hydrodynamic. The theoretical study of many interesting problems of plane-radial filtration theory is also brought to the solution of problems of type (1)-(4).

It is known that the information necessary for the determination of some hydrodynamic indicators of oil fields can be obtained only when the well is suddenly closed and opened (Charny, 1963). In this case, the time derivative includes in the boundary condition, which causes certain difficulties in the application of classical solution methods.

2.1 Finite Differences Schemes for the Main Problem

An algorithm for finding an approximate solution to the dimensionless problem (1)-(4) by the following finite difference method is proposed

$$\frac{\partial u(\xi,\tau)}{\partial \tau} = \kappa \frac{\partial^2 u(\xi,\tau)}{\partial \xi^2} + f(\xi,\tau), \quad 0 \le \xi \le 1, \tag{5}$$

$$u(\xi,0) = 1, \tag{6}$$

$$\delta_0 \frac{\partial u(0,\tau)}{\partial \tau} + \frac{\partial u(0,\tau)}{\partial \xi} = 0, \tag{7}$$

$$u(1,\tau) = \frac{u_c(\tau)}{u_0} \tag{8}$$

Here κ and δ_0 are given positive parameters having physical sense related of anayzed problem. Now, we will explain the finite difference algorithm to compute a numerical solution to the main problem (5)-(8). For this purpose, a uniform grid covering the region $Q_T^{(\xi,\tau)}$ in which the problem is discretized is created

$$\Omega_{h_\xi,h_\tau} = \{(\xi_j,\tau_n) \mid \xi_j = jh_\xi, \tau_n = nh_\tau, h_\xi > 0, h_\tau > 0, j = 0,1,2,\dots N, n = 0,1,2,\dots\}$$

and the finite difference approximation of the problem (5)-(8) is constructed at an arbitrary (ξ_j,τ_n) node point of the grid as

$$\frac{U_{j,n+1} - U_{j,n}}{h_\tau} = \frac{1}{h_\xi^2}\left(U_{j+1,n+1} - 2U_{j,n+1} + U_{j-1,n+1}\right), \tag{9}$$

where $j = 1,2,\dots,N-1; n = 0,1,2,\dots,$

$$U_{j,0} = 1, (j = 0,2,\dots,N), \tag{10}$$

$$\delta_0 \frac{U_{0,n+1} - U_{0,n}}{h_\tau} + \frac{U_{1,n+1} - U_{0,n+1}}{h_\xi} = 0, \tag{11}$$

$$U_{N,n+1} = \phi(\tau_{n+1}), \ (n = 0,2\dots.). \tag{12}$$

Here, $\phi(\tau_n) = \frac{u_{\tau_n}}{u_0}$, the grid function $U_{j,n}$ represents approximate values of the function $u(x,t)$ at point (i,k). In order to obtain the solution of the main problem by using algorithm (9)-(12) we must define value of $U_{0,n+1}$. From (11) we have: $U_{0,n+1} = U_{0,n} - \frac{\delta_0 h_\tau}{h_\xi}\left(U_{1,n} - 2U_{0,n} + U_{-1,n}\right)$.

It should be note that the order of approximation of schema (9)-(12) has $O\left(h_\tau + h_\xi\right)$ of accuracy. The question of increase the order of accuracy of this schema we will consider later. Now the algorithm for obtaining of the unknown $U_{j,n+1}$ is purposed. On the basis of this proposed algorithm, a computer experiment was carried out and the result is shown in Figure 1.

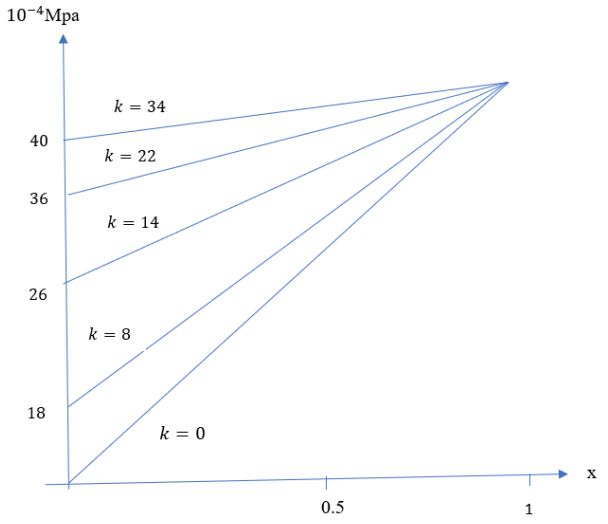

Figure 1. Numerical solution

2.2 Analytical Solution of the Main Problem

Now let us construct the analytical solution of the main problem by residue method. The aim here is to compare the analytical solution with the solution given by the numerical algorithm. In order to perform the residue method, by replacing with $v(\xi,\tau) = u(\xi,\tau) - g(\xi,\tau)$, $g(\xi,\tau) = e^{\frac{\tau}{\delta_0}}\xi + 1 - e^{\frac{\tau}{\delta_0}}$, $f(\xi,\tau) = \frac{1}{\delta_0}(1-\xi)e^{\frac{\tau}{\delta_0}}$, $v_0(\xi) = 1 - \xi$ the problem is reduced to a homogeneous boundary condition problem sas follows

$$\frac{\partial v(\xi,\tau)}{\partial \tau} = \frac{\partial^2 v(\xi,\tau)}{\partial \xi^2} + f(\xi,\tau), \tag{13}$$

$$v(\xi,0) = v_0(\xi), \tag{14}$$

$$\delta_0 \frac{\partial v(0,\tau)}{\partial \tau} + \frac{\partial v(0,\tau)}{\partial \xi} = 0, \tag{15}$$

$$v(1,t) = 0. \tag{16}$$

According of the residue method, we associate the following two problems with complex parameter corresponding to problem (13)-(16) as

2.2.1. *Spectral problem*

$$y'' - \lambda^2 y = h(\xi), \tag{17}$$

$$\lambda^2 y(\xi) + \frac{1}{\delta_0} y'(0) = -h(0), \quad y(1,\lambda) = 0, \tag{18}$$

2.2.2. *Chauchy's problem*

$$\frac{dz}{dt} - \lambda^2 z = f, \tag{19}$$

$$z(\xi, 0) = u_0(\xi), \tag{20}$$

where $h(\xi)$ is an arbitrary continuous function having the derivative of first order on [0,1].

It is clearly that $z(\xi,\tau,\lambda) = u_0(\xi)\, e^{\lambda^2\tau} + \int_0^\tau f(\xi,\theta) e^{\lambda^2(\tau-\theta)} d\theta$ is solution of problem (19), (20). According to the general theory of boundary problem of ordinary differential equations the soltion of (17), (18) is constructed as follows

$$y(\xi,\lambda,h(\xi)) = \int_0^1 G(\xi,\eta,\lambda) h(\xi)\, d\eta + \frac{Y(\xi,\lambda,h(\xi))}{\Delta(\lambda)}, \tag{21}$$

where

$$G(\xi,\eta,\lambda) = \frac{\Delta(\xi,\eta,\lambda)}{\Delta(\lambda)} \tag{22}$$

which is called Green's function of problem (17), (18),

$$\Delta(\lambda) = (\delta_0\lambda^2 + \lambda)e^{-\lambda} - (\delta_0\lambda^2 - \lambda)e^{\lambda},$$

$$\Delta(\xi,\eta,\lambda) = \begin{vmatrix} g(\xi,\eta,\lambda) & e^{\lambda}\xi & e^{-\lambda}\xi \\ \delta_0\lambda^2 g(0,\eta,\lambda) + g'(0,\eta,\lambda) & \delta_0\lambda^2 + \lambda & \delta_0\lambda^2 - \lambda \\ g(1,\eta,\lambda) & e^{\lambda} & e^{-\lambda} \end{vmatrix},$$

$$g(\xi,\eta,\lambda) = \begin{cases} \dfrac{1}{2\lambda}\sinh\lambda(\xi-\eta), & 0 \le \eta \le \xi \le 1, \\ -\dfrac{1}{2\lambda}\sinh\lambda(\xi-\eta), & 0 \le \xi \le \eta \le 1. \end{cases}$$

Because of (17), (18) is *R* regular in sense (Rasulov, 1963), that the following two statements take place:

1. Under fulfillment the condition *R* regularity for the Green's function in domain R_δ^* takes place the estimate $G(x,\xi,\lambda) = O\left(\frac{1}{\lambda^{n-1}}\right)$,

where $R_\delta^* = R_\delta - \cup_\nu K_\delta(\lambda_\nu)$, $K_\delta(\lambda_\nu)$ is a circle with radius of δ and in center of the roots of the equation $\Delta(\lambda) = 0$.

2. For any continuously differentiable on [0,1] function $h(\xi)$ take place the following expansion

$$h(\xi) = -\frac{1}{2\pi\sqrt{-1}}\sum_{\nu}\int_{C_\nu} \lambda\, y(\xi,\lambda,h)\, d\lambda$$

where the sum with respect to ν extend on all the poles of the integrand function.

Under these assumptions and according to the general theory of residue method (Rasulov, 1963), the analytical solution of problem (1)-(4) is obtained in the form of a rapidly decreasing series

$$u(\xi,\tau) = \frac{-1}{2\pi\sqrt{-1}}\sum_{\nu}\int_{C_\nu} \lambda e^{\lambda^2\tau}\int_0^1 G(\xi,\eta,\lambda)\left[u_0(\xi) + \int_0^\tau e^{\lambda^2(\tau-\theta)} f(\eta,\theta)d\theta\right] d\eta d\lambda +$$
$$\frac{-1}{2\pi\sqrt{-1}}\sum_{\nu}\int_{C_\nu} \lambda_\nu \frac{Y(\xi,\lambda,h)}{\Delta(\lambda)}d\lambda \qquad (23)$$

where C_V is a simple closed contour enclosing only one of the poles of λ_ν of integrand function.

As it is seen from (22) computation of this integral be reduced to calculation of the roots of the characteristic determinant $\Delta(\lambda)$. It is clear that the equation (22) is transcendental, therefore necessary to find of this roots numerically, or for roots it possible asymptotic representations. Transforming equation (22) we have $e^{2\lambda} = \frac{\delta_0+\frac{1}{\lambda}}{\delta_0-\frac{1}{\lambda}}$.

It is seen from this the relation of the right side tend to one if $\lambda \to \infty$. Therefore the roots of $\Delta(\lambda) = 0$ by $\lambda \to \infty$ tend to roots of the $\Delta(\lambda) = 1$, that is $\lambda_\nu = 2\pi\nu\sqrt{-1}$, $\nu = 0, \pm1, \pm2, ...$

For these values of λ_ν the function defined by (23) is computed easily. Taking into account the above substitutions for the function $v(\xi,\tau)$ we have the following representation as

$$v(\xi,\tau) = \sum_{\nu=1}^{\infty}\frac{1}{\pi\nu(\delta_0\pi^2\nu^2+1)}\left\{\sin\pi\nu\xi(\cos\pi\nu - 1) - \pi\nu\cos\pi\nu\xi\left[e^{-\pi^2\nu^2\tau} + \frac{e^{\frac{\tau}{\delta_0}} - e^{-\pi^2\nu^2\tau}}{1+\delta_0\pi^2\nu^2}\right]\right\} +$$
$$+1 - e^{\frac{\tau}{\delta_0}\xi} - e^{\frac{\tau}{\delta_0}}.$$

and its graph is shown in Figure 2.

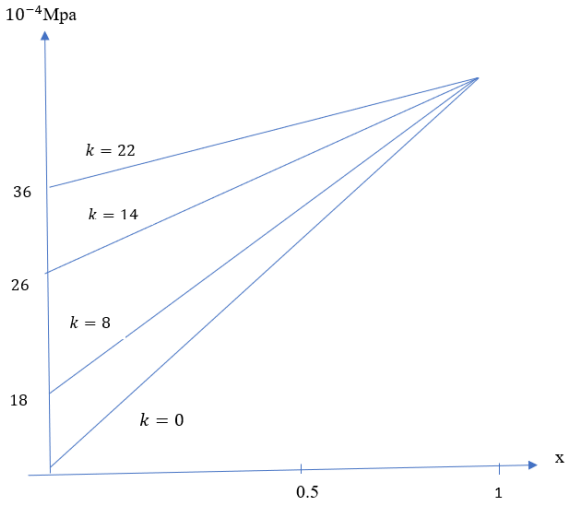

Figure 2. Result obtained by analytical solution

3. CONCLUSION

By finite differences method the numerical solution of the main problem is obtained with order $O(h_\tau + h_\xi)$. It is also possible to write higher order difference schema of the finite difference system with respect to τ. The residual method is used to find the exact solution of the mixed boundary value problem in the form of a rapidly decreasing series. Through the derived formula, the existence and uniqueness of the solution can be proved. Furthermore, this formula allows us to compare the exact solution with the approximate solution calculated by using numerical methods.

Funding

There are no financial interests in this study.

Declaration of Competing Interest

There is no conflict of interest in this study.

References

[1] Birkhoff, G. (1908a). On the asymptotic character of the solutions of certain linear differential equations containing a parameter. Trans. Amer. Math. Soc. 9, 219–231.
[2] Birkhoff, G. (1908b). Boundary value and expansion problems of ordinary linear differential equations. Trans. Amer. Math. Soc. 9, 373–395.
[3] Cauchy, A. (1827). Mémoire sur l'Application du Calcul des Résidus à la Solution des Problèmes de Physique Mathématique. Paris: Chez de Bure frères.
[4] Charny, I. (1963). Underground Fluid Dynamics. Moscow-Leningrad : Gostekhizdat. [in Russian].
[5] Fourier, J. (1822). Théorie Analytique de la Chaleur. Paris: Firmin Didot.
[6] Keldysh, M. (1951). On eigenvalues and eigenfunctions of some classes of nonselfadjoint equations. Dokl. Akad. Nauk SSSR, 77, 11–14.
[7] Liouville, J. (1837). Second mémoire sur le développement des fonctions ou parties de fonctions en séries dont les divers termes sont assujettis à satisfaire à une même équation différentielle du second ordre, contenant un paramètre variable. J. Math. Pures Appl., 2, 16–35.
[8] Poincaré, H. (1894). Sur les équations aux dérivées partielles de la physique mathématique. Rend. Circ. Mat. Palermo, 8, 57–155.
[9] Rasulov, M.L. (1959). The residue method for solution of mixed problems for differential equations and a formula for expansion of an arbitrary vector-function in fundamental functions of a boundary problem with a parameter. Matematicheskii Sbornik, 90, 277–310.

[10] Rasulov, M.L. (1963). The contour integral method and its application to the solution of multi-dimensional mixed problems for differential equations of parabolic type. Matematicheskii Sbornik, 102, 393–410.
[11] Rasulov, M.L. (1967). Methods of Contour Integration. Amsterdam: North-Holland Publishing Company.
[12] Rasulov, M.A., & Sinsoysal, B. (2008). Residue method for the solution of heat equation with nonlocal boundary condition. Beykent University Journal of Science and Technology, 2, 146–158.
[13] Sinsoysal, B., & Rasulov, M.A. (2008). Residue method for the solution of a 2d linear heat equation with nonlocal boundary condition. Int. J. Contemp. Math. Sciences, 3(34), 1693–1700.
[14] Sinsoysal, B. (2009). Residue method for the solution of wave equation with nonlocal boundary condition. Beykent University Journal of Science and Technology, 3, 74–81.
[15] Sinsoysal, B., & Rasulov, M.A. (2013). Residue solution of system of differential equations and its application to RC circuit problem. Beykent University Journal of Science and Technology, 6, 1–9.
[16] Sinsoysal, B., & Rasulov, M.A. (2020). One method to prove of existence weak solution of a mixed problem for 2D parabolic equations. Partial Differential Equations in Applied Mathematics, 1, 100002. https://doi.org/10.1016/j.padiff.2020.100002
[17] Tamarkin, J. (1928). Some general problems of the theory of ordinary linear differential equations and expansion of an arbitrary function in series of fundamental functions. Mathematische Zeitschrift, 27, 1–54.

September 2024, Vol:2, Issue:2

International Journal of New Findings in Engineering, Science and Technology

journal homepage: *https://ijonfest.gedik.edu.tr/*

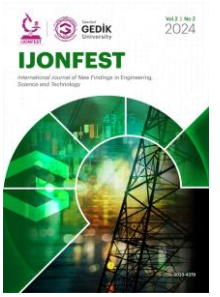

IMPLEMENTING THE STREAMLINE CURVATURE METHOD FOR PRELIMINARY DESIGN OF MULTISTAGE AXIAL COMPRESSORS

Rafis Mukhamediarov [a*], Hadi Genceli [a]

[a] *Department of Mechanical Engineering, Yildiz Technical University, Istanbul, Turkey,*
[*] *Corresponding author's email address: RafisMukhamedyarov@gmail.com*

Abstract

This study presents a modified algorithm for the inverse calculation of a multistage axial compressor using the established streamline curvature method. The algorithm was applied to design a four-stage axial compressor with a pressure ratio of 3.2 and an estimated efficiency of 88.6%. Numerical simulations of the designed compressor were performed, showing good agreement with the calculated values at the mean diameter, with deviations within 5%. The temperature distribution along the radial direction was predicted accurately, while some discrepancies in pressure prediction near the hub were observed due to the approximate nature of the loss models used. The study provides recommendations for improving the calculation methodology and confirms the reliability of the proposed modifications to the design method. These findings enhance the preliminary design process for axial compressors, contributing to their efficiency and reliability.

Keywords: Axial Compressor; Streamline Curvature Method; Inverse Solver; Preliminary Design.

1. INTRODUCTION

In modern gas turbines, the axial compressor is an essential part. Aerodynamic design and optimization need a thorough understanding of its flow characteristics and performance across a wide variety of operating situations. Three-dimensional computational fluid dynamics (CFD), the one-dimensional approach, and the through-flow method are the main computational techniques employed in compressor research. The one-dimensional approach skips the in-depth flow study in favor of concentrating on the general traits and functionality of the compressor stage [1].

The streamline curvature method is a standard tool used for the design and analysis of turbomachinery, particularly in the context of designing axial multistage machines. The use of the streamline curvature method as applied to analysis in multistage axial compressors was described by Jansen and Moffatt[2], Aungier [3], Campsty [4], and many other authors. Jansen and Moffatt [2] represent an early foundational study in the designing axial multistage machines. References [3] and [4] are relatively modern seminal texts that comprehensively detail

https://doi.org/10.61150/ijonfest.2024020204

axial multistage compressors' theory and design methodologies. Banjac [5] provided a reasonably detailed description of the design methodology using the streamline curvature method. Suppose the body and sleeve geometry are modified in that design throughout the calculation process. In that case, the only thing that changes in this work is the blades' edge positions, which will be covered in more detail below.

Existing methodologies [3,4] typically propose conducting the compressor calculation sequentially from section to section along its flow path. However, an appealing approach is the method of calculating parameters simultaneously considering all sections. This approach simplifies the computation of partial derivatives of compressor parameters and avoids nested loops in the calculation program. Nevertheless, this method has a drawback: ensuring the stability of the solution process becomes more challenging. When solving the inverse problem, the complexity increases because geometry updates of the compressor are required at each iteration, which can lead to computational instability.

It is vital to enhance inverse solvers made specifically for compressor design in order to enhance the features of axial compressors. Early-stage design solvers that consider a wide range of parameters influencing the machine's efficiency are required. Studying the inverse solver's algorithms, as well as the physical processes taking place in the compressor's flow section, are necessary to do this.

In compressor design, it is crucial to select loss models appropriately and consider parameters such as incidence angles, deviation angles, and blockage factors. For instance, inaccurately calculated losses or blockage factors may result in meridional velocity variations from the design values. This mismatch in compressor stage operation lowers the compressor's efficiency and surge margin. Improper distribution of losses along the blade height can result in insufficient performance near the casing, leading to flow degradation and boundary layer separation.

In this paper, we propose an original algorithm for the inverse calculation of multistage axial compressors. This algorithm addresses some of the challenges by updating only the position of the blade edges during the calculation process, which aims to enhance computational stability. The proposed algorithm has been applied to the design of a four-stage axial compressor, showing promising results that suggest its potential effectiveness.

2. MATERIAL AND METHODS

2.1 Radial equilibrium equation

The streamline curvature method is based on the radial equilibrium equation. This method does not take into account viscous effects and assumes an axisymmetric flow [4]. Figure 1 presents a fluid flow diagram in the meridional plane with the designation of the coordinate system.

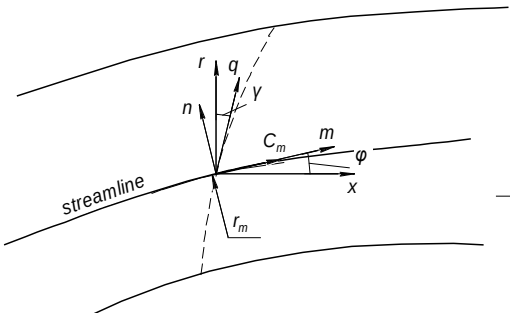

Figure 1. Coordinate system for streamline curvature method calculation

The equation is shown below in the generally recognized form [4], except that the term that accounts for blade forces in the radial direction is missing in this particular case. It is possible to ignore this term in the axial compressors.

$$\frac{1}{2}\frac{\partial}{\partial q}C_m^2 = \frac{\partial h_0}{\partial q} - T\frac{\partial s}{\partial q} + C_m\frac{\partial C_m}{\partial m}\sin(\phi+\gamma) - \frac{C_m^2}{r_m}\cos(\phi+\gamma) - \frac{1}{2r^2}\frac{\partial}{\partial q}\left(r^2C_u^2\right) \quad (1)$$

In this case, the variables are: ϕ is the angle between a stream-surface and the compressor axis; γ is the angle between the quasi-normal and the plane perpendicular to the compressor axis; C_m is the meridional velocity; C_u is the circumferential velocity; h_0 is the total enthalpy; and s is the entropy.

2.2 Calculation procedure

Upon completing the compressor calculation based on the mean diameter, the shape of its flow path is determined. Subsequently, a two-dimensional axisymmetric calculation is necessary to ascertain the flow kinematics along the blade height of the compressor. To achieve this, a computational grid is generated (Figure 2a) for further calculation based on the obtained geometry of the flow path. During the first iteration, the blade width is assumed to be constant along the height and equal to the value obtained from the mean-line calculation. The blade width depends on the chord of the blade and the stagger angle of the blade profile, which in turn is completely determined by the flow kinematics. Then, in each subsequent iteration, the blade width is refined for each section, and based on this refinement, the position of the nodes of the computational mesh is updated.

The calculation process is as follows:

1) Initially, the positions of the stream surfaces are estimated. Typically, they are arranged to divide the surfaces formed by the rotation of quasi-normals into surfaces of equal area.

2) Angles ϕ and the curvature of the stream surfaces r_m are determined at the intersection points with the quasi-normals. Then, by interpolation, the values of these parameters are determined at the grid nodes (Figure 2b).

3) Values of the angle γ are determined at the grid nodes.

4) In the initial approximation at the first iteration, the values of the meridional velocity C_m and entropy s are assumed constant with height, derived from mean-line calculation results. On each subsequent iteration, these values are taken from the calculation results of the previous iteration. A relaxation coefficient may be applied for calculation stabilization.

5) Values of the total enthalpy h_0 and velocity C_u are determined at each node. At the rotor inlet, C_u is determined based on the twist law, while at the rotor outlet, it is determined to ensure the required work at the given rotor radius.

6) Terms of equation 1 are evaluated at each point. Then, by integrating equation 1, updated values of C_m are determined for each point. The boundary condition for integrating the equation is taken as the value of velocity C_m at the mean diameter.

7) Using the new values of C_m, losses are evaluated for each blade section, and the entropy s is updated.

8) The flow rate through each quasi-normal is calculated, and the values of C_m are updated to ensure the specified flow rate through each quasi-normal. This may be accomplished by multiplying all of the C_m values in the current quasi-normal by a coefficient that is the same as the ratio of the specified flow rate to the calculated flow rate.

9) If necessary, the blockage factors are updated. Here, a relaxation coefficient may also be used to ensure calculation stability.

10) Blade width values are updated, and based on this, the position of grid nodes is updated.

11) The positions of the stream surfaces are updated to ensure flow continuity in each stream tube formed by adjacent stream surfaces.

12) Residuals are evaluated, and if necessary, the calculation is repeated from step 2.

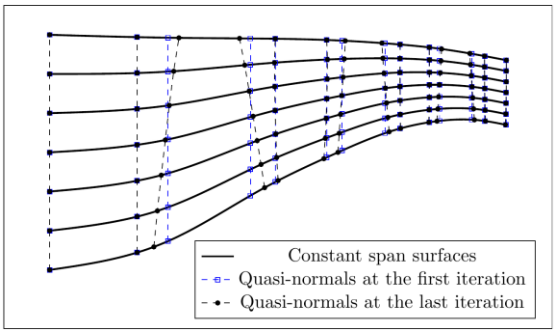

(a) Illustration of node position update

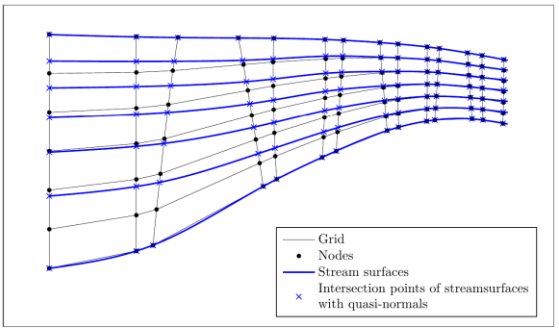

b) Illustration of intersection points between stream surfaces and quasi-normals

Figure 2. Computational grid

2.3 Loss Correlations

The loss coefficient is calculated from the drag coefficient, which in turn is composed of coefficients of resistance caused by various types of losses:

$$\bar{\omega} = C_D \sigma \frac{\cos^2 \beta_1}{\cos^3 \beta_m}$$

$$C_D = C_{Dp} + C_{Da} + C_{Ds} + C_{Dt}$$

where $\bar{\omega}$ is loss coefficient, C_D – total drag coefficient, C_{Dp} – drag coefficient from profile losses, C_{Da} – drag coefficient end-wall losses C_{Ds} – drag coefficient from secondary losses, C_{Dt} – drag coefficient from tip clearance losses, σ – row solidity at mean diameter, β_1 – inlet flow angle at relative frame, β_m – averaged flow angle which calculated as:

$$\beta_m = \arctan\left(\frac{\tan\beta_1 + \tan\beta_2}{2}\right)$$

where β_2 is the outlet flow angle at the relative frame.

Profile losses are estimated using the widely accepted Lieblein's model [6]:

$$C_{Dp} = 2\left(\frac{\theta_2}{l}\right)\left(\frac{\cos\beta_m}{\cos\beta_2}\right)^3\left(\frac{2H_2}{3H_2 - 1}\right)\left[1 - \left(\frac{\theta_2}{l}\right)\frac{\sigma H_2}{\cos\beta_2}\right]^{-3}$$

where β_m – averaged flow angle at the relative frame, β_2 – outlet flow angle at the relative frame, σ – row solidity at mean diameter, H_2 – boundary layer shape factor, θ_2 – blade wake momentum thickness, c – blade chord.

The prediction of endwall losses and secondary losses is based on the Howell model [7]:

$$C_{Da} = 0.02\frac{s}{H}$$

$$C_{Ds} = 0.018C_L^2$$

where s is blade pitch, H – blade height, C_L – lift coefficient.

An empirical model has been used to estimate losses from leakage in the radial gap:

$$C_{Dt} = 0.29\bar{t}C_L^{1.5}$$

here $\bar{t}$ is the relative tip gap, C_L – lift coefficient.

The lift coefficient is calculated as:

$$C_L = \frac{2}{\sigma}\left(\tan\beta_1 - \tan\beta_2\right)\cos\beta_m$$

where σ is row solidity at mean diameter β_1 – inlet flow angle at relative frame, β_2 – outlet flow angle at relative frame, β_m – averaged flow angle.

2.4 Designed compressor parameters

The main parameters of the designed compressor are given in Table 1. The compressor is a four-stage compressor with a pressure ratio of 3.2. At this pressure ratio, the compressor stages are usually lightly loaded and usually provide fairly high efficiency. Based on one-dimensional calculations, the estimated efficiency is 88.6%. The air mass flow rate is 50 kg/s, which corresponds to a medium-sized compressor. The relative hub diameter in the first stage is 0.5, which provides a balance between compressor performance and acceptable efficiency.

Table 1. Compressor main parameters

Parameter	Unit	Value
Number of stages	[-]	4
Mass flow rate	[kg/s]	50
Pressure Ratio	[-]	3.2
Isentropic Efficiency	[-]	0.886
Shaft Speed	[RPM]	9550
Inlet Hub-Tip Ratio	[-]	0.5

Figure 3 shows the meridional cross-section of the compressor flow path. During the calculation, the end diameter was chosen as the determining one, and this diameter decreased by 4% from the compressor inlet to the outlet.

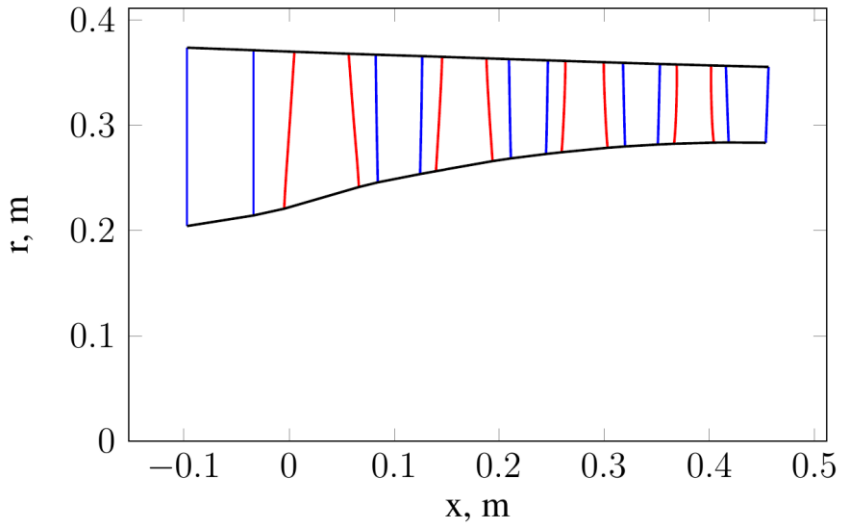

Figure 3. Compressor flow path

Table 2 presents the main parameters of the compressor stages. Figure 4 shows the distribution of pressure ratio, isentropic efficiency of the compressor stages and the equivalent diffusion factor of the compressor rows.

The flow coefficients were selected from values from 0.5 to 0.59. These values provide an axial velocity of 174.6 m/s at the entrance to the first stage rotor and 160 m/s at the exit from the compressor. The outlet flow angles in the stators of the first and second stages are 16 degrees, which ensures an acceptable degree of reaction and, accordingly, increased efficiency of the stages. At the third stage, this angle is 12 degrees, which makes it possible to achieve acceptable efficiency values and, at the same time, reduce the load on the final stage stator by decreasing the flow angle behind the final stage rotor.

Table 2. The compressor stage's main parameters

	Unit	IGV	1st stage	2nd stage	3rd stage	4th stage
Blade speed at mean diameter	[m/s]	-	296	310.4	317.5	320.1
Blade corrected speed at mean diameter	[m/s]	-	296	292.3	284.4	275.4
Total temperature rise	[K]	-	36.6	34.4	30	26.3
Axial velocity at the inlet	[m/s]	149.2	174.6	172.2	168.3	160
Work coefficient	[-]	-	0.42	0.36	0.3	0.26
Flow coefficient	[-]	-	0.59	0.555	0.53	0.5
Stator outlet flow angle	[°]	12	16	16	12	2
Rotor de-Haller Number	[-]	-	0.709	0.727	0.749	0.765
Stator de-Haller Number	[-]	1.196	0.787	0.764	0.764	0.767

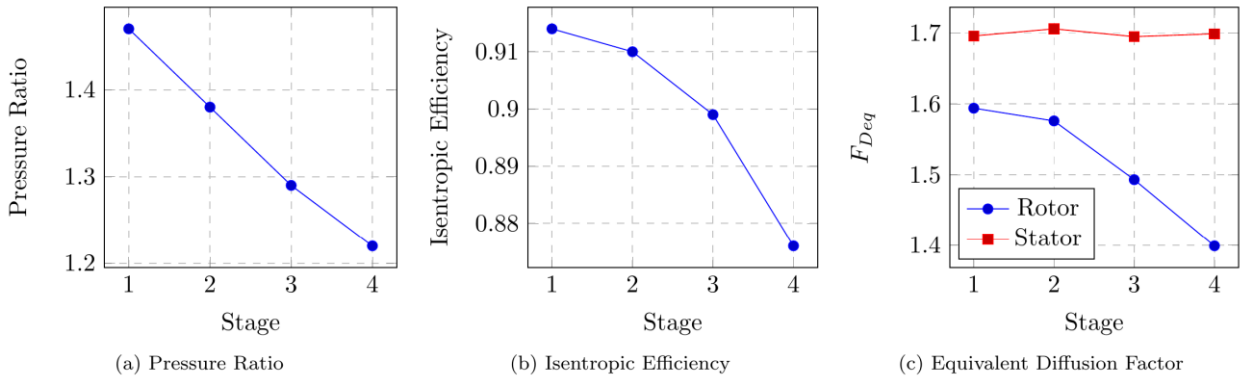

Figure 4. Stages parameters

Work coefficients were also selected to ensure high-stage efficiencies but were adjusted to limit the aerodynamic loading of the stators to $F_{Deq}=1.7$. Since the stators of the third and fourth stages have to correct the flow, swirled in the first two stages, their aerodynamic load increases, so the rotors of these stages are underloaded. Accordingly, if the temperature increased by 36.6 and 34.4 degrees in the first two stages, respectively, in the third stage, it will climb by 30 degrees and by just 26.3 degrees in the second stage.

The speed of the blades at the mean diameter is moderate, from 296 to 320 m/s, which makes it possible to manufacture the compressor rotor from inexpensive materials. The corrected blade speed at the mean diameter varies from 296 m/s at the inlet to 275.4 m/s at the outlet. These values correspond to transonic stages.

2.5 CFD modeling

Based on the results of aerodynamic calculations, the compressor blades were profiled, and a 3D model of the aerodynamic surfaces was created. DCA profiles were used for the rotor blades and IGV blades, and NACA65 profiles [7] were used for the stator blades. The resulting 3D model is shown in Figure 5.

The Ansys CFX [9] software package was used for the numerical simulation of the flow in the compressor. This package allows for the calculation of RANS (Reynolds-Averaged Navier-Stokes) equations using the finite volume method.

A high-quality hexahedral mesh was generated in TurboGrid. The number of elements per row ranged from 0.5 to 2.0 million. Near the walls, the mesh was refined so that the thickness of the first element was between 3 and 5 microns, ensuring y+ values of less than 5. A radial clearance of 0.5 mm was implemented on the rotor blades. Figure 6 shows the resulting mesh. The total number of elements was 9.2 million, and the number of nodes was 9.54 million.

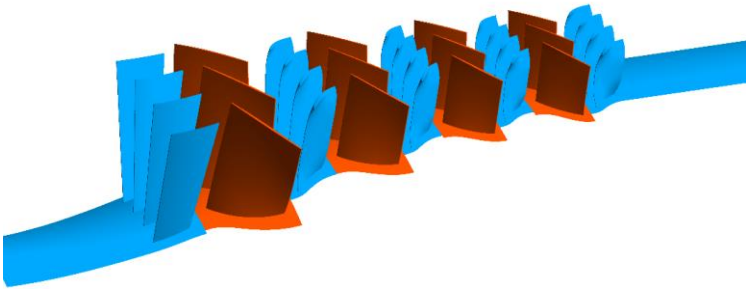

Figure 5. 3D model of the designed compressor

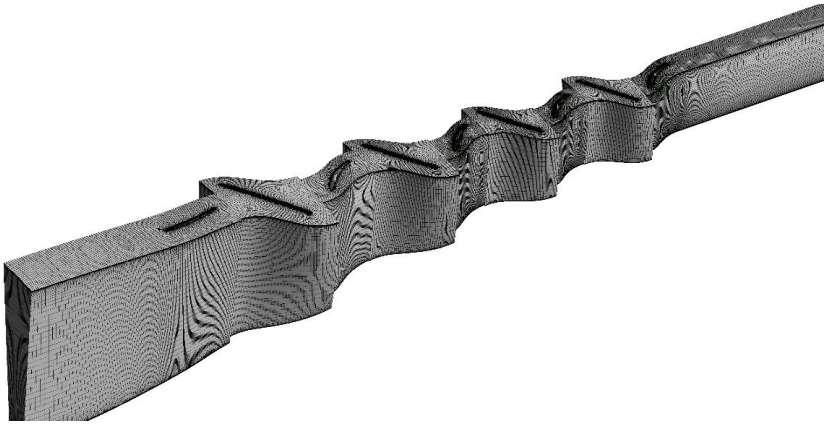

Figure 6. Computational mesh

The full energy model is used in the simulation. The turbulence model is SST. A periodic boundary condition allows the calculation to consider only one interblade passage. The boundary condition for the walls is a no-slip condition. At the inlet, the total pressure is set to 101.325 kPa and the total temperature to 288.15 K, while the outlet has an average static pressure of 290 kPa. The rotation speed of the computational domain is set to 9550 RPM. The convergence criterion is that the root mean square residuals reach a level of 1e-4.

3. RESULTS AND DISCUSSION

Table 3 presents the integral parameters of the compressor obtained as a result of numerical simulation in comparison with the design values. Despite the blockage coefficients taken into account during the design, the flow deficit was 3.6%, which is likely due to incorrect calculation of the channel blockage and incorrectly selected angles of attack in the rotor of the first stage of the compressor. The shortfall in efficiency was 1.6%, which is not much for preliminary design. The deviation of the pressure ratio from the design value was -2.81%.

Table 3. Integral Parameters

	Unit	Design	CFD	Rel. diff.
Mass Flow	[kg/s]	50.0	48.2	-3.60%
Isentropic efficiency	[-]	0.886	0.870	-1.81%
Pressure ratio	[-]	3.20	3.11	-2.81%

In Figure 7, the calculation results for the hub, middle and tip sections of the compressor are presented in the form

of Mach number fields and vector fields. From these figures it is clear that in the middle and end sections the flow proceeds without areas of developed boundary layer separation, while in the hub section there are areas with intense boundary layer separation in the stator rows. It can also be noted that there are areas with pronounced shock waves in the first stage rotor, where the temperature is the lowest.

The graphs (Figure 8) illustrating the distribution of total pressure and temperature indicate that in the first stage, above the mean diameter, the work performed exceeds the design specifications. Further, in the second and third stages, the pressure curve somewhat levels out in the flow core, while at the core of the blades there are strong dips in the total pressure due to the presence of boundary layer separation in these zones. In the fourth stage, the total pressure over the entire height is below the design value. It should be noted that there is a drop in total pressure already behind the first stage, which can cause degradation of the flow in the area of the end-walls and, therefore, a rapid increase in the thickness of the boundary layer and its separation [10].

Regarding the distribution of the total temperature, it should be noted that in all stages there is approximately the same difference from the design values in the area of the end walls, which is probably caused by mixing processes in the boundary layer, which were not taken into account during the design. The entropy distribution graphs show that there is an approximately constant difference with the design values, which indicates that the design did not take into account the uneven distribution of entropy at the entrance to the compressor, which could also cause degradation of the flow near the end walls further along the compressor flow path.

During the design process, it is essential to highlight that the distribution of losses with respect to height was somewhat inaccurate. In the event where the design of the entropy distribution curves is supposed to be parabolic, the modeling results show discrete linear portions in the entropy distribution curves for the initial three stages. However, in the final stage, characterized by enhanced mixing, the curve is notably smoothed and closely approximates the originally intended design shape.

Figure 9 shows graphs of the distribution of flow angles at the inlet and outlet for each row of the compressor, and Figure 10 shows graphs of the distribution of meridional velocity. It is evident from Figure 9a that the rotor's angle of attack was set wrong, which resulted in inadequate flow through the compressor. Judging by the other figures, this may also be true for the rotors of subsequent stages. To increase flow rate, it is recommended to increase the angles of attack for rotor cascades. If the stators of the first three stages level the flow over most of the blade height, while due to the intense separation of the boundary layer, the stator of the last stage provides kinematic flow parameters close to the design ones only in the flow core.

The meridional velocity distribution graphs demonstrate that there was a notable departure from the design values of the meridional velocity as early as the first stage entry. This divergence was most noticeable in the vicinity of the hub wall. This effect only increases further along the compressor flow path. This deviation from the design parameters could also cause increased losses at the bushing and, as a result, degradation of the flow closer to the compressor outlet.

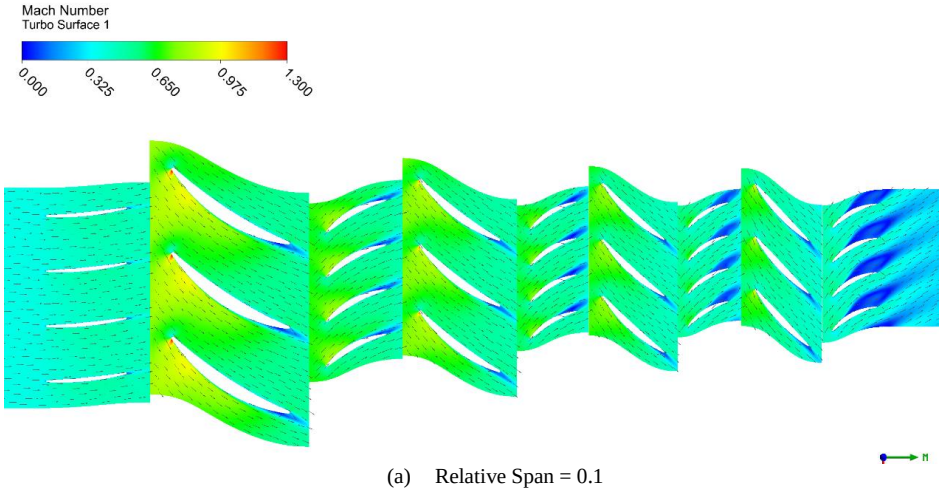

(a) Relative Span = 0.1

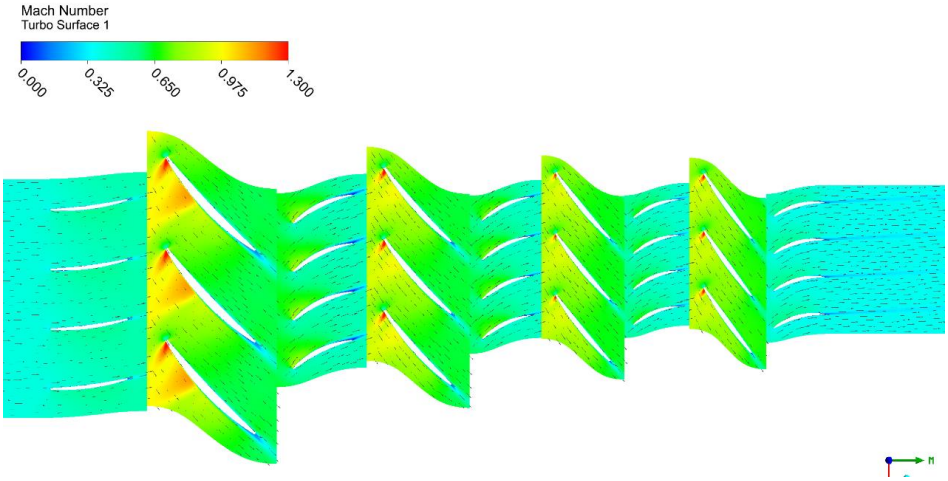

(b) Relative Span = 0.5

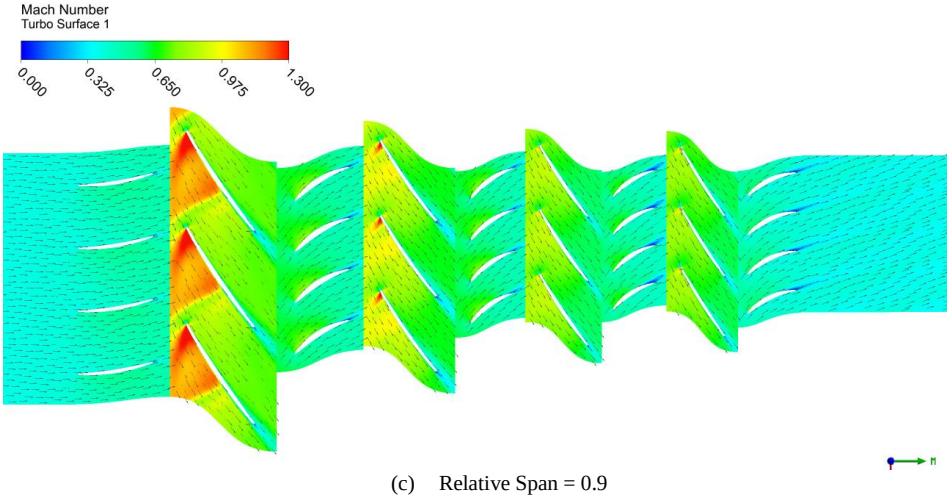

(c) Relative Span = 0.9

Figure 7. Mach number fields and vector fields

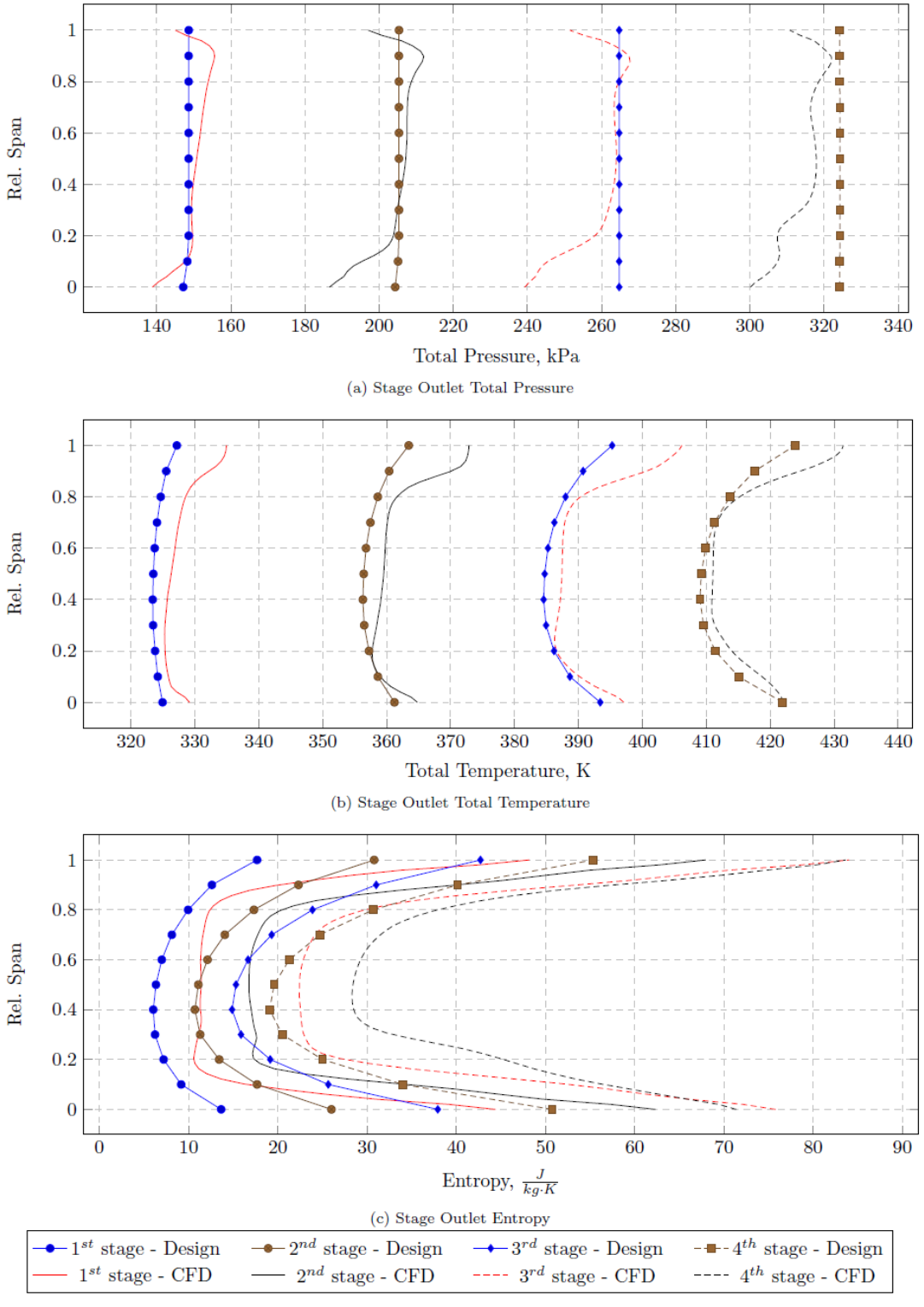

(a) Stage Outlet Total Pressure

(b) Stage Outlet Total Temperature

(c) Stage Outlet Entropy

Figure 8. Thermodynamic parameters

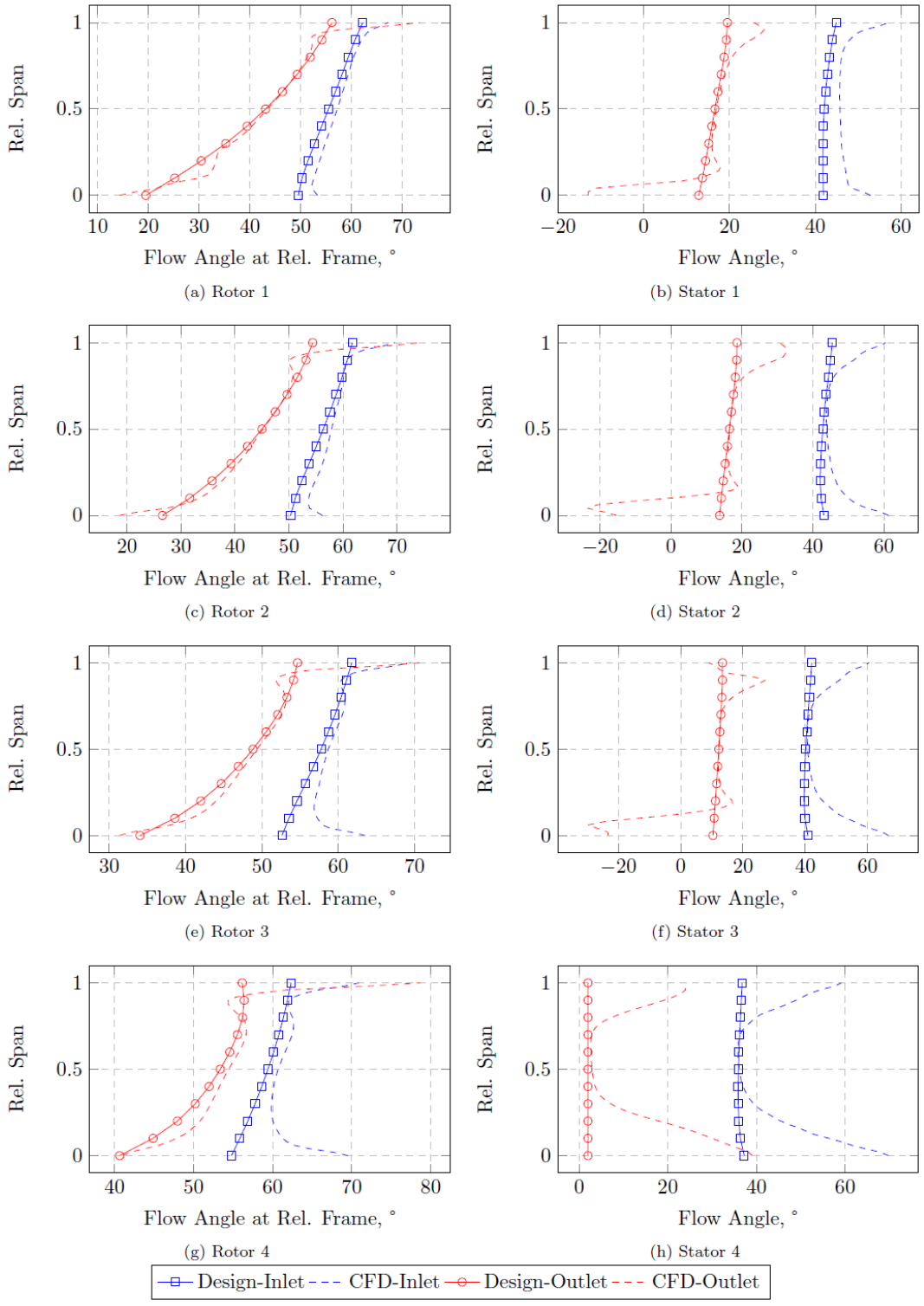

Figure 9. Flow angles

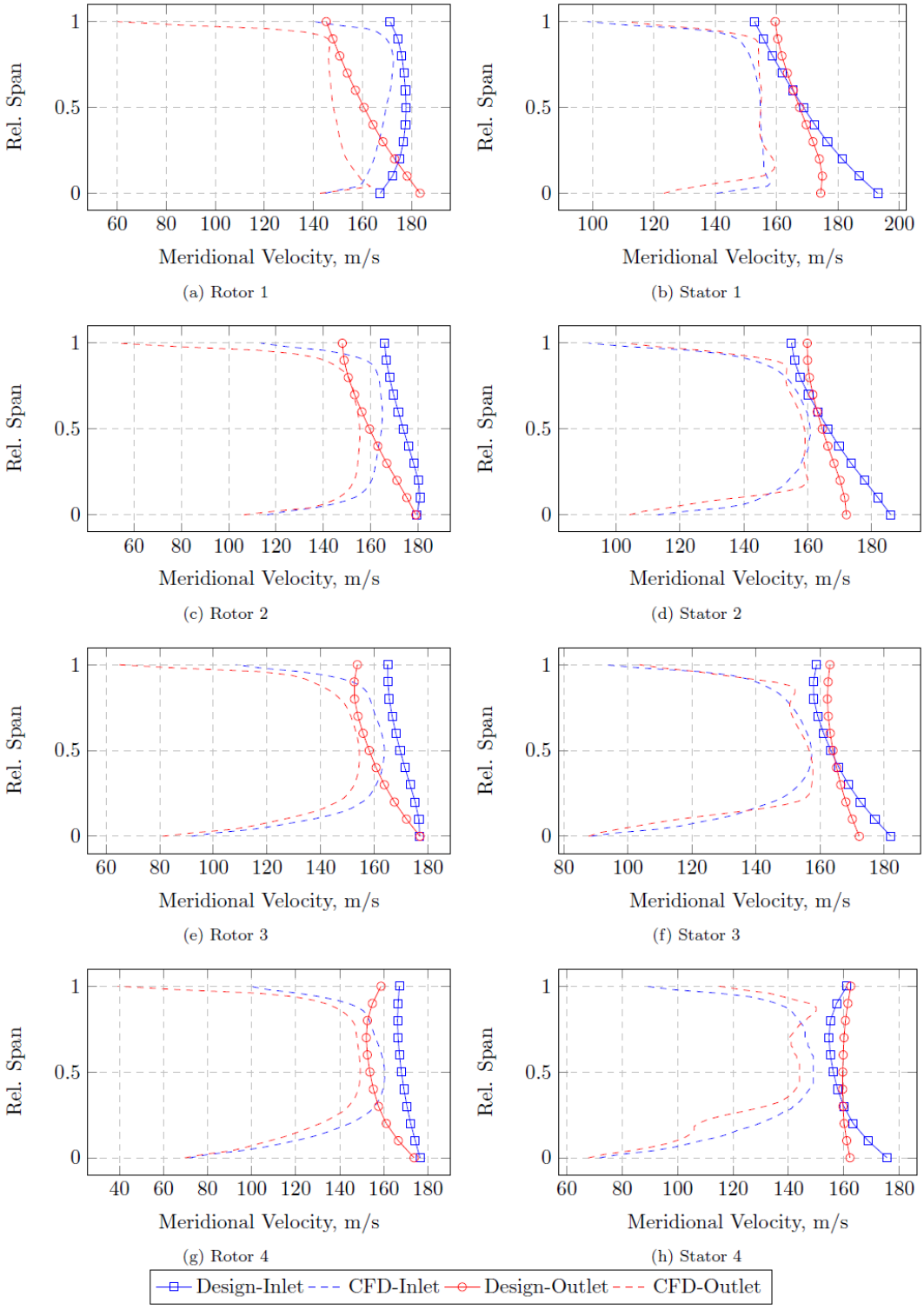

Figure 10. Meridional velocity

4. CONCLUSION

This study focused on the development and application of an inverse calculation algorithm specifically designed for the design of multistage axial compressors. The main task was to develop a four-stage axial compressor with a pressure ratio of 3.2

We proposed an inverse calculation algorithm to determine the geometric and aerodynamic parameters of multistage axial compressors based on specified target parameters. The algorithm was applied in the design of a four-stage axial compressor. Comprehensive numerical simulations were carried out to evaluate the performance of the designed compressor. This simulation provided a detailed understanding of the flow pattern and overall compressor efficiency. Numerical modeling results showed deviations from the design values: the mass flow rate deviation was -3.6%, the pressure ratio deviation was -2.81%, and the isentropic efficiency deviation was -1.81%.

Additionally, there were local deviations in the thermodynamic and kinematic parameters from the design values caused by the following reasons:

- Inaccurate estimation of channel blockage.
- Incorrectly selected incidence angles in the compressor rotors.
- Improper distribution of losses along the blade height.

These factors led to flow degradation along the compressor's flow path, resulting in boundary layer separation from the hub surface.

Despite these issues, the developed software code allows for the preliminary design of a compressor with parameters close to the design values. However, to improve the program, the following recommendations are made:

- Advanced Channel Blockage Prediction: Use more advanced methods for predicting channel blockage, such as calculating the boundary layer on the end walls of the compressor.
- Enhanced Loss Models: Employ more sophisticated loss models, particularly regarding their distribution along the blade height. This could involve implementing three-dimensional loss models that account for secondary flows and other complex phenomena.
- Meticulous Angle of Attack Selection: Conduct a more meticulous selection of angles of attack. This can be achieved through more precise optimization algorithms and taking into account the variable flow conditions across different stages.
- Consider Blade Height Mixing: It is recommended to take into account blade height mixing, which is especially important for compressors with more than 3-4 stages. This consideration can help accurately predict and mitigate adverse flow effects.

By implementing these recommendations, the accuracy and reliability of the compressor design process can be significantly improved, resulting in higher efficiency and better overall performance.

Future research will focus on calibrating loss models and accurately distributing these losses along the blade height. Additionally, the calculation of the boundary layer on the end walls of the compressor will be a key area of study to better estimate flow path blockage. Furthermore, modifications will be made to the computational code to account for mixing effects, which is essential for the accurate design and analysis of multistage compressors.

References

[1] Tao, L., Yadong, W., & Hua, O. (2020). Performance Prediction of Transonic Axial Compressors Using Improved Streamline Curvature Approach. Fluid Dynamics, 55(1), 121–132.
[2] Jansen, W., & Moffatt, W. C. (1967). The off-design analysis of axial-flow compressors.
[3] Aungier, R. H. (2003). Axial-flow compressors. American Society of Mechanical Engineers, New York.
[4] Cumpsty, N. A. (1989). Compressor aerodynamics. Longman Scientific & Technical.
[5] Banjac, Milan & Petrovic, Milan. (2018). Development of Method and Computer Program for Multistage Axial Compressor Design: Part II — Two-Dimensional Design and Validation Using CFD. V02CT42A008. 10.1115/GT2018-75412.
[6] Lieblein, S., 1959. “Loss and Stall Analysis of Compressor Cascades”. ASME Journal of Basic Engineering, 81, pp. 387–400.
[7] Schobeiri, M. (2005). Turbomachinery flow physics and dynamic performance (p. 153). Berlin: Springer.
[8] Bogdonoff, S. M. (1948). NACA Cascade Data for the Blade Design of High-Performance Axial-Flow Compressors. Journal of the Aeronautical Sciences, 15(2), 89-95.
[9] ANSYS, 2010. ANSYS CFX-Solver Theory Guide. ANSYS Inc, Canonsburg.
[10] Statrtsev, A.N. (2021). Аэродинамическое проектирование осевого компрессора [Design of an axial compressor aerodynamics]. Aircraft Engines 3(12), 19-34.

September 2024, Vol:2, Issue:2

International Journal of New Findings in Engineering, Science and Technology

Journal homepage: *https://ijonfest.gedik.edu.tr/*

Mechatronics System Design and Implementation of a Pneumatic Hand Rehabilitation Device

Emre Tuğberk Gülnergiz[a*]

[a]*Department of Mechatronics Engineering, Istanbul Gedik University, Turkey e-mail:tugberk.gulnergiz@gedik.edu.tr*
*(*Corresponding Author)*

Abstract

This study presents the development of a mechatronic device for an additively manufactured Pneumatic Artificial Muscle (PAM) rehabilitation orthosis. Within this scope, the system's electro-pneumatic, mechanical, control, and software designs have been designed and implemented. The device, intended to directly interact with both patients and therapists within the bio-mechatronic process, is equipped with an intuitive graphical user interface (GUI). Utilizing a FlexSensor to measure hand flexion/extension angles, the device employs a solenoid valve, along with a trigger relay, for the inflation and deflation of the orthosis. During the electronic design phase, challenges such as interference and latency were mitigated through the implementation of isolations in the design. Employing a PD (Proportion-Derivative) control loop on the ATmega328 microcontroller, control parameters were determined empirically. By excluding a compressor pump inside the device, a lightweight, portable, and cost-effective system was accomplished. While potential enhancements discussed in the conclusion will be considered in future studies, the current prototype effectively fulfills the project objectives.

Keywords: Pneumatic Artificial Muscle; Hand Rehabilitation; Mechatronic System Integration

1. INTRODUCTION

When reviews in the field of robotic hand rehabilitation are examined, it is observed that a large portion of the studies involve the application of similar methods in different forms. Particularly, several complex methods have been adopted, especially in terms of power transmission and actuation techniques. The advantages and disadvantages of these methods in relation to each other and traditional physical therapy techniques have been extensively studied and presented in various works as shown in **Figure 1**.

https://doi.org/10.61150/ijonfest.2024020205

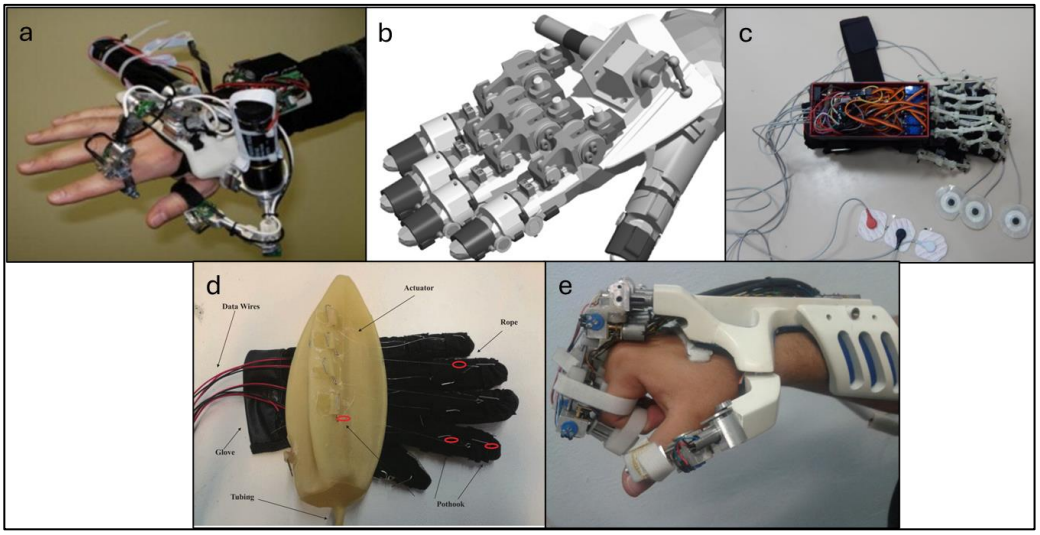

Figure 1. Some Examples of Mechatronics Hand Rehabilitation Devices [1-5].

When studies on hand/finger extension are examined, it is evident that the products are largely unidirectional, lacking active exercise (type of exercise involving the patient's active movements), and feature complex designs. Therefore, based on expert advice and research findings, it has been concluded that the robotic hand rehabilitation orthosis to be developed should include the following elements: the capability for passive hand/finger extension and active hand/finger flexion exercises; a simple, user-friendly design that appeals to a wide range of users and provides tactile sensory input (skin sensation); and a low-cost manufacturing technology that can be customized as needed.

In this context, instead of traditional McKibben artificial muscles, PAM via additive manufacturing was considered. In addition to all the advantages offered by McKibben artificial muscles, flexible and custom designs for different purposes [6,7] could be rapidly and affordably produced.

As seen in the **Hata! Başvuru kaynağı bulunamadı.**, design preferences were made among designs with different geometric parameters through preliminary design and computer-aided modeling phases conducted considering biomechanical requirements, along with finite element analyses and the details have been previously published [8-10]

This paper focuses on the development of the mechatronic system, which integrates the previously designed orthosis with the necessary electronic and control components to create a functional rehabilitation device. The following sections will detail the methodology used in the development of this system, including system integration, and control mechanisms.

2. METHODOLOGY

As seen in the methodological flowchart presented in **Hata! Başvuru kaynağı bulunamadı.**, an additive manufacturing methodology was adopted to produce the preferred design according to the desired specifications as shown in **Figure** 3**Hata! Başvuru kaynağı bulunamadı.**. **Hata! Başvuru kaynağı bulunamadı.** Following the design and manufacturing phases, a complete mechatronic system integration was carried out to work in conjunction with the orthosis, thus preparing the ground for its analysis and rehabilitation studies.

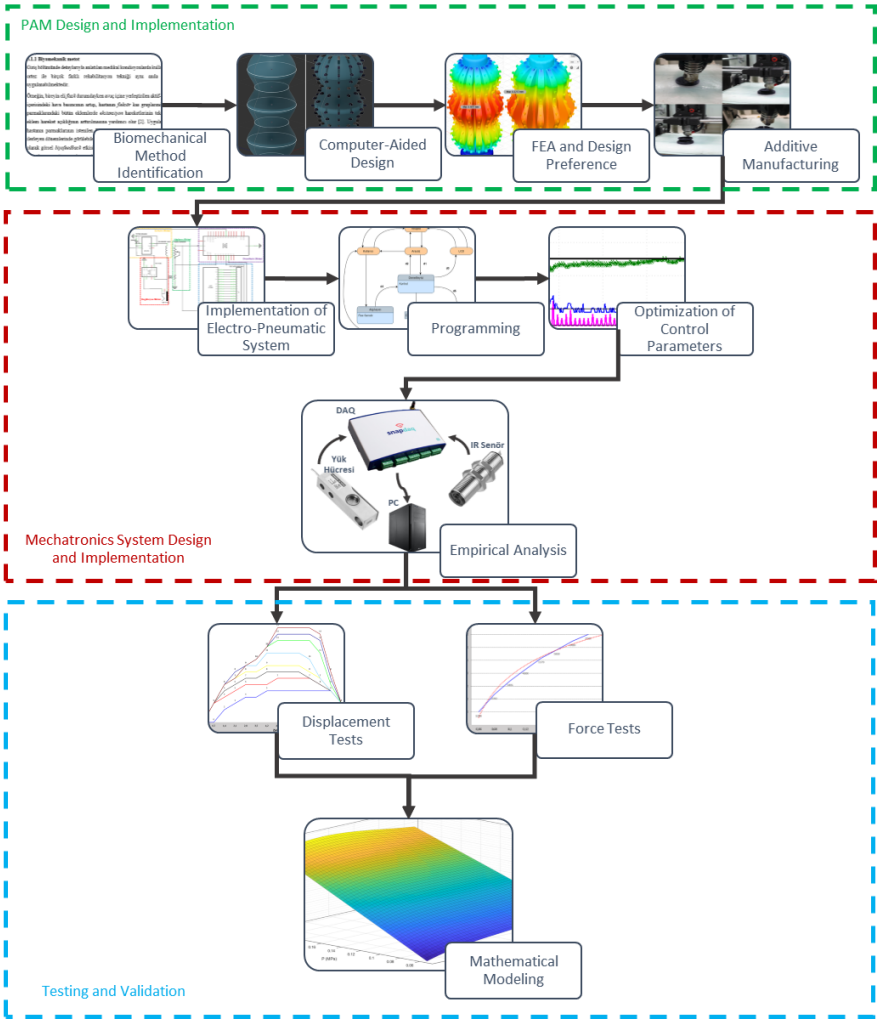

Figure 2. Methodological Flowchart.

The software carrying the system's operating algorithm was integrated into the system with a user interface, and the parameters of the preferred controller type were determined using this system through empirical methods. After the completion of system integration, parallel experimental analyses were conducted alongside finite element analyses, the details of which have been published previously [8-10], and a mathematical model was established based on these analyses.

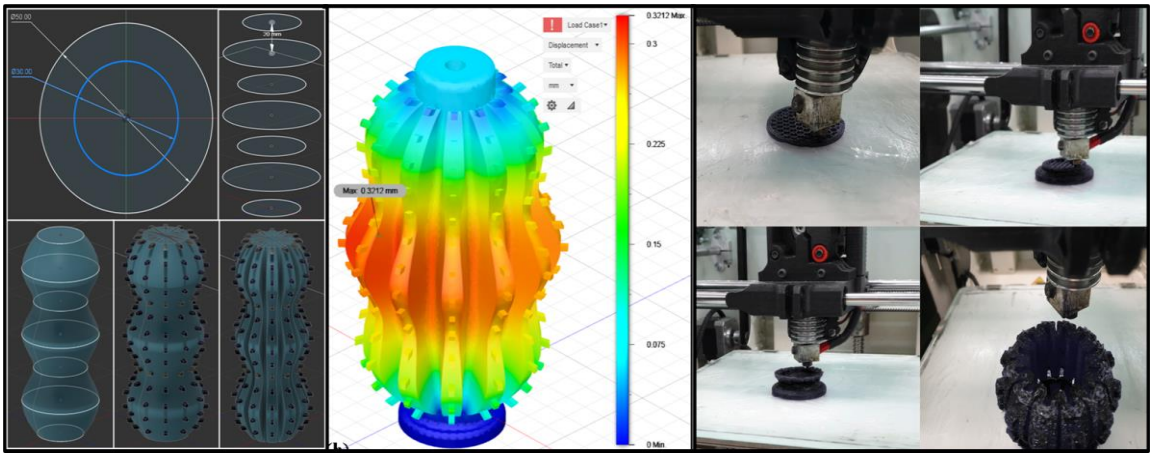

Figure 3. The Design, Analysis, and Production Phases of The Orthosis [8-10].

The implementation process of the bio-mechatronic system was generally divided into 5 sections: actuator unit, I/O unit sensor unit, control unit, therapist, and patient. The Data Flow Diagram (DFD) and the bio-mechatronic sub-systems are presented in Figure 4. In the Input/Output unit, an LCD screen is used as an output, while the Graphic User Interface (GUI) is used as an input and output tool. These input/output tools will facilitate the control of the rehabilitation device for the therapist. The actuator unit includes components such as the trigger relay, solenoid valve, and pneumatic orthosis necessary for the device to perform mechanical work. In the system's sensing unit, a flex sensor is included to analogically measure hand extension and flexion amounts. The control of all units and the data processing are carried out on the Atmega328 central controller.

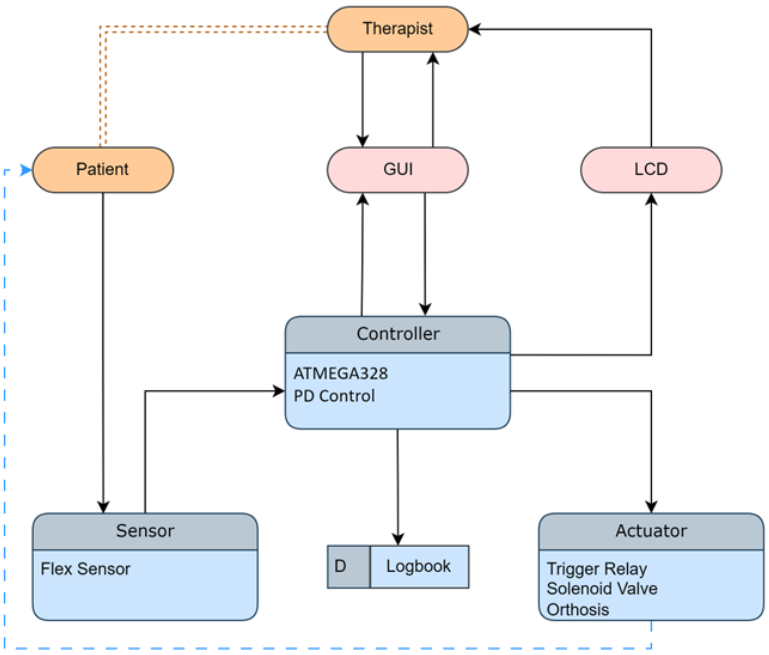

Figure 4. DFD of the Bio-Mechatronic System.

2.1 Electronic Design

The main sensing element used in the closed-loop control of the rehabilitation device is a flex sensor. The 4.5" long sensor is long enough to measure the cylindrical grasping movement of a normal human hand and can operate without the need for an additional amplifier circuit, using only an input resistor. The flex sensor in the system's sensing unit measures hand aperture in real-time and sends it to the controller. The controller then processes the data according to the control algorithm and sends relevant triggers and/or information to the actuator and the I/O units. Although a relatively simple power/control mechanism would suffice to meet the requirements described in the introduction section, the structure of the control algorithm, as discussed in the next section, has brought along some physical application challenges. To overcome these challenges, a few additions have been made to the electronic design. As seen in Figure 5, while all components in the circuit operate with direct current, a voltage regulation unit has been added to the circuit due to the voltage differences between the components. However, as also shown in the same figure, the MP1584 integrated voltage regulator in the circuit is used not for supplying all components operating at 5V but only for powering the triggering relay.

Although the 1.8-amp output current of the MP1584 voltage regulator would be sufficient to power all 5V components in the circuit, this approach has been taken as the relay and solenoid valve are inductive elements. The rapid switching of inductive elements in the circuit leads to the generation of reverse EMF (electromotive force), interference on the electronic circuit, and high voltages due to induction currents.

These parasitic effects and fluctuations on the load negatively affect various parts of the system, including the USB interface used for communication with the central processor and the LCD screen controller communicated via the I2C protocol. For these reasons, only the inductive elements have been powered by the MP1584 (Figure 5), and additionally, the trigger relay has been opto-isolated , and the I2C controller has been protected with a flyback diode and decoupling capacitor. The ATmega328 has been chosen as the main controller of the system due to its 16MHz clock speed and 32 KB ISP flash memory [11].

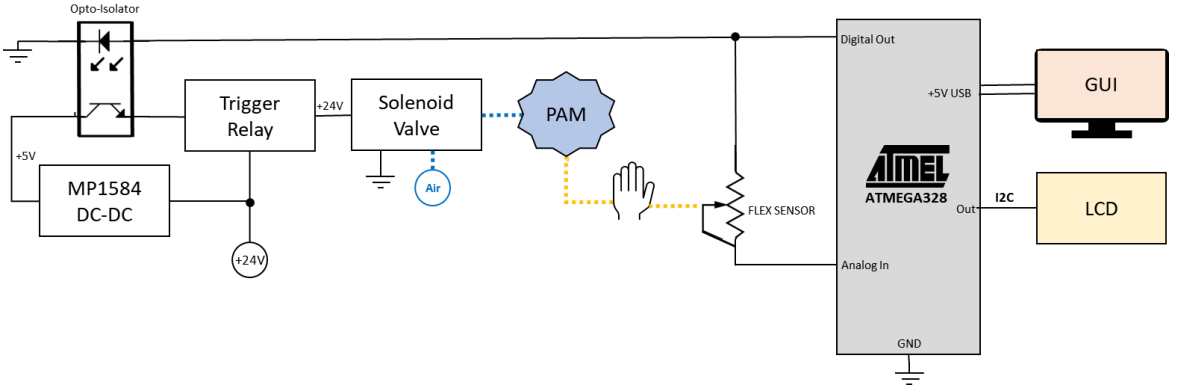

Figure 5. Electronic Circuit Diagram.

2.2 Control

Although the relay and solenoid valve used to activate the orthosis are digital components, the flex sensor used as the main sensor in the system provides analog outputs according to the degree of bending. In similar cases, the widely preferred PD control technique has also been chosen in this study as shown in Figure 6.

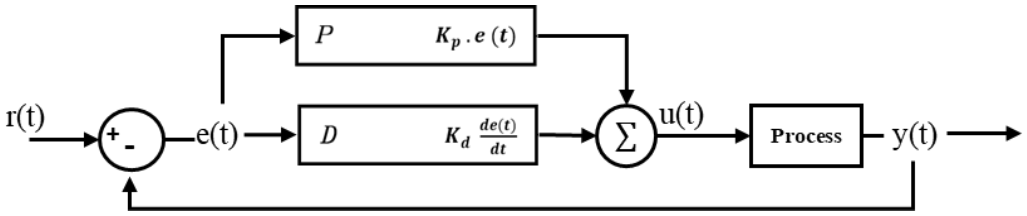

Figure 6. Control Diagram.

For the determination of the K_p, and K_d coefficients of the controller, empirical methods used in the literature [12-15] were reviewed concerning Rise Time, Overshoot, Settling Time, and Steady State Error. In this context, the coefficients presented in the study by Heidari et al. [16] were initially considered as the starting point for coefficient determination. Later, the final values of the coefficients were determined through experimental methods as shown in Figure 7.

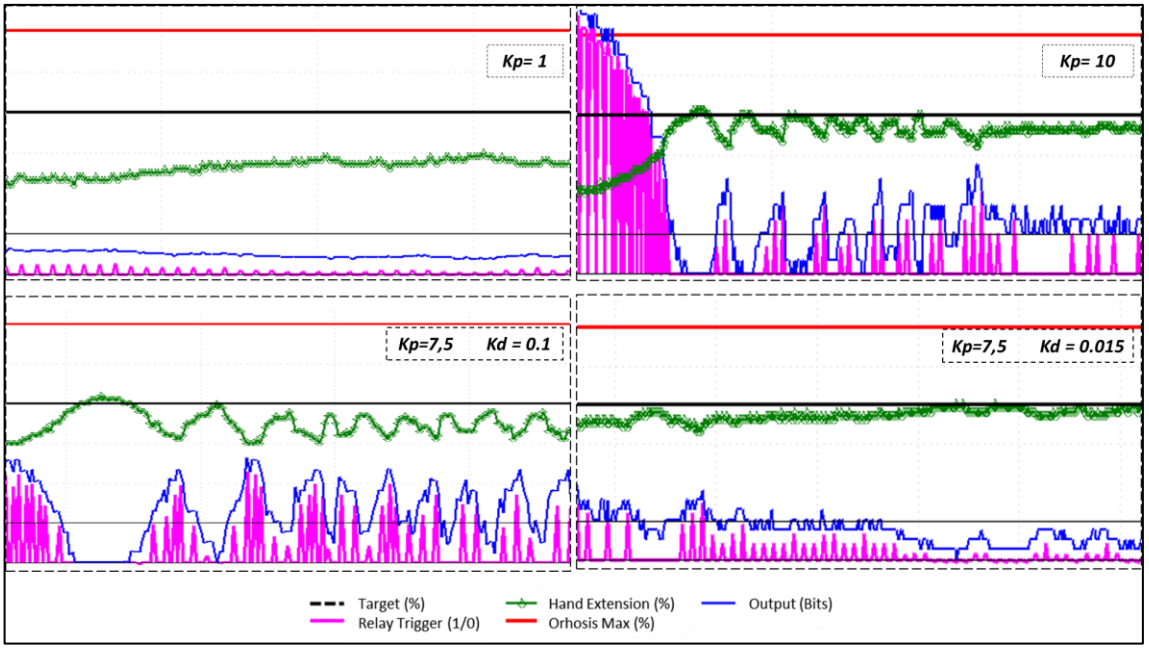

Figure 7. Controller Tuning.

2.3 User Interface

The graphic user interface (GUI) of the system, consisting of 4 main sections, is presented in Figure 8. In the Calibration section, the therapist must "reset" the system before starting the session. After the patient has put on the orthosis in its deflated state, pressing the "Calibrate" button will save the current angle value read by the sensor as the base angle value for the controller. This allows the system to record the patient's joint degree in flexion enabling to work based on this reference. Then, the therapist will select the size of the orthosis worn by the patient as the pneumatic orthosis can be manufactured in different diameters and parameters for various patient groups (young, elderly etc.). This selection will be saved and the predefined maximum expansion angle parameter for the selected orthosis will be used as a limit during the process.

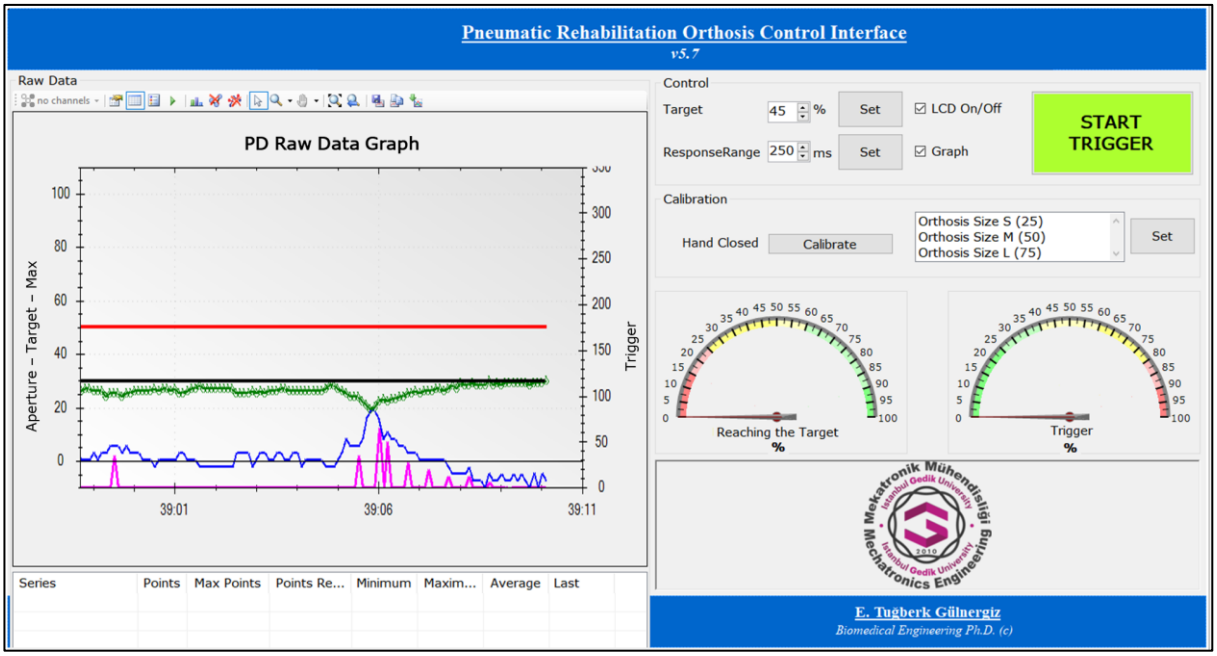

Figure 8. Graphical User Interface (GUI).

In the Control section, the therapist can adjust the “Target” and “Response Range” values. Additionally, he or she can control the LCD screen, view the raw data graph, and start or stop triggering. The Response Range parameter is crucial for the controller and generally determines the response sensitivity of the device. If it is determined that the output from the control loop is greater than the previously set "Response Range," the relay is triggered.

This range, which directly affects the system's behavior, has a default starting value but can be easily and instantly adjusted by the therapist. The "Target" value represents the percentage of hand aperture that the therapist aims to achieve during that therapy session. This percentage is calculated using the base value set in the calibration section and the limit value that can be reached by the selected orthosis size. For example, the hand being as closed as it was in the initial state represents 0%, while the hand being fully extended to the maximum angle the orthosis can inflate represents 100%.

Additionally, the "Start/Stop Triggering" button under the same group allows the therapist to perform system adjustments/calibrations without triggering any pneumatic actuation during therapy sessions and shut down the system when the session is complete. The user interface provides two dial gauges to the therapist, displaying the triggering amount and the percentage of reaching the target. Additionally, since this system is a prototype, there is a graph screen in the interface where all raw data is shown and logged into the logbook.

3. RESULTS AND DISCUSSION

The completed rehabilitation device is presented in Figure 9. As this system is a prototype, further optimization steps are needed for commercialization or mass production.

The device, excluding the orthosis, has a total weight of approximately 500 grams and has been produced in a compact and portable form. A computer is required for the operation of the device. While some summary data can

be accessed directly through the LCD screen during the system's operation (Figure 10), the device does not have any input method for adjustments, making it impossible to operate independently from a computer. In future studies, the LCD screen on the device will be replaced with a TFT LCD Touch Screen, allowing the device to function as a standalone system for basic rehabilitation and exercises.

Figure 9. The Final Prototype

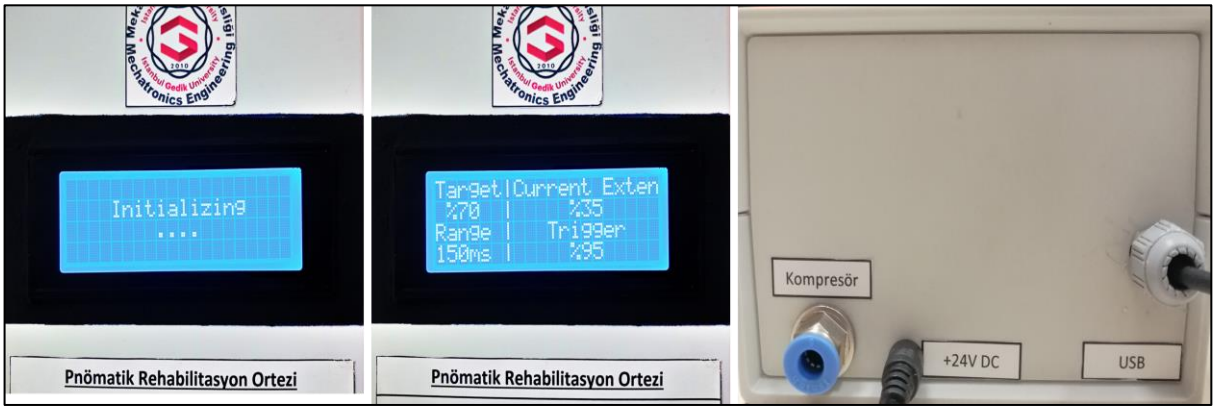

Figure 10. LCD Screen and Connections

Similarly, the device's electrical and compressed air supplies are expected to be provided from external sources as shown in Figure 10. Although the maximum operating pressure of PAM orthoses produced by additive manufacturing is 0.2 MPa, due to the size and weight of compressors that can meet this requirement, they have not been included in the system. In future studies, it is possible to produce a version of the device with a built-in compressor motor.

As shown in Figure 11, the device tests have been successfully completed with different orthoses. The approximate total hardware cost of the prototype, which is around $100, makes this device quite accessible for patients, therapists, and institutions. Thanks to its simple design, patients can acquire this device to perform daily hand exercises without therapist supervision if they choose to do so.

Figure 11. Testing of the Prototype

The integrated logbook in the system has been prepared to provide meaningful data to both patients and therapists. These data will be beneficial for tracking the progress of patients during the therapy process. Additionally, for potential commercialization and mass production, adding retrospective data analysis and patient tracking features to the software would be advantageous.

The control parameters of the system have been determined through experimental methods. Although the current performance of the controller in reaching the target is deemed sufficient, future studies plan to adopt a more systematic approach to extract the parametric model of the system.

4. CONCLUSION

In this study, a mechatronic device has been developed for an additively manufactured PAM rehabilitation orthosis. The device, which will interact directly with the patient and therapist in the bio-mechatronic process, has been integrated with an easy-to-use GUI. The device uses a flex sensor to measure the flexion/extension angles of the hand, and a solenoid valve, in series with a trigger relay, is used for inflating and deflating the orthosis. During the electronic design of the device, issues such as interference and latency were addressed by adding isolations to the design. The device applies a PD control loop on the ATmega328 microcontroller, and the control parameters were determined using an empirical method. Although the improvements mentioned in the discussion section will be included in future studies, the prototype currently meets the project objectives.

Acknowledgements

This study was conducted as part of a master's thesis under the supervision of Assoc. Prof. Dr. Savaş Dilibal. Previous publications related to the thesis are presented in the bibliography.

Funding

There is no financial interest in this study.

Declaration of Competing Interest

There is no conflict of interest in this study.

References

[1] Iqbal, J., Khan, H., Tsagarakis, N. G., & Caldwell, D. G. (2014). A novel exoskeleton robotic system for hand rehabilitation – conceptualization to prototyping. *Biocybernetics and Biomedical Engineering*, *34*(2), 79–89. https://doi.org/10.1016/j.bbe.2014.01.003

[2] Chiri, A., Vitiello, N., Giovacchini, F., Roccella, S., Vecchi, F., & Carrozza, M. C. (2012). Mechatronic design and characterization of the index finger module of a hand exoskeleton for post-stroke rehabilitation. *IEEE/ASME Transactions on Mechatronics*, *17*(5), 884–894. https://doi.org/10.1109/tmech.2011.2144614

[3] Abdallah, I. B., Bouteraa, Y., & Rekik, C. (2017). Design and development of 3D printed myoelectric robotic exoskeleton for hand rehabilitation. *International Journal on Smart Sensing and Intelligent Systems*, *10*(2), 1–26. https://doi.org/10.21307/ijssis-2017-215

[4] Li, H., & Cheng, L. (2017). Preliminary study on the design and control of a pneumatically-actuated hand rehabilitation device. *2017 32nd Youth Academic Annual Conference of Chinese Association of Automation (YAC)*. https://doi.org/10.1109/yac.2017.7967530

[5] Sandoval-Gonzalez, O., Jacinto-Villegas, J., Herrera-Aguilar, I., Portillo-Rodiguez, O., Tripicchio, P., Hernandez-Ramos, M., Flores-Cuautle, A., & Avizzano, C. (2016). Design and development of a hand exoskeleton robot for active and passive rehabilitation. *International Journal of Advanced Robotic Systems*, *13*(2), 66. https://doi.org/10.5772/62404

[6] Dilibal, S., Gulnergiz, E. T., Pagliarani, N., Donato, E., Iori, F., Setti, E., Falotico, E., & Cianchetti, M. (2022). Grasping of li-ion batteries via additively manufactured Soft Gripper and collaborative robot. *2022 International Congress on Human-Computer Interaction, Optimization and Robotic Applications (HORA)*. https://doi.org/10.1109/hora55278.2022.9799902

[7] Gulnergiz, E. T., Dilibal, S., Gormus, B., Danquah, J. O., & Emon, O. F. (2023). Additively manufactured soft pneumatic gripper integrated remotely operated underwater vehicle (ROV) for grasping archeological remains. *2023 5th International Congress on Human-Computer Interaction, Optimization and Robotic Applications (HORA)*. https://doi.org/10.1109/hora58378.2023.10156774

[8] Gulnergiz, E. T., & Dilibal, S. (2022). Experimental and numerical analysis of additive manufactured pneumatic artificial muscle hand rehabilitation orthosis. *2022 Innovations in Intelligent Systems and Applications Conference (ASYU)*. https://doi.org/10.1109/asyu56188.2022.9925499

[9] Gülnergiz, E.T. (2019). Katmanlı İmalat Yöntemiyle Üretilmiş Çoklu Serbestlik Dereceli Pnömatik Rehabilitasyon Ortezi, *Turkey Robotics Conference (ToRK)*, 64–69. ISBN: 978-605-5625-16-0.

[10] Gülnergiz, E. T. (2020). *Eklemeli İmalatla Üretilmiş Pnömatik Yapay Kas ile El Rehabilitasyon Ortezi Mekatronik Sistem Tasarımı* (thesis).

[11] *Atmega328*. Microchip. (2020). https://www.microchip.com/en-us/product/atmega328

[12] Philip, M. S., Krishna, B., & Meenatchisundaram, S. (2018). Identification of empirical model and tuning of PID controller for a level control system. *Engineering Vibration, Communication and Information Processing*, 385–397. https://doi.org/10.1007/978-981-13-1642-5_35

[13] Bucz, Š., & Kozáková, A. (2018). Advanced methods of PID controller tuning for specified performance. *PID Control for Industrial Processes*. https://doi.org/10.5772/intechopen.76069

[14] Jenkins, H. (2016). *Tuning for PID Controllers*. Lecture, Macon; Mercer University. Retrieved from https://faculty.mercer.edu/jenkins_he/.

[15] Åström, K. J., & Murray, R. M. (2008). *Feedback systems: An introduction for scientists and Engineers*. Princeton University Press.

[16] Heidari, M., & Homaei, H. (2014). Improving the pneumatic control valve performance using a PID controller. *Turkish Journal of Engineering and Environmental Sciences*, *38*, 240–247. https://doi.org/10.3906/muh-1301-8

September 2024, Vol:2, Issue:2

International Journal of New Findings in Engineering, Science and Technology

journal homepage: *https://ijonfest.gedik.edu.tr/*

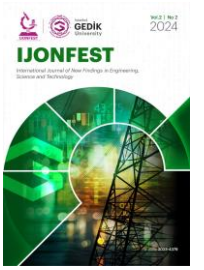

Monte Carlo simulation of distance-dependent quantum entanglement in mixed XXZ Heisenberg spin-1/2 chains

İzzet Paruğ DURU[a*], Şahin AKTAŞ[b]

[a]*Istanbul Gedik University, Medical Imaging Technics Program, Istanbul, Türkiye e-mail:parug.duru@gedik.edu.tr(*Corresponding Author)*
[b] *Marmara University, Faculty of Science, Department of Physics, Istanbul, Türkiye e-mail:saktas@marmara.edu.tr*

Abstract

The quantum entanglement of mixed XXZ Heisenberg spin-1/2 chain is examined. We quantify localizable entanglement (LE) in terms of upper/lower bounds through Quantum Monte Carlo simulations. Loop algorithm is chosen to numerically calculate thermodynamic quantities including spin-spin correlations. The exchange coupling, Zeeman energy, and dipolar interaction are taken into account. Findings summarize that the strength of dipole-dipole interaction (D) and external magnetic field (Bz) are notable in entanglement formation driving the creation and extinction of entanglement. The creation and extinction of entanglement depend on D and Bz. Furthermore, strong fields at critical temperatures lead to a non-monotonic/monotonic behavior introducing revival phenomena. Nevertheless, strong D provides the distance-dependent stability of LE values, preserving unity.

Keywords: Mixed magnetic state; Quantum entanglement; Monte Carlo simulation; Revival phenomena; Critical temperature.

1. INTRODUCTION

A significant information resource is provided by entanglement, which is a notable aspect of executing quantum information operations like quantum teleportation [1-3] and quantum computation [4-9]. Since their literal and straightforward construction makes them ideal for studying entanglement and strong correlations, Heisenberg and Ising-like models, determining the magnetic state of a spin system [10, 11], have been notably preferred. Additionally, a remarkable number of studies revealing magnetic characterization and particularly spin-spin correlations have been performed [12-19]. Since 1D-spin arrays, which considerably incorporate entangled states, can be presented as a credible choice for quantum information operations, have exhaustively concentrated on the Heisenberg Hamiltonian introducing quantum spin-1/2 chains [20-23]. Additionally, they concentrated on the concurrence of mixed states of two qubits. Wang concludes that zero-field concurrence has unity at low temperatures until T = 0.2, and vanishes at T = 1.1 [24]. For an isotropic XY chain, however, a quantum phase transition for a critical value of B is observed at zero temperature [25].

https://doi.org/10.61150/ijonfest.2024020206

For the isotropic XXX model (J = 1), entanglement disappeared at T = 0.9, according to Rigolin's calculations [26]. In addition to measuring the concurrence of the two nearby spins, multi-particle entanglement can yield useful information between distant pairs of spins. An eligible measurement tool is LE. Androvitsaneas et al. seek a close relation between LE and anisotropy in the case of XY and XYZ models in the absence/presence of the applied magnetic field reporting Bz = 0.75 as a quantum critical point. Besides, rival regions under specific magnetic fields and thermal agitations are displayed for the 10 closest neighboring spins [27]. Spherical nanostructures are dressed with dipoles by Sinyagin et al. to ascertain the aggregation of the considered structure [28]. A strong argument for ~~a~~ topological storage may be ensured through inevitably long-distant entangled couples [29]. However, [30] examined the two-qubit long-range entanglement and revealed the coupling of qubits across long distances. There is also a wealth of possible research material for several long-ranged interacted systems [31-41]. Several experimental investigations utilizing low-dimensional quantum-spin models have been conducted to explore the characteristics of quasi-particle excitations [39, 40, 42]. Sahling evaluates the first example of entangled spins in bulk materials at relatively low temperatures [43].

In theory, it is necessary to comprehend quantum phase transitions in the context of condensed matter physics [44-46]. The dipole-dipole interaction under transverse magnetic field stressing a quantum phase transition on antiferromagnetic (AFM) spin chains is underlined by Bravo et al. [46]. We have previously concentrated on quantifying LE of an AFM spin-chain taking the dipolar interaction (D) and the external magnetic field (Bz) into account. Rival zones are connected to the temperature for specific values of D and Bz [47]. Under a uniform external magnetic field (Bz), this work highlights the impact of dipole-dipole interaction (D) on the upper and lower bounds of entanglement in isotropic ferromagnetic spin-1/2 Heisenberg chains. The ALPS package [48] is preferred to calculate and simulate the model by loop algorithm to specify LE in terms of upper and lower bounds. LE is a useful tool to figure out how much a multipartite system is entangled, measuring bipartite entanglement. It quantifies the average maximal entanglement between two parts of the system by performing local measurements throughout the rest of the system [49-51]. LE and the entanglement of assistance are connected (EoA). The authors have built a Phyton script for post-processing simulation data. Our objective is to address the impact of dipolar interaction on LE using numerical methods. Additionally, we sought to measure the entanglement of long-ranged neighboring spins in multipartite systems.

In this article, the Hamiltonian and expectation values using a loop algorithm and Quantum Monte Carlo techniques are described in Section 2. In Section 3, the determination of upper and lower bounds of localizable entanglement is discussed. Temperature, spin-spin interaction, strength of dipolar interaction, and additionally external magnetic field are taken into consideration related to the n neighboring spins. Section 4 includes a summary of the findings.

2. MODEL & METHOD

2.1 Background of Loop Algorithm

The Loop algorithm [57-59], has been first developed in “Lattice 91” (Tsukuba, Japan) as a Quantum Monte Carlo procedure. It overcomes almost all the difficulties of world-line algorithms by considering non-local changes in the world-line configuration determined by local stochastic decisions. Moreover, it can be comprehensively applied to numerous models, including stochastic series expansion (SSE) [60-62], and the imaginary time world lines formulation [63]. It corresponds to the cluster algorithms developed by Swendsen-Wang [64] in a classical statistical system. Main features: autocorrelations are reduced, it can be easily formulated for continuous time Monte Carlo (by eliminating the Trotter approach), and observables can be formulated in terms of loop features by reducing the errors of the quantities measured with Improved Estimators. Besides, non-diagonal operators can be measured with advanced evaluators and the sign problem can be overcome (especially in fermionic systems). However, it can be coded more easily than traditional worldlines.

S_p, given in Equation 1, corresponds to the possible spin local configurations where eigenvalues are $S_{i,j}^z = \mp 1/2$ constrained through z direction.

$$S_p \equiv (S_{i,j}^z, S_{i+1,j}^z, S_{i,j+1}^z, S_{i+1,j+1}^z) \quad (1)$$

The statistical weight of the entire possible configurations can be represented by $W(s_P)$ in a density matrix formalism. Equation 2 contains probable spin configurations including the Heisenberg Hamiltonian, $\hat{H}_i$, which operates spin-1/2 pairs exponentially.

$$W(s_P) \equiv \langle S_{i,j}^z, S_{i+1,j}^z | e^{-\Delta\tau \hat{H}_i} | S_{i,j+1}^z, S_{i+1,j+1}^z \rangle \quad (2)$$

The Hamiltonian cooperates with exchange coupling energy, dipole-dipole interaction, and Zeeman energy along the z-direction.

$$\hat{\mathcal{H}} = -\sum_{i=1}^{N} \left[J_x \hat{\sigma}_i^x \hat{\sigma}_{i+1}^x + J_y \hat{\sigma}_i^y \hat{\sigma}_{i+1}^y + J_z \hat{\sigma}_i^z \hat{\sigma}_{i+1}^z + B_z(\hat{\sigma}_i^z) \right] + \hat{\mathcal{H}}_D \quad (3)$$

$$\hat{\mathcal{H}}_D = \frac{D}{2} \sum_{i=1}^{N} \left[\frac{\hat{\sigma}_i \hat{\sigma}_{i+1}}{r_{i\,i+1}^3} - 3 \frac{(\hat{\sigma}_i . r_{i\,i+1})(\hat{\sigma}_{i+1} . r_{i\,i+1})}{r_{i\,i+1}^5} \right] \quad (4)$$

where $J_\alpha (\alpha: x, y, z)$ is exchange coupling constant, B_z and D represents the magnetic field along the z-axis and the strength of dipole-dipole interaction. The periodic boundary conditions (PBC) are satisfied declaring $\sigma_1 = \sigma_{N+1}$. The abovementioned statistical weight matrix evolves to Equation 5 when the graph configurations are conceptually considered.

$$W_p(S_p) = \sum_{G_p} W_p(S_p, G_p) \quad (5)$$

Gp is a graph variable that has particularly been defined in the plaquette. It has to satisfy $W_p(S_p, G_p) \geq 0$. Graph examples are shown in Figure 1. Gp=1, Gp=2, and Gp=3 graph variables represent the pair flip of any two spins at the edges. $Gp = 4$ indicates that the direction of all spins flips. It is also called a frozen breakup. The rest divides plaquettes into two parts. Frozen breakups induce larger clusters. Note that smaller clusters bring about efficient simulation. Hence, the transition probability to frozen breakups will be low. The graph variables are crucial to deciding whether a transition to a new four-spin state is allowed or not using $\Delta(S_p, G_p)$.

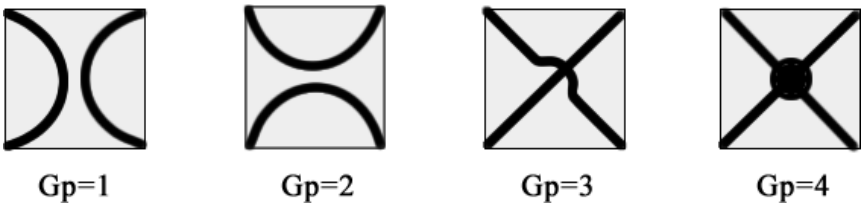

Figure 1. Plaquette breakups of 4-fold spin-1/2 states

The partition function, Z,

$$Z = \sum_S \prod_p W(S_p) = \sum_{S,G} \prod_p W_p(S_p, G_p) \quad (6)$$

$\sum_G$ summation expands the partition function over the entire possible configurations of the graph

variable. If a plaquette has N number of components, the number of breakups, Nb(N), is defined as in Equation 7 and Equation 8.

$$N_b(N) = \sum_k^N g(N,k) \tag{7}$$

$$\sum_{i=1}^{k} P_i g(N,i) = k^N \quad (k = 1,2,\dots,N) \tag{8}$$

If the spin orientation is changed for a certain breakup, there are multiple spin configurations obtained from a single one. The value of the graph variable Gp defines such a set of spin configurations. The number of GP states increases rapidly to O(αN). This is not very important since the number of states is small enough during the Monte Carlo simulation.

According to Fortuin [65] and Kasteleyn [66], $W(S_p, G_p)$ can be expressed as in Equation 9 where $v_p(G_p)$ is the graph weight of Gp.

$$W_p(S_p, G_p) = v_p(G_p)\Delta(S_p, G_p) \tag{9}$$

$$\Delta(S_p, G_p) = \begin{cases} 1, & S_p \in G_p \\ 0, & others \end{cases} \tag{10}$$

The conventional Monte Carlo Markov chain proposes $S^{(1)} \to S^{(2)} \to S^{(3)} \to \cdots$ in spin configuration space. The spin configuration space follows a graph configuration space in a Markov process of a clustering algorithm. ($S^{(1)} \to G^{(1)} \to S^{(2)} \to G^{(2)} \to S^{(3)} \to G^{(3)} \to \cdots$). The transition probabilities from spin to graphs are explicitly given in Equation 11 and Equation 12.

$$P(S \to G) \equiv \frac{\prod_p W_p(S_p,G_p)}{\sum_{G'} \prod_p W_p(S_p,G_p{}')} \tag{11}$$

$$P(G \to S) \equiv \frac{\prod_p W_p(S_p,G_p)}{\sum_{S'} \prod_p W_p(S'_p,G_p)} \tag{12}$$

$S \equiv \cup_p S_p$ and $G \equiv \cup_p G_p$, represent the global spin and graph configurations, respectively. Each local transition in a plaquette is determined via Equation 13.

$$P(S_p \to G_p) \equiv \frac{W_p(S_p,G_p)}{\sum_{G_p{}'} W_p(S_p,G_p{}')} \tag{13}$$

The transition probabilities noted below are consistent with the detailed balance condition. The probability of any S spin and G graph configuration is defined by Equation 14 and Equation 15.

$$P(S) = \frac{1}{Z}\sum_G \sum_P W_p(S_p, G_p) = \frac{1}{Z}\prod_p W_p(S_p) \tag{14}$$

$$P(G) = \frac{1}{Z}\sum_S \sum_P W_p(S_p, G_p) \tag{15}$$

Since G global graph configurations specify only how the spins are divided in the system, a spin configuration

can be determined among different configurations according to Equation 12. There are global differences between these spin configurations. In the Monte Carlo process, such a non-local spin orientation change is extracted by every local stochastic decision on every plaquette given by Equation 13. The algorithm that simultaneously updates the spins in clusters is called the cluster algorithm. The clustering algorithm has significant advantages over traditional local spin orientation change algorithms. The binary spin correlation function is identical to the probability function that tells us that these binary lattice points belong to the same cluster. Thus, the clustering algorithm significantly reduces the autocorrelation time between successful Monte Carlo configurations. To ensure ergodicity in quantum models, the Worldlines algorithm requires artificial global spin orientation variation. In the clustering algorithm, only natural global spin orientation variation is present. The loop algorithm can be implemented in both discrete imaginary time and continuous imaginary time. 8 possible quadruple spin configurations are shown in Figure 2.

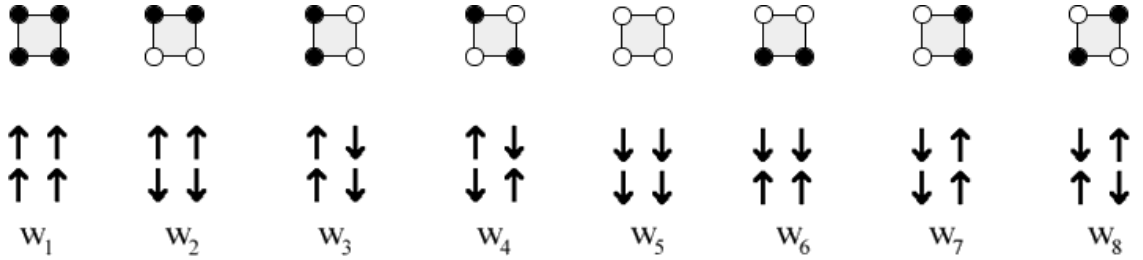

Figure 2. 8 possible 4-fold spin-1/2 states and their vertex weights (Wi): the black dots in the upper row represent upward spins and the white dots represent downward spins.

These configurations and plaquette breakups are illustrated in Figure 3, and Figure 4, respectively. Blackened arrows denote up-spins and gray arrows stand for the down-spins.

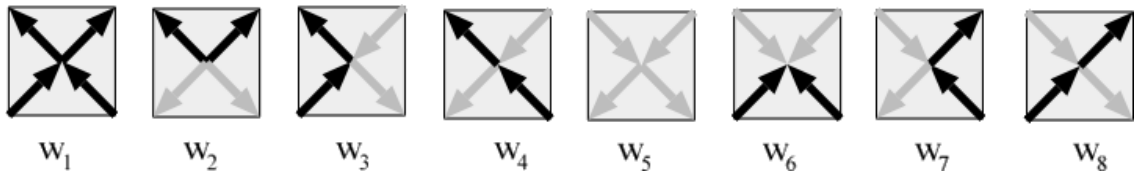

Figure 3. Vertex arrows representation of possible 4-fold spin-1/2 states

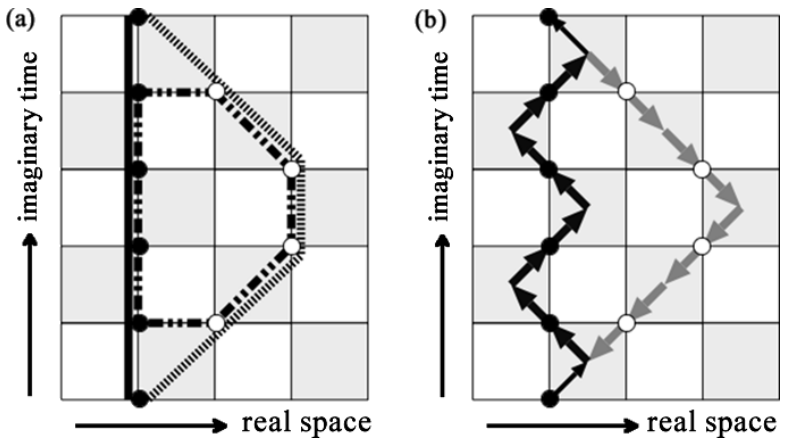

Figure 4. An example of an update of loop algorithm (a) worldline representation (b) vertex arrow representation

The thick solid line, in Figure 4(a), is a single world line. The dotted line represents a possible cycle. When the spins are reversed throughout the cycle, a dashed worldline is formed. The cycle here is not small enough to be local. Figure 4(b) illustrates the worldline with vertex arrows. The cycle is represented by thick arrows. In vertex representation, each cycle follows the arrows of the spin configuration. In other words, the cycle creates a worldline with upward spins along the imaginary time direction. Downward arrows do not create a world line. The most basic procedure of a Monte Carlo update of the loop algorithm consists of two stochastic mappings: from spins to spins and loops, thence to new spins. A breakup is selected for each shaded (gray) plaquette with the transition probability of the configuration of the spins in the selected plaquette. Clusters are established to create these breaks. When the directions of all arrows are changed along the cycle, each set is reversed with the appropriate probability. Thus, new spin configurations are formed. The value of the probabilities depends on the Hamiltonian and the previous spin configurations. The worldlines are continuous at every site along the Trotter direction due to the imaginary time-space $\Delta\tau \to 0$ ($\frac{\beta}{M} \to 0$) with an occasional jump to neighboring lattice sites. These jumps are instantaneous. $\hat{H}_i$, can be represented by Gp graph variables due to the infinitesimal imaginary time intervals.

$$\langle \varphi_j | \hat{H}_i | \varphi_{j+1} \rangle \equiv -\sum_{G_p} a_p(G_p)\Delta(S_p, G_p) - B_p(S_p) \tag{16}$$

$\Delta(S_p, G_p)$ is as defined in discrete imaginary time. $W_p(S_p)$, vertex weights, takes the form given in Equation 17 for each $\epsilon \equiv \Delta\tau \ll 1$ along continuous imaginary time.

$$W_p(S_p) \equiv \langle \varphi_j | e^{-\Delta\tau \hat{H}_i} | \varphi_{j+1} \rangle \approx e^{-\epsilon B_p(S_p)} \left[I_p(S_p) + \epsilon \sum_{G_p} a_p(G_p)\Delta(S_p, G_p) \right] \tag{17}$$

$I_p(S_p)$, is the unit operator in a plaquette. Taking $\Delta(S_p, 1) \equiv I_p(S_p)$, makes things easier. Taking the limit at $\epsilon \to 0$, a transition probability in a plaquette can be reduced to:

i. If the present S_p the state is consistent with $G_p = 1$ graph, for instance, spin splitting is not available at a $(t, t+\epsilon)$ time interval,

$$P(S_p \to G_p) = \epsilon a_p(G_p)\Delta(S_p, G_p) \qquad (G_p = 1)$$
$$P(S_p \to 1) = 1 - \sum_{G_p' \neq 1} P(S_p \to G_p') \tag{18}$$

ii. If the present S_p the state is inconsistent with $G_p = 1$ graph, for instance, the state at t is different from the state at $t+\epsilon$,

$$P(S_p \to G_p) = \frac{a_p(G_p)\Delta(S_p, G_p)}{\sum_{G_p' \neq 1} a_p(G_p')\Delta(S_p, G_p')} \qquad (G_p = 1)$$
$$P(S_p \to 1) = 0 \tag{19}$$

Eq.18 is applied to plaquette on worldlines along the Trotter direction. The probability of choosing a graph with $G_p \neq 1$ in the imaginary time interval. ϵ is determined by $\epsilon a_p(G_p)\Delta(S_p, G_p)$. In fact, G_p graphs are distributed over a uniform interval with a probability density such as $a_p(G_p)\Delta(S_p, G_p)$ in the continuity limit. On the other hand, Eq.19 specifies the probability expression with the graph relative to the point in time when two neighboring worldlines exchange or a local state change. Note that, the expression here is not probability density.

The loop algorithm in continuous imaginary time can be generally summarized as follows. For each pair of adjacent world lines,

i. $G_p(\neq 1)$ graphs, as in Equation 18, worldlines are distributed over each imaginary time interval in such a way that they are not overlapped.

ii. At each time point where states can be exchanged between two lattice points, a graph G_p is selected by Equation 19.

iii. $G_p = 1$ is assigned to the rest.

Then the spin values are updated by changing the clusters. This algorithm has some advantages over the loop algorithm in discrete imaginary time. The most important of these is that the need for Trotter extrapolation to reduce the systematic error arising from the finite Trotter number m in Suzuki-Trotter decomposition disappears in the continuity limit. Thus, KMC simulations become more convenient at low temperatures. Discrete imagery can sometimes be implemented more easily on computers than in real-time [57]. The 2-dimensional classical mesh in continuous imaginary time is shown in Figure 5 and Figure 6.

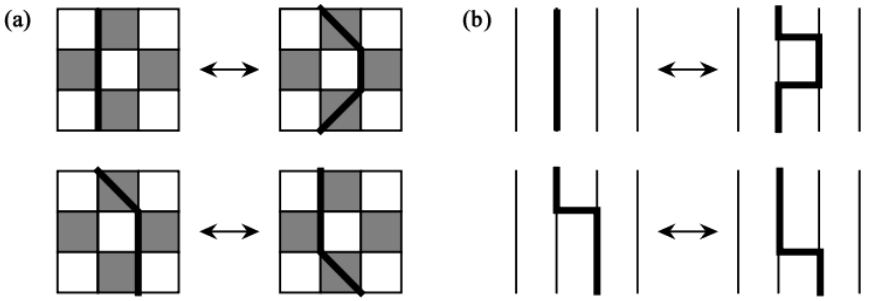

Figure 5. Local update of two worldlines (a) discrete imaginary time (b) continuous imaginary time

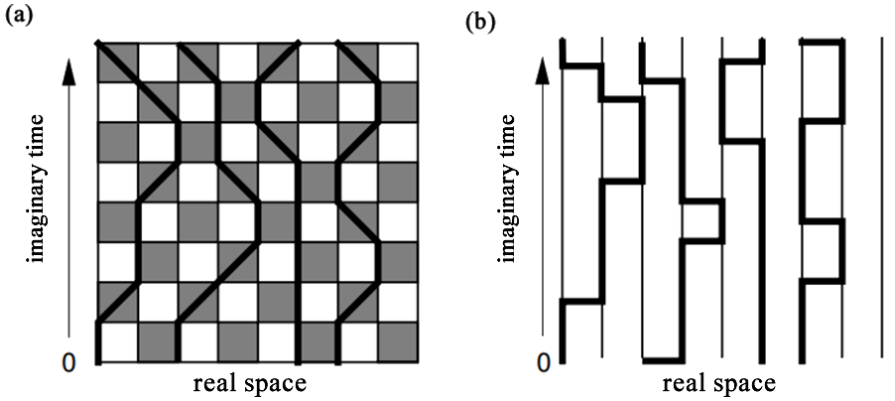

Figure 6. Worldlines (a) discrete imaginary time representation (b) continuous imaginary time representation

A cluster update in continuous imaginary time with the loop algorithm is exemplified in Figure 7.

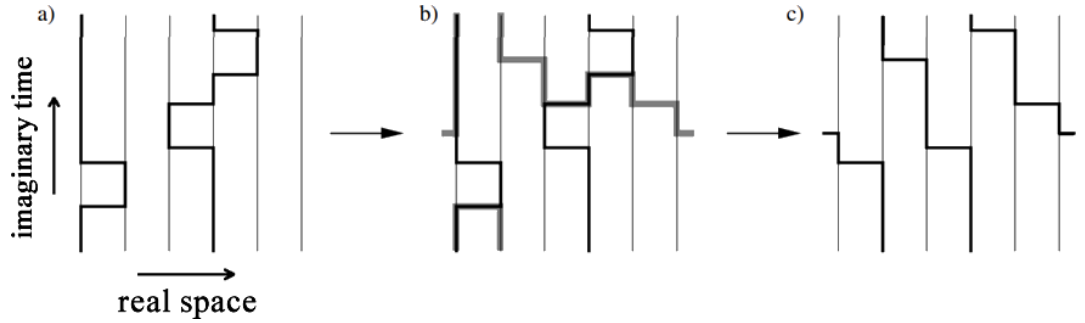

Figure 7. An update scheme of the loop algorithm

Figure 7(a) is the worldlines configuration before an update (thick black lines indicate upward spins, thin gray lines indicate downward spins). In Figure 7(b), there is a cluster update shown with thick gray lines with worldlines configuration. Figure 7(c) shows the world lines configuration after the directions of all spins in the cluster are changed.

2.2 Expected Value & Thermodynamic Quantities

In the lattice model, the partition function and the expected value of an observable are given by Equation 20 and Equation 21 where $\beta = \frac{1}{k_B T}$, T is temperature, and kB is the Boltzmann constant.

$$Z = Tr[e^{-\beta \hat{H}}] \tag{20}$$

$$\langle A \rangle = \frac{Tr[Ae^{-\beta \hat{H}}]}{Tr[e^{-\beta \hat{H}}]} \tag{21}$$

The tough part is to deal with the Hamiltonian of the system in the statistical mechanics of many-particle quantum systems since the observables are in the form of large matrices. It is crucial to represent ⟨A⟩, by vertex weights, W(S), and the A(S) estimators belong to observables to apply the MCMC technique and calculate the expected values,

$$\langle A \rangle = \frac{\sum_S A(S)W(S)}{\sum_S W(S)} \tag{22}$$

In the loop algorithm, the graph configuration G contains a wealth of information about the physical properties of the system. Estimators developed in conjunction with the loop algorithm are used to reduce measurement errors [15, 57]. The expected value of an observable A over G graph, A(G),

$$A(G) = \frac{\sum_S A(S)\Delta(S,G)}{\sum_S \Delta(S,G)} \tag{23}$$

A(G) is the average of A(S) over $2^{N_S(G)}$ number of the worldlines configurations. $N_S(G)$ represents the number of clusters.

$$\langle A(G)\rangle_G = \frac{1}{Z}\sum_G A(G)W(G) = \frac{1}{Z}\sum_G \left[\frac{\sum_S A(S)\Delta(S,G)}{\sum_S \Delta(S,G)}\right][\sum_S \Delta(S,G)V(G)]$$

$$\langle A(G)\rangle_G = \frac{1}{Z}\sum_S A(S)[\sum_G \Delta(S,G)V(G)] = \langle A(S)\rangle_S \quad (24)$$

The calculation of A(G) calculation is not cost-effective. It can be done more with the help of the symmetries found in an original physical system using improved evaluators. In addition, improved evaluators for correlation functions can be built and the calculation of correlation functions can be facilitated. The significant thermodynamic quantities that are calculated via the improved estimators in this study are given by Equation 25 and Equation 26, respectively. The thermal agitations are included in the atomic scale.

$$M_\alpha = \sum_i S_i^\alpha \qquad (\alpha = x, y, z) \quad \text{(magnetization)} \tag{25}$$

$$E = -\frac{1}{Z}\frac{\partial Z}{\partial \beta} \qquad \text{(internal energy)} \tag{26}$$

2.3 *The Boundaries of the Localizable Entanglement*

The entanglement has been quantified via a variety of measurement approaches, including concurrence, entanglement entropy, entanglement witness, and negativity. Verstraete, F., established a close connection between correlation functions and entanglement by describing localized entanglement between two sub-parts. It is the maximum amount of entanglement that can be localized via making local measurements in the rest of the system using the upper and lower limits. Hence, this content focuses on determining the upper and lower limits of the entanglement of an N-qubit system. Nonetheless, a close relationship between entanglement phenomena and classical correlations has been established. The classical two-point correlation function (Equation 27) is associated with the upper limit [51].

$$Q_{\alpha\beta}^{ij}(|\psi\rangle\langle\psi|) = \langle\psi\left|\hat{\sigma}_\alpha^i \otimes \hat{\sigma}_\beta^j\right|\psi\rangle - \langle\psi|\hat{\sigma}_\alpha^i|\psi\rangle\langle\psi\left|\hat{\sigma}_\beta^j\right|\psi\rangle \tag{27}$$

By unrolling the equation $LE_{ij}(\psi) \geq \max | Q_{\alpha\beta}^{ij}(\psi) |$ for a given pure state $|\psi\rangle$ of N qubits, a relationship between concurrence and localizable entanglement in spin-1/2 systems may be applied to higher-dimensional spin systems. The left side of the Eq.28 is associated with the lower bound of entanglement (LE_{ij}^{lb}) while the right side represents the upper bound of the entanglement (LE_{ij}^{ub}). However, the use of entanglement of assistance (EoA) reveals the upper bound. Thus, the following equation provides an easy way to express the bounds of entanglement.

$$max\left(\left|Q_{xx}^{ij}\right|, \left|Q_{yy}^{ij}\right|, \left|Q_{zz}^{ij}\right|\right) \leq LE_{i,j} \leq \frac{\sqrt{X_+^{ij}}+\sqrt{X_-^{ij}}}{2} \tag{28}$$

$$x_\pm^{ij} = \left(1 \pm \langle\sigma_z^i\sigma_z^j\rangle\right)^2 - \left(\langle\sigma_z^i\rangle \pm \langle\sigma_z^j\rangle\right)^2 \tag{29}$$

A strong methodology based on spin clustering on discrete imaginary time is introduced by loop algorithms as a significant means of simulating quantum spin systems. The Markov process exhibits a continuous loop of the transition from the spin (S) to graph (G) configurations, in contrast to the conventional Markov Chain Monte Carlo (MCMC). The simulation process has been carried out after introducing a spin-1/2 lattice with exchange coupling interactions and the model's Heisenberg Hamiltonian. Long equilibration times can be shortened by gradually lowering the temperature during thermalization. The thermalization cost is 103 of the Monte Carlo steps before the physical quantity measurement method. Here, we concentrated on the internal energy as a function of temperature

through the MC updates. Simulated data is used to calculate the $Q^{ij}_{\alpha\beta}$ and $x^{ij}_{\pm}$. N=40 quantum spin-1/2 particles are considered as a chain. The thermodynamic properties and the boundaries of entanglement are determined by Loop algorithm-based Quantum Monte Carlo simulation by ALPS package [48] in parallel. The temperature interval has been set to Tϵ(0,4]. The dipole-dipole interaction strength (Dϵ(0,4]) and the external magnetic field ($B_z\epsilon$(0,5]) are taken into account to emphasize the effect of these interactions to the boundaries of entanglement. Note that, exchange coupling constants are set to Jz=1, Jx=Jy=-1.

3. FINDINGS & DISCUSSION

A clear illustration of the spin chain and exchange coupling of a mixed magnetic state is given in Figure 8. FM and AFM states are indicated by Jz, Jx, and Jy couplings in a XXZ mixed state. Jx and Jy specify an AFM interaction while Jz indicates a FM interaction in a spin-1/2 chain. We have previously worked on isotropic AFM [47] and FM models [67] considering the dipole-dipole interaction, and thermal agitations.

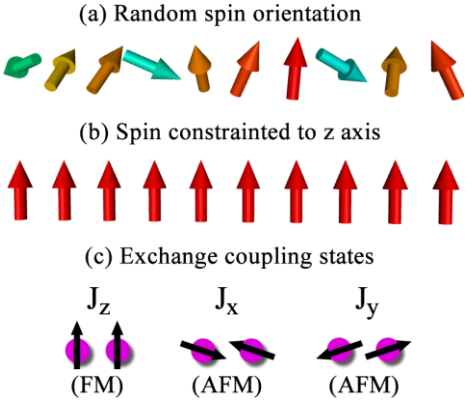

Figure 8. Illustration of spin chain with (a) random spin orientation (b) spin constrained to z-axis (c) exchange coupling constants.

The average magnetization and internal energy per spin as a function of temperature are shown in Figure 9. Firstly, the dipole-dipole interaction is neglected. The spin chain shows ferromagnetic behavior. It is probably originated from ferromagnetic exchange interaction in the -z projection even though antiferromagnetic coupling lies for neighboring spins along the x and y-axis. A stronger external field leads to a higher phase transition temperature (Figure 9(a)). Even the phase seems to be transited, the average magnetization does not vanish. The highest field dominates the thermal agitations, ensuring the spin pairs are constrained along the magnetic field direction. The increasing magnetic field reduces the internal energy (Figure 9(b)). Moreover, increasing temperature causes an increment in internal energy. Under zero fields and lower magnetic fields, the energy gets closer to zero but does not converge, and tends to be zero for infinite temperature.

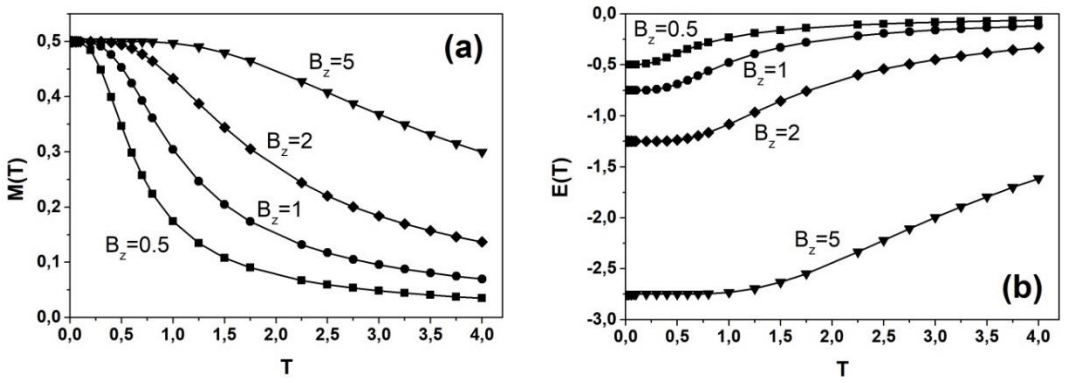

Figure 9. (a) Magnetization per spin (b) internal energy, as a function of temperature under external magnetic field, B_z=0.5, 1, 2, 5.

In the absence of dipole-dipole interaction (D=0), the lower and upper limits of entanglement as a function of temperature under an external magnetic field are clearly shown in Figure 10. The lower limit of entanglement (Figure 10(a)) is inversely proportional to the temperature. The external field contributes to lower limit values of LE. It is more than 3 times the lower limit of B_z=0 at nearly zero temperature. The maximum value of lower limit LE is calculated as 0.25. The strongest field preserves it up to T=1 and inhibits the lower limit from vanishing. There is an analogy between magnetization and lower limit (Figure 10(b)). The upper limit of LE is almost 1 (unity) at every temperature regime in the absence of an external field. Increasing the magnetic field estranges the upper limit from the saturation area. At low temperatures and strong fields, the value of this limit is around 0.75. Consequently, the external field acts directly to the bounds.

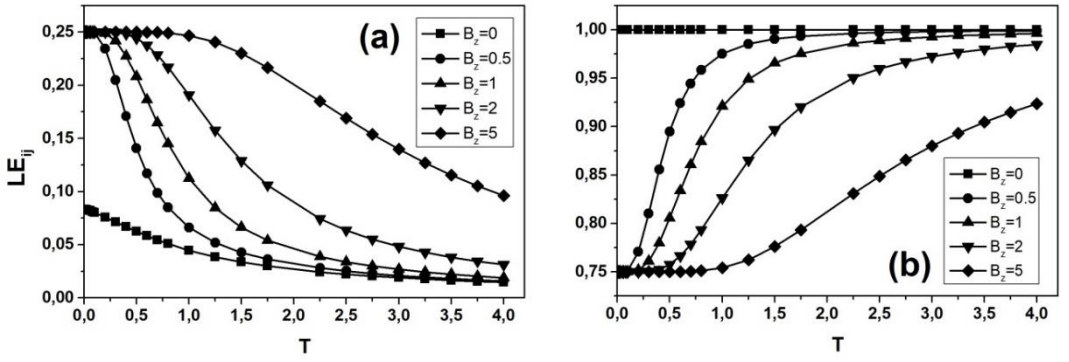

Figure 10. (a) LE lower limit (b) LE upper limit as a function of temperature under external magnetic field, B_z=0.5, 1, 2, 5.

In the absence of external field, lower bound values are decreasing by the increasing dipolar strength for D=0 and D=1 at low temperatures (Figure 11). For D≥1, increasing D hoist the lower limit. The temperature-dependent behavior is monotonic decreasing. We take a sensitive focus on the effect of dipolar strength in the range of D∈(0,1). The lower bound values show a decreasing-increasing behavior, briefly fluctuating, for consecutive temperature values. This can be sort of an awakening phenomenon. Each D creates an individual turning point. The strength of D is a natural tuner of these points as well (Figure 11(b)).

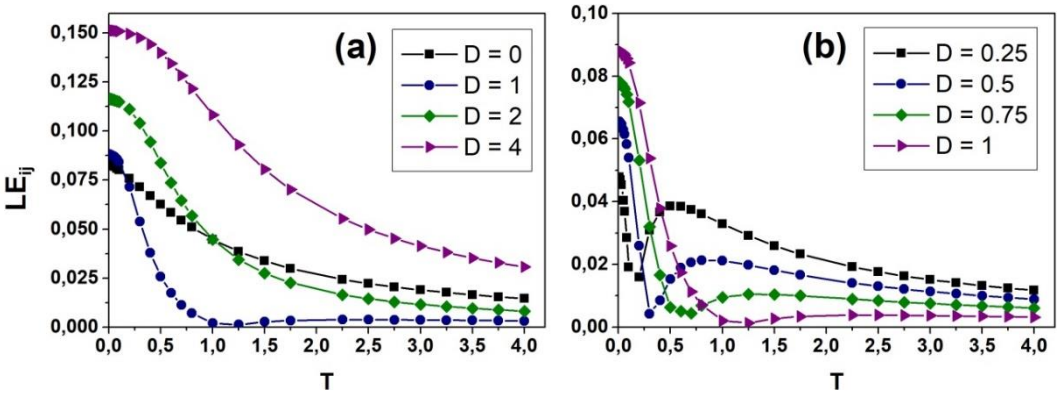

Figure 11. LE lower limit as a function of temperature under zero magnetic field with exchange coupling constants J_x=-1, J_y=-1, J_z=1 for (a) D=0, 1, 2, 4 (b) D= 0.25, 0.5, 0.75, 1.

When B_z=0.5, the lower limit values decrease as D increases in the range 1>D>0. The lowest D value (D=0.25) entails the highest lower limit values at low temperatures. For D>1, it is seen that as D increases, the values of the lower limit increase. D=2 and D=4 are not as entangled at very low temperatures as they are at D=0.25 and D=0.5. However, D=4 resists the distorting effect of temperature and keeps the amount of entanglement farther from zero (see Figure 12).

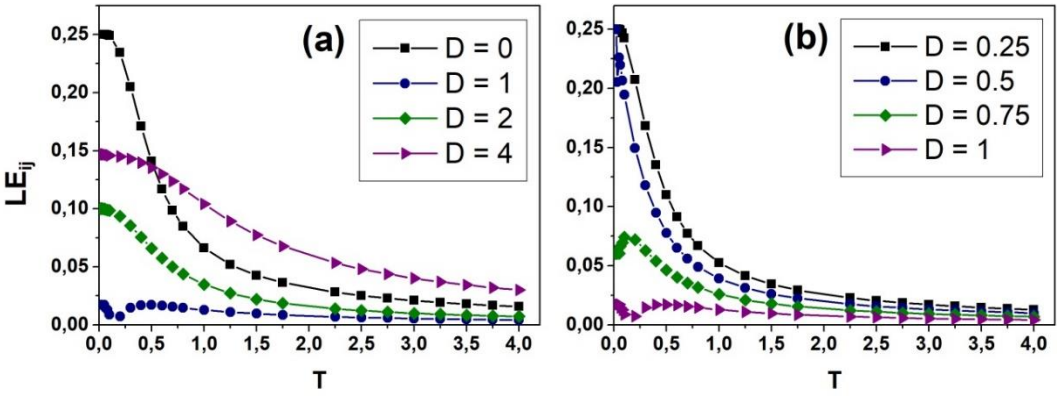

Figure 12. LE lower limit as a function of temperature under B_z=0.5 magnetic field with exchange coupling constants J_x=-1, J_y=-1, J_z=1 for (a) D=0, 1, 2, 4 (b) D= 0.25, 0.5, 0.75, 1.

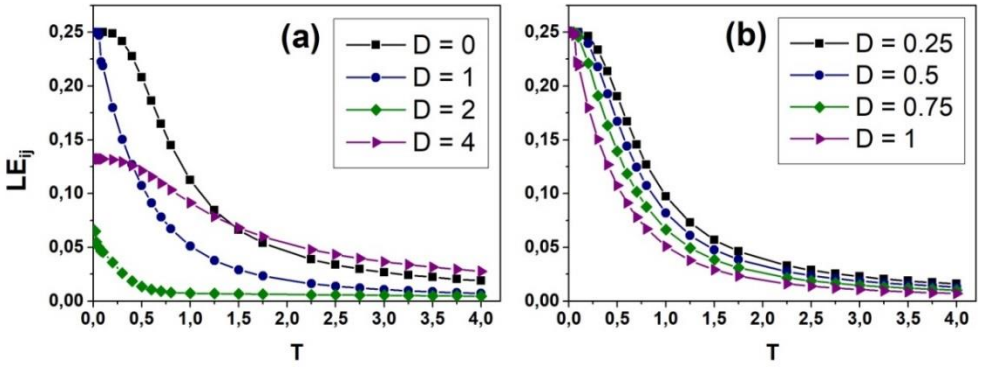

Figure 13. LE lower limit as a function of temperature under B_z=1 magnetic field with exchange coupling constants J_x=-1, J_y=-1, J_z=1 for (a) D=0, 1, 2, 4 (b) D= 0.25, 0.5, 0.75, 1.

The behavior changes as the external field increases. The reason is the dominancy of the external field to the dipolar effect and thermal. The lower limit decreases monotonically (Figure 14 and Figure 15) inverse proportional to the D.

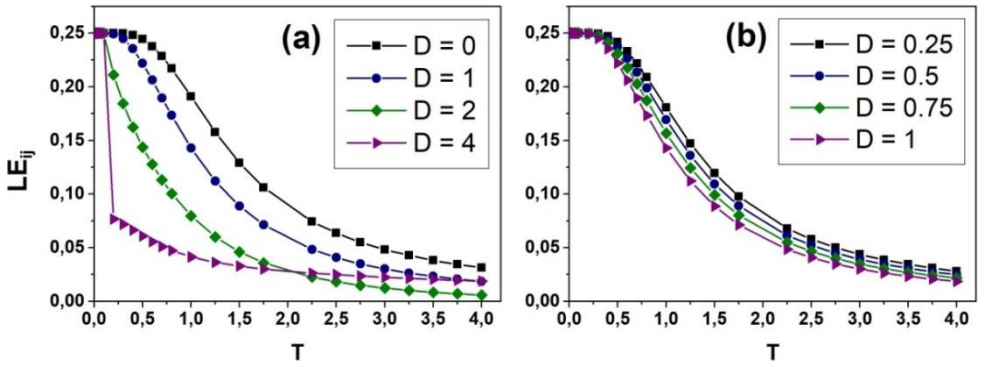

Figure 14. LE lower limit as a function of temperature under B_z=2 magnetic field with exchange coupling constants J_x=-1, J_y=-1, J_z=1 for (a) D=0, 1, 2, 4 (b) D= 0.25, 0.5, 0.75, 1.

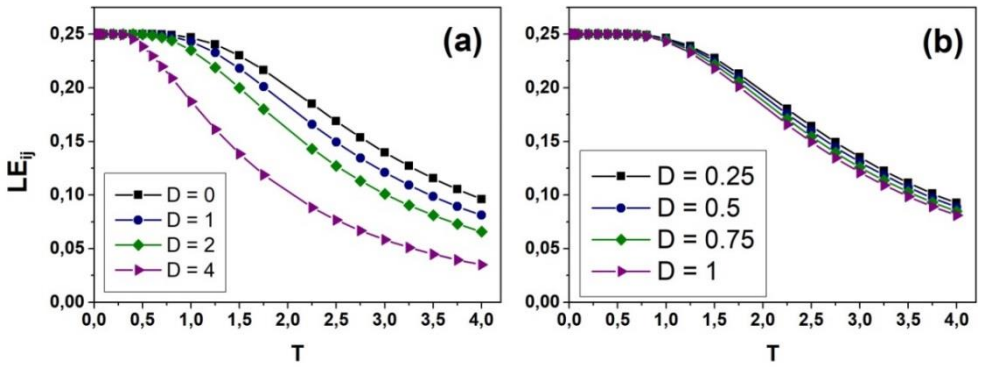

Figure 15. LE lower limit as a function of temperature under B_z=5 magnetic field with exchange coupling constants J_x=-1, J_y=-1, J_z=1 for (a) D=0, 1, 2, 4 (b) D= 0.25, 0.5, 0.75, 1.

The upper limit has its maximum value for all D values in the absence of an external field (Figure 17). As the external field increases, the upper limit decreases for lower temperatures as D decreases for T≥1.5; besides, they all overlap at the maximum value. Although this behavior does not change for 5>Bz≥0, the value of the T temperature at which all D curves begin to overlap increases. When B_z=5, the upper limit values corresponding to all D values decrease and reach their maximum with temperature and do not overlap.

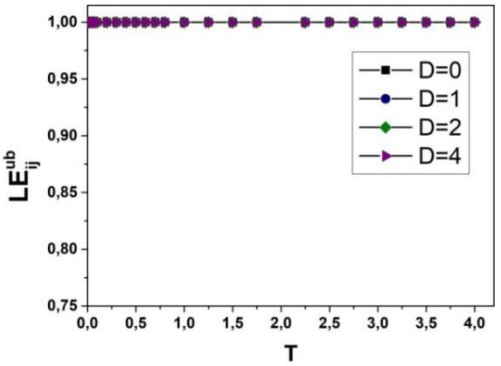

Figure 17. The upper limit of localizable entanglement under zero magnetic field for exchange coupling constants J_x=-1, J_y=-1, J_z=1 and dipolar interaction with D=0, 1, 2, 4.

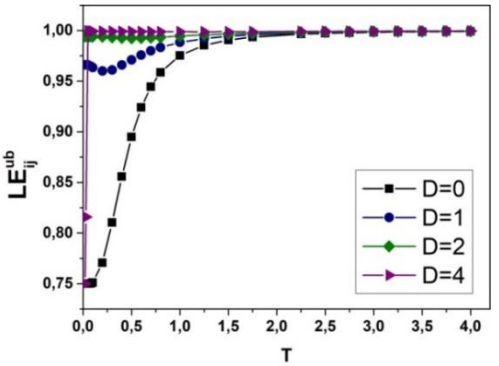

Figure 18. The upper limit of localizable entanglement under B_z=0.5 magnetic field for exchange coupling constants J_x=-1, J_y=-1, J_z=1 and dipolar interaction with D=0, 1, 2, 4.

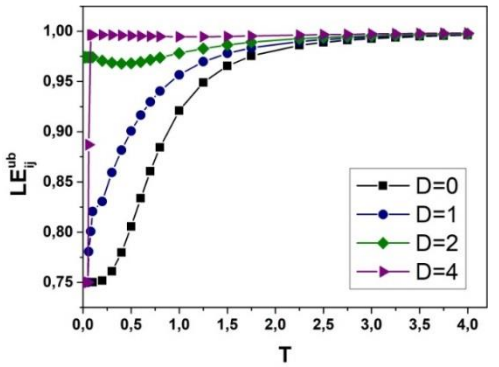

Figure 19. The upper limit of localizable entanglement under B_z=1 magnetic field for exchange coupling constants J_x=-1, J_y=-1, J_z=1 and dipolar interaction with D=0, 1, 2, 4.

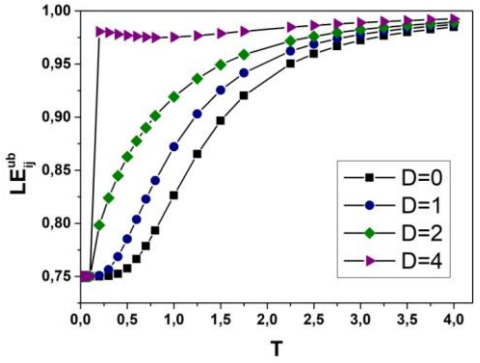

Figure 20. The upper limit of localizable entanglement under B_z=2 magnetic field for exchange coupling constants J_x=-1, J_y=-1, J_z=1 and dipolar interaction with D=0, 1, 2, 4.

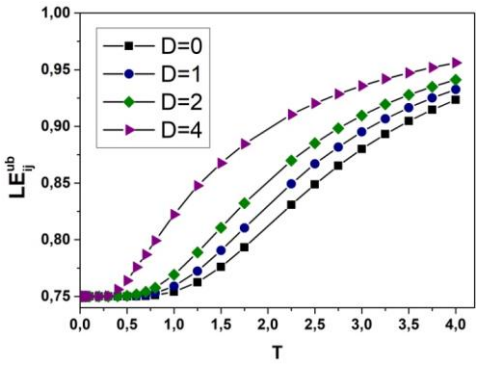

Figure 21. The upper limit of localizable entanglement under B_z=5 magnetic field for exchange coupling constants J_x=-1, J_y=-1, J_z=1 and dipolar interaction with D=0, 1, 2, 4.

Localizable entanglement between nearest neighboring spins is determined through lower and upper bounds for mixed magnetic states. The distance-dependent entanglement is discussed including the temperature and external field. In the absence of field (B_z = 0), LE of neighboring 20 spins is gradually measured (Figure 22). D = 4 dominates the thermal effects maximizing the lower bounds except T = 3.5. At very high temperatures (T = 3.5), this behavior does not change but is not at its maximum value. Accordingly, it can be said that as the temperature increases, the lower limit does not change according to the distance for D=4. The situation is slightly different for other dipole constants. In the absence of dipole-dipole interaction at T = 0.1, the lower limit of the entanglement is not damped until n = 10 adjacent spins. At T = 0.5 temperature, the distortion effect of temperature reduced the number of spins of the nearest n = 10 neighbors entangled for D = 0. At T ≥ 1 temperature, the lower limit is damped for all D values starting from the 2nd adjacent spin. When D < 4, the distorting effect of temperature dominates the dipole-dipole interaction.

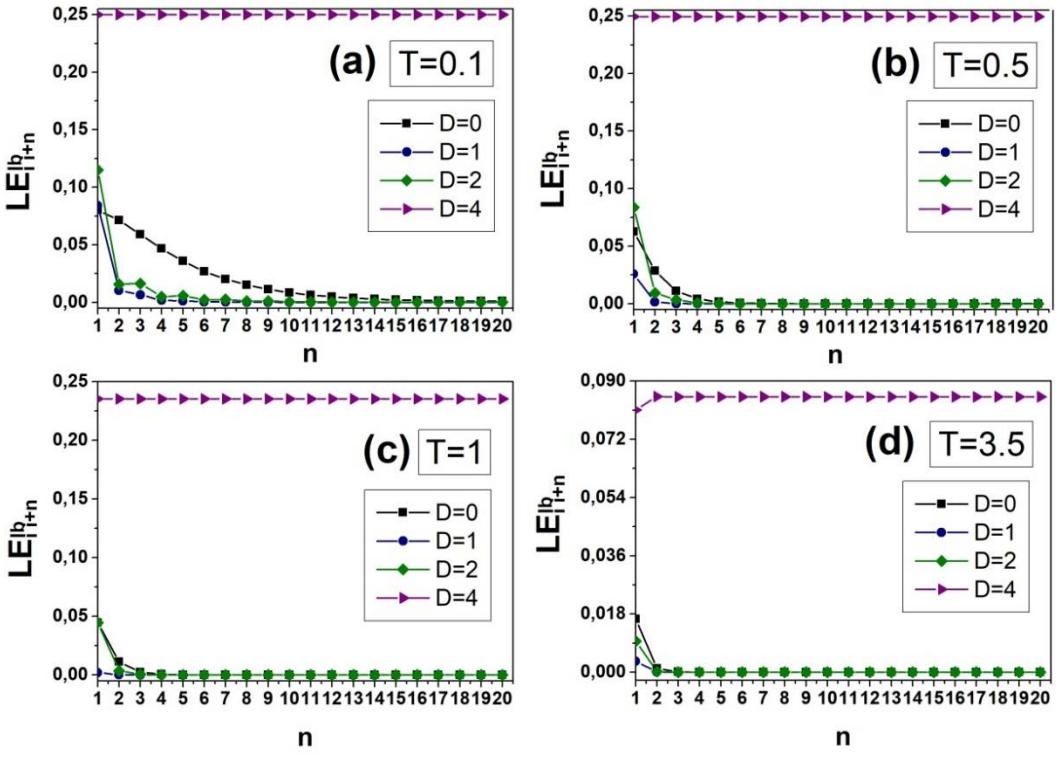

Figure 22. The lower limit of LE under zero magnetic field for 20 nearest neighboring at temperatures (a) T=0.1 (b) T=0.5 (c) T=1 (d) T=3.5

According to Figure 22(c) ($D = 2$), there is non-monotonic LE_{ij}^{lb} values underlying "rival regions" at low temperatures and under low magnetic fields.

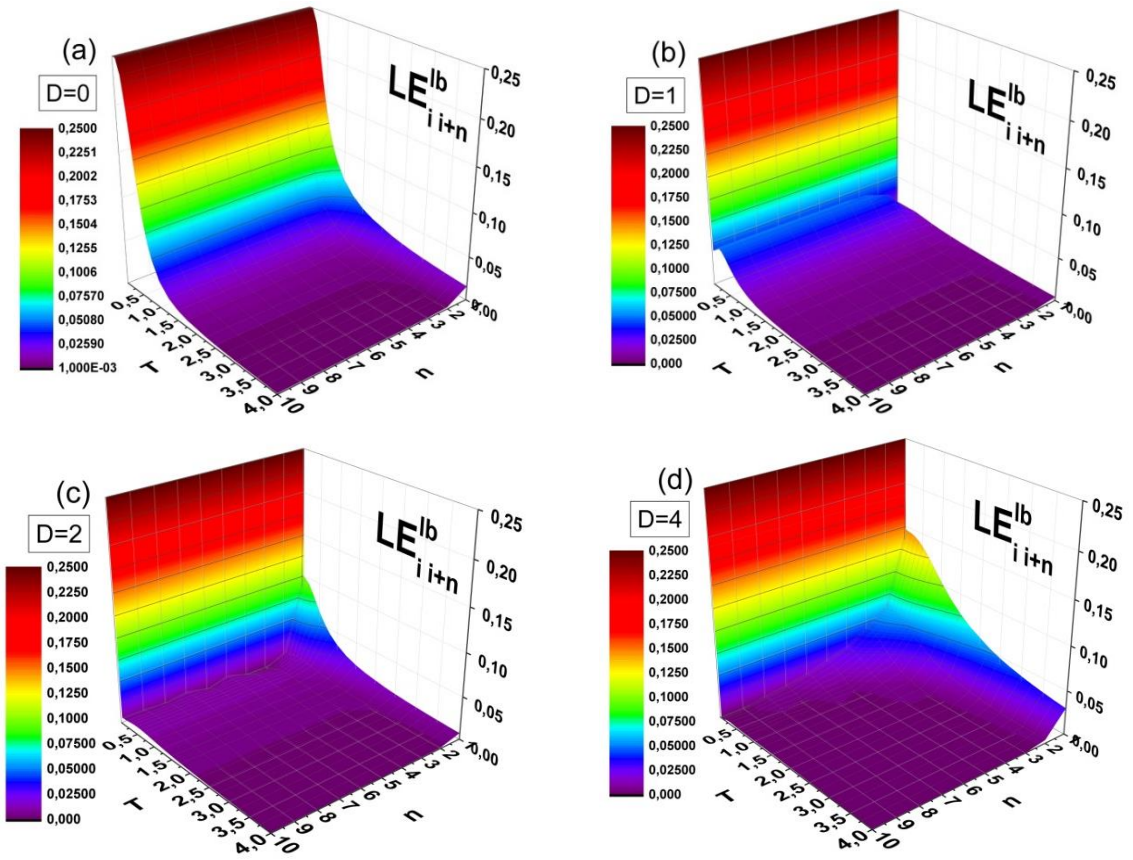

Figure 23. The illustration of the lower limit of LE under B_z=0.5 magnetic field for 10 nearest neighboring spins.

The variation of the lower limit of entanglement with temperature according to the nth neighboring spins under the external magnetic field B_z = 0.5 is given in Figure 23 for D = 0, 1, 2, and 4, respectively. At B_z = 0.5, for D = 0, the behavior of the first 10 neighboring spins with temperature is monotonous but does not change according to the length at low temperatures. At D = 1, the lower limit for all neighboring spins suddenly fell at low temperatures and, immediately after, increased until T = 0.5. At these low temperatures, the first and second neighboring spins, n=1 and n=2, have subdued lower bound values than the rest. D = 4 is the strength where the lower limit is maximized at both high and low temperatures. Except for D = 4 and B_z = 2, all other D strengths do not affect the system. D=4 causes a weak odd-even effect for n = 4. However, as D increases, the lower limit values decrease related to temperature and n. The change of the lower limit of entanglement with temperature according to the number of nth neighbors under the external magnetic field B_z = 2 is given in Figure 24 for D = 0, 1, 2, and 4, respectively. In the absence of a dipolar interaction, an external field merely takes place and influences the bounds of entanglement. As shown in Figure 24(a), there is a monotonic behavior in which LE decreases by increasing temperature for all nth neighboring spins except the nearest one. This discrepancy is abolished through the existence of dipolar interaction. According to Figure 24(d) ($D = 4$), there is non-monotonic LE_{ij}^{lb} values pointing to "revival regions" at low temperatures under low magnetic fields. Note that n=3 (3rd neighboring spins) is a clear fluctuation point that the value of the lower limit abruptly changes.

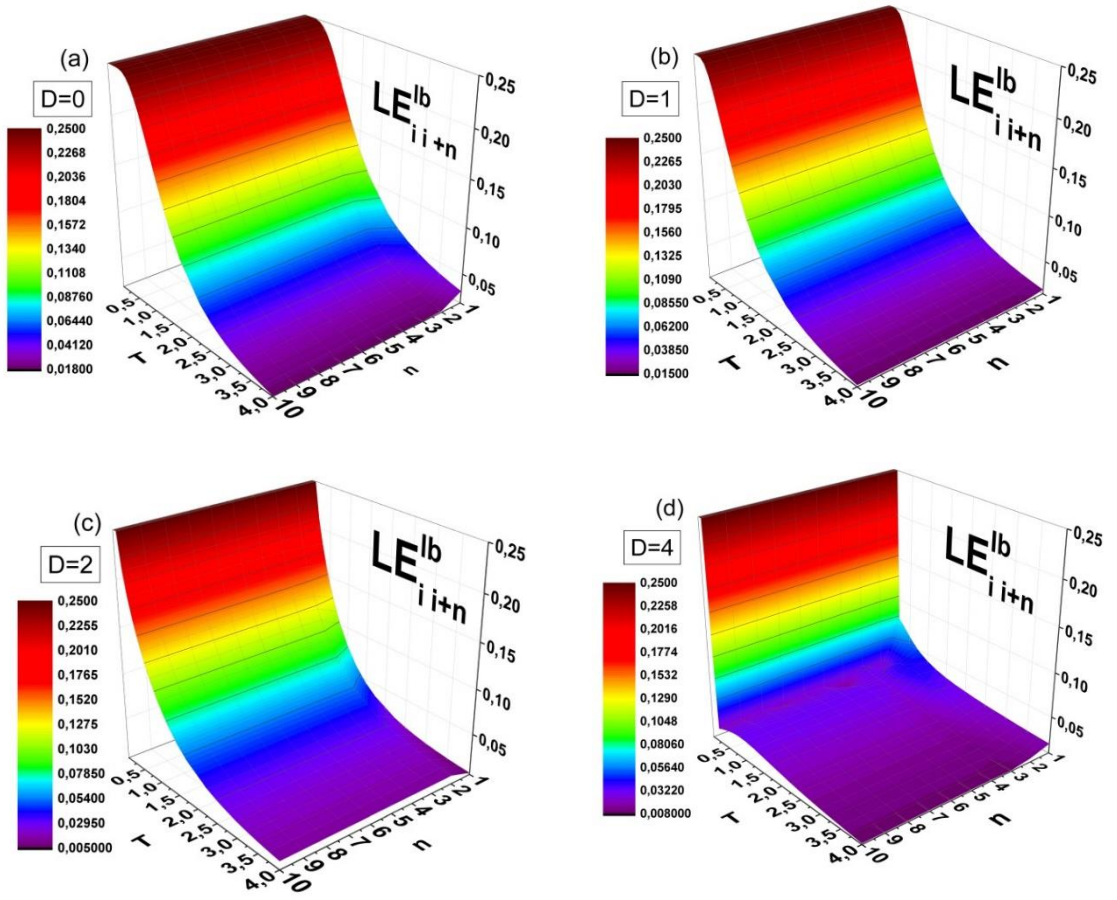

Figure 24. The illustration of the lower limit of LE under B_z=2 magnetic field for 10 nearest neighboring spins.

4. CONCLUSION

The upper and lower bounds of LE are quantified to measure entanglement between any two parts of the multipartite XXZ spin chain. In the T→0 case, the lower bound possesses a monotonically increasing trend proportional to the applied field when dipole-dipole interaction is disregarded. This behavior works for increasing temperature. As expected, thermal agitations distort the lower bound, and non-monotonic behavior takes place at relatively low temperatures. In the absence of dipole-dipole interaction at T = 0.1, the lower limit of the entanglement is not damped until n = 10 adjacent spins. At T = 0.5, the distortion effect of temperature reduced the number of spins of the nearest n = 10 neighbors entangled for D = 0. There is a monotonic behavior in which LE decreases by increasing temperature for all nth neighboring spins except the nearest one under when D = 0 under B_z = 0.5 magnetic field while a non-monotonic attitude points to rival regions at low temperatures.

Acknowledgments

This research was supported by the Scientific Research Projects Commission of Marmara University (FEN-C-DRP-120613-0273). Simulations were performed in the Simulation and Modeling Research Laboratory (Simulab) at the Department of Physics, Marmara University.

Funding

The authors should declare the financial interests which may be considered as potential competing interests.

Declaration of Competing Interest

Competing interest statement declared by authors. This statement must also appear in your manuscript before the references.

References

[1] Modławska, J., & Grudka, A., (2008). Nonmaximally Entangled States Can Be Better for Multiple Linear Optical Teleportation. *Physical Review Letters, 100, 110503.*

[2] Cavalcanti, D., Skrzypczyk, P., & Šupić, I., (2017).All Entangled States can Demonstrate Nonclassical Teleportation. *Physical Review Letters, 119, 110501.*

[3] Z.A.Sabegh, R., & Mahmoudi, M., (2018). Spatially dependent atom-photon entanglement. *Scientific Reports, 8, 13840.*

[4] Loss, D., & DiVincenzo, D., (1998). Quantum computation with quantum dots. *Physical Review A, 57, 120.*

[5] Jürgen Audretsch (2007), The Quantum Computer. In Entangled Systems: New Directions in Quantum Physics *(pp.219-245), Weinheim, Germany: John Wiley and Sons, Ltd.*

[6] Belsley, M. (2014). Introduction to Quantum Information Science, by Vlatko Vedral. *Contemporary Physics, 55, 124.*

[7] DiVincenzo, D. (1997). Quantum computation and spin physics (invited). *Journal of Applied Physics, 81, 4602-4607.*

[8] Zheng, S., & Guo, G., (2000). Efficient Scheme for Two-Atom Entanglement and Quantum Information Processing in Cavity QED. *Physical Review Letters, 85, 2392-2395.*

[9] Bennett, C., & DiVincenzo, D., (2000). Quantum information and computation. *Nature, 404, 1476-4687.*

[10] Eggert, S., Affleck, I., & Takahashi, M., (1994). Susceptibility of the spin 1/2 Heisenberg antiferromagnetic chain. *Physical Review Letters, 73, 332-335.*

[11] Hammar, P., Stone, M., Reich, D., Broholm, C., Gibson, P., Turnbull, M., Landee, C., & Oshikawa, M., (1999). Characterization of a quasi-one-dimensional spin-1/2 magnet which is gapless and paramagnetic for $g\,\mu\,B\,H \lesssim J$ and $k_B T \ll J$. *Physical Review B, 59, 1008-1015.*

[12] Androvitsaneas, P., Fytas, N., Paspalakis, E., & Terzis, A.F., (2012). Quantum Monte Carlo simulations revisited: The case of anisotropic Heisenberg chains. *Philosophical Magazine, 92, 4649-4656.*

[13] Barma, M., & Shastry, B., (1978). Classical equivalents of one-dimensional quantum-mechanical systems. *Physical Review B, 18, 3351-3359.*

[14] Handscomb, D. (1964). A Monte Carlo method applied to the Heisenberg ferromagnet. *Mathematical Proceedings of the Cambridge Philosophical Society, 60, 115-122.*

[15] Harada, K., & Kawashima, N., (2001). Loop Algorithm for Heisenberg Models with Biquadratic Interaction and Phase Transitions in Two Dimensions. *Journal of the Physical Society of Japan, 70, 13-16.*

[16] Huang, Y., & Su, G., (2017). Quantum Monte Carlo study of the spin-1/2 honeycomb Heisenberg model with mixed antiferromagnetic and ferromagnetic interactions in external magnetic fields. *Physical Review E, 95, 052147.*

[17] Sandvik, A., & Kurkijärvi, J., (1991). Quantum Monte Carlo simulation method for spin systems. *Physical Review B, 43, 5950-5961.*

[18] Deger, C., Aksu, P., & Yildiz, F., (2016). Effect of Interdot Distance on Magnetic Behavior of 2-D Ni Dot Arrays. *IEEE Transactions on Magnetics, 52, 1-4.*

[19] Duru, I., Değer, C., Kalaycı, T., & Arucu, M., (2015). A computational study on magnetic effects of $Zn_{1-x}Cr_xO$ type diluted magnetic semiconductor. *Journal of Magnetism and Magnetic Materials, 396 pp. 268-274.*

[20] Arnesen, M., Bose, S., & Vedral, V., (2001). Natural Thermal and Magnetic Entanglement in the 1D Heisenberg Model. *Physical Review Letters, 87, 017901.*

[21] Marchukov, O.V., & Zinner, N., (2016). Quantum spin transistor with a Heisenberg spin chain. *Nature Communications, 7, 13070.*

[22] Renes, J., Miyake, A., Brennen, G., & Bartlett, S., (2013). Holonomic quantum computing in symmetry-protected ground states of spin chains. *New Journal of Physics, 15, 025020.*

[23] Apollaro, T., Lorenzo, S., Sindona, A., Paganelli, S., Giorgi, G., & Plastina, F., (2015). Many-qubit quantum state transfer via spin chains. *Physica Scripta, T165 pp. 014036.*

[24] Wang, X., (2002). Threshold temperature for pairwise and many-particle thermal entanglement in the isotropic Heisenberg model. *Physical Review A, 66, 044305.*

[25] Wang, X., (2001). Entanglement in the quantum Heisenberg XY model. *Physical Review A, 64, 012313.*

[26] Rigolin, G., (2004). Thermal entanglement in the two-qubit Heisenberg XYZ model. *International Journal of Quantum Information, 2, 393-405.*

[27] Androvitsaneas, P., Paspalakis, E., & Terzis, A., (2012). A quantum Monte Carlo study of the localizable entanglement in anisotropic ferromagnetic Heisenberg chains. *Annals of Physics, 327, 212-223.*

[28] Sinyagin, A., Belov, A., Tang, Z., & Kotov, N., (2006). Monte Carlo Computer Simulation of Chain Formation from Nanoparticles. *Journal of Physical Chemistry B, 110, 7500-7507.*

[29] Kim, I., (2013). Long-Range Entanglement is Necessary for a Topological Storage of Quantum Information. *Physical Review Letters, 111, 080503.*

[30] Elman, S., Bartlett, S., & Doherty, A., (2017). Long-range entanglement for spin qubits via quantum Hall edge modes. *Physical Review B, 96, 115407.*

[31] Bitko, D., Rosenbaum, T., & Aeppli, G., (1996). Quantum Critical Behavior for a Model Magnet. *Physical Review Letters, 77, 940-943.*

[32] Chakraborty, P., Henelius, P., Kjønsberg, H., Sandvik, A., & Girvin, S., (2004). Theory of the magnetic phase diagram of $LiHoF_4$. *Physical Review B, 70, 144411.*

[33] Bramwell, S., & Gingras, M., (2001). Spin Ice State in Frustrated Magnetic Pyrochlore Materials. *Science, 294, 1495-1501.*

[34] Castelnovo, C. R., & Sondhi, S., (2008). Magnetic Monopoles in Spin Ice. *Nature, 451, 42-45.*

[35] Mengotti, E., Heyderman, L., Bisig, A., Fraile Rodríguez, A., Le Guyader, L., Nolting, F., & Braun, H., (2009). Dipolar energy states in clusters of perpendicular magnetic nanoislands. *Journal of Applied Physics, 105, 113113.*

[36] Lahaye, T., Menotti, C., Santos, L., Lewenstein, M., & Pfau, T., (2009). The physics of dipolar bosonic quantum gases. *Reports on Progress in Physics. 72, 126401.*

[37] Peter, D., Müller, S., Wessel, S., & Büchler, H., (2012). Anomalous Behavior of Spin Systems with Dipolar Interactions. *Physical Review Letters, 109, 025303.*

[38] Islam, R., Senko, C., Campbell, W., Korenblit, S., Smith, J., Lee, A., Edwards, E., Wang, C., Freericks, J., & Monroe, C., (2013). Emergence and Frustration of Magnetism with Variable-Range Interactions in a Quantum Simulator. *Science, 340, 583-587.*

[39] Jurcevic, P., & Roos, C., (2014). Quasiparticle engineering and entanglement propagation in a quantum many-body system. *Nature, 511, 202-205.*

[40] Richerme, P., & Monroe, C., (2014). Non-local propagation of correlations in quantum systems with long-range interactions. *Nature, j511 pp. 198-201.*

[41] Mahmoudian S., Rademaker L., Ralko A., Fratini S., & Dobrosavljevic V., (2015). Glassy Dynamics in Geometrically Frustrated Coulomb Liquids without Disorder. *Physical Review Letters, 115, 025701.*

[42] Bohnet, J., Sawyer, B., Britton, J., Wall, M., Rey, A., Foss-Feig, M., & Bollinger, J., (2016). Quantum spin dynamics and entanglement generation with hundreds of trapped ions. *Science, 352, 1297-1301.*

[43] Sahling, S., & Lorenzo, E., (2015). Experimental realization of long-distance entanglement between spins in antiferromagnetic quantum spin chains. *Nature Physics, 15, 255-260.*

[44] Osborne, T., & Nielsen, M., (2002). Entanglement in a simple quantum phase transition. *Physical Review A, 66, 032110.*

[45] Vidal, G., Latorre, J., Rico, E., & Kitaev, A., (2003). Entanglement in Quantum Critical Phenomena. *Physical Review Letters, 90, 227902.*

[46] Bravo, B., Cabra, D., Gomez Albarracin, F., & Rossini, G., (2017). Long−range interactions in antiferromagnetic quantum spin chains. *Physical Review B, 96, 054441.*

[47] Duru, I.P., & Aktas, S., (2019). Localizable entanglement of isotropic antiferromagnetic spin-1/2 chain. *Turkish Journal of Physics. 43 pp. 272 - 279.*

[48] Bauer, B., Carr, L., Evertz, H., Feiguin, A., Freire, J., Fuchs, S., Gamper, L., Gukelberger, J., Gull, E., Guertler, S., Hehn, A., Igarashi, R., Isakov, S., Koop, D., Ma, P., Mates, P., Matsuo, H., Parcollet, O., Pawlowski, G., Picon, J., Pollet, L., Santos, E., Scarola, V., Schollwöck, U., Silva, C., Surer, B., Todo, S., Trebst, S., Troyer, M., Wall, M., Werner, P., & Wessel, S., (2011). The ALPS project release 2.0: open source software for strongly correlated systems. *Journal of Statistical Mechanics: Theory and Experiment, 2011, P05001.*

[49] DiVincenzo & Uhlmann, A., (1999). Entanglement of Assistance. *Quantum Computing and Quantum Communications, pp. 247-257.*

[50] Laustsen, T., Verstraete, F., & Van Enk, S., (2003). Local vs. Joint Measurements for the Entanglement of Assistance. *Quantum Information and Computation, 3, 64-83.*

[51] Popp, M., Verstraete, F., Martin-Delgado, M., & Cirac, J., (2005). Localizable entanglement. *Physical Review A, 71, 042306.*

[52] Todo, S., & Kato, K., (2001). Cluster Algorithms for General S Quantum Spin Systems. *Physical Review Letters, 87, 047203.*

[53] Vedral, V., & Plenio, M., (1998). Entanglement measures and purification procedures. *Physical Review A, 57, 1619-1633.*

[54] Qi, X., Gao, T., & Yan, F., (2017). Lower bounds of concurrence for N-qubit systems and the detection of k-nonseparability of multipartite quantum systems. *Quantum Information Process, 16, 23.*

[55] Xue-Na Zhu, M., & Fei, S., (2018). A lower bound of concurrence for multipartite quantum systems. *Quantum Information Processing, 17, 30.*

[56] Cornelio, M., (2013). Multipartite monogamy of the concurrence. *Physical Review A, 87, 032330.*

[57] Evertz, H. G., Lana, G., & Marcu, M. (1993). Cluster algorithm for vertex models. Physical Review Letters, 70(7), 875.

[58] Evertz, H. G., & Marcu, M. (1993). The loop-cluster algorithm for the case of the 6 vertex model. Nuclear Physics B-Proceedings Supplements, 30, 277–280.

[59] Kawashima, N., Gubernatis, J. E., & Evertz, H. G. (1994). Loop algorithms for quantum simulations of fermion models on lattices. Physical Review B, 50(1), 136.

[60] Sandvik, A. W. (1992). A generalization of Handscomb's quantum Monte Carlo scheme-application to the 1D Hubbard model. Journal of Physics A: Mathematical and General, 25(13), 3667.

[61] Sandvik, A. W. (1997). Finite-size scaling of the ground-state parameters of the two-dimensional Heisenberg model. Physical Review B, 56(18), 11678.
[62] Sandvik, A. W., & Kurkijärvi, J. (1991). Quantum Monte Carlo simulation method for spin systems. Physical Review B, 43(7), 5950.
[63] Scalettar, R. T. (1998). World-line quantum Monte Carlo. Quantum Monte Carlo Methods in Physics and Chemistry, 525, 65.
[64] Swendsen, R. H., & Wang, J.-S. (1987). Nonuniversal critical dynamics in Monte Carlo simulations. Physical Review Letters, 58(2), 86.
[65] Fortuin, C. M. (1969). Physica (Utrecht) 57, 536 (1972); PW Kasteleyn and CM Fortuin. J. Phys. Soc. Jpn. Suppl, 26(11).
[66] Fortuin, C. M., & Kasteleyn, P. W. (1972). On the random-cluster model: I. Introduction and relation to other models. Physica, 57(4), 536–564.
[67] Duru, İ.P., & Aktaş, Ş. (2022). Dipole-Dipole Effect to Limits of Entanglement in Multipartite Spin Chain: A Monte Carlo Study. International Journal of Advances in Engineering and Pure Sciences, 34(2), 305-316. https://doi.org/10.7240/jeps.1032914

September 2024, Vol:2, Issue:2

International Journal of New Findings in Engineering, Science and Technology

journal homepage: *https://ijonfest.gedik.edu.tr/*

Developing Soil Liquefaction Analysis Program created on Visual Basic Analysis in MS Excel based on the 2018 Turkish Seismic Code

Mahmut Özcan[a], Hasan Bozkurt Nazilli[b*], Mert Tolon[c]

[a] *Küçükçekmece Municipality, Turkey e-mail: ozcanmahmutt@gmail.com*
[b*]*Civil Engineering Department, Istanbul Gedik University, Turkey e-mail: bozkurt.nazilli@gedik.edu.tr Orcid ID: 0000-0003-3926-5025*
[c]*Civil Engineering Department, Maltepe University, Turkeye-mail: merttolon@maltepe.edu.tr Orcid ID: 0000-0002-0131-2976 (*Corresponding Author)*

Abstract

The rapid increase in the world's population, the desire to revise old structures or to need new structures, and the decrease in usable areas in some big cities lead engineers to examine ground conditions more frequently. Due to Turkey's location and geological structure, earthquake occurrences are quite high. The loss of life and property, which has increased with the earthquakes that have occurred in our country (Turkey) in recent years, has been examined and it has been seen that this situation is related to the ground factor rather than the superstructure design inadequacies. In this sense, the main goal of investors is to optimize the profit to be obtained by providing the aesthetics of the superstructure, comfort, and interior quality in building projects such as residences and offices. For this reason, geotechnical design is becoming a discipline that needs to be solved most economically. Starting the investment without paying due attention to the seismicity of the ground in the investment budgets, when the risk of liquefaction in the ground may come to the fore, it is possible to avoid unaccounted ground improvement methods, so new buildings with the risk of soil liquefaction are added to the unsafe old building stock. With the 2018 Seismic Code in Turkey, liquefaction on the ground and different problems that occur on the ground have been examined in more detail. Within the scope of this study, it was focused on getting faster results with faster and on-site determinations of the liquefaction situation on the ground, thanks to the Visual Basic application program prepared in Excel. In this sense, with the program prepared as the aim of the study, it is aimed to enable the construction of the soil liquefaction analysis to be made quickly and with less cost and to start the construction with a realistic budget and structural models. The program continuously increases its sensitivity and accuracy with additional inputs. This allows geotechnical engineers to achieve faster and earlier results.

Keywords:Earthquake; Soil Liquefaction; TBDY; 2018 Turkish Seismic Code Regulation.

1. INTRODUCTION

The energy that occurs as a result of sudden breaks in the earth's crust and spreads by seismic waves is called an earthquake. Earthquakes are disasters that negatively affect life in nature. It is possible to see the negative effects of the earthquake in all areas such as superstructure, infrastructure, and soil-bearing capacity losses [01]. Although it is in the same region, it can be thought that one of the reasons for the different damages in the structures is the failure

https://doi.org/10.61150/ijonfest.2024020207

to consider the structure-soil interaction. It has been observed that some of the damages observed in the structures after the earthquakes in our country are due to soil liquefaction.

During an earthquake, when the groundwater level is high, with the increase of pore water pressure of saturated non-cohesive soils under static and dynamic loads, the phenomenon called "liquefaction" occurs by acting like a liquid. At the end of the liquefaction event, there is a loss of strength in non-cohesive soils, and as a result, the soils lose their bearing capacity [2]. In particular, irreversible damages may occur in the superstructure as the ground loses its strength and becomes unable to carry the loads coming from the superstructure. The same negative effects can be seen in infrastructure systems.

With the prepared study, the liquefaction problem on the ground is detected early by using different regulations and methods, and more precise results are obtained by early intervention with a Visual Basic-based program, the data is obtained as a result of on-site investigations and laboratory tests are prepared on MS Excel. The results were obtained by using different methodologies to examine the differences in the liquefaction status of the ground and the shear wave velocity of the earthquake code prepared in the 2018 Turkey Building Seismic Code (TSC) used in our country and the earthquake regulation prepared in the TSC-2007. In this study, it is aimed to intervene in the problem on the ground early and reduce or completely eliminate the risk.

The frequent occurrence of earthquakes in Turkey, coupled with the high risk of soil liquefaction, has underscored the necessity for advanced geotechnical design. Despite the adoption of the 2018 Turkey Building Seismic Code (TSC), there is a pressing need for a cost-effective, efficient, and accurate method to assess soil liquefaction risk during the early stages of construction projects. Current practices often overlook the critical interaction between structure and soil, leading to significant damage during seismic events. As a research gap, this study aims to bridge this gap by developing a Visual Basic application within MS Excel that facilitates rapid and precise soil liquefaction analysis, thereby enabling geotechnical engineers to make informed decisions and implement timely soil improvement methods. However, the study does not compare this new method with other existing analysis techniques, which represents a limitation that future research should address.

2. METHODOLOGY

2.1 Regulations and Calculation Procedures

Turkey's current Seismic Code is the Building Earthquake Code 2018 published on 31.12.2018. It contains precise information about what should be considered for the superstructure or infrastructure to be built in a sequential and phased manner [3]. TSC-2018 provides much more comprehensive and clear information by creating a separate section on the liquefaction problem in the research.

2.2.1. *Liquefaction Analysis According to the 2018 Turkish Seismic Code*

Along with the regulation that considers every region as an earthquake zone, it is determined whether there is liquefaction in the ground as a result of a comprehensive ground examination with the analyzes obtained as a result of laboratory and experiments in the regions where soil groups belonging to the soil class “ZD, ZE, ZF” are located 20 m from the ground. should be done. Numerical liquefaction analysis is performed with the following steps.Moment magnitude (Mw) values of possible earthquakes produced by faults should be calculated.

$$Mw = a + b \log (SRL) \quad (1)$$

SRL: The length of the expected surface rupture (km), coefficients a and b: Depends on the type of fault.

The a and b coefficients in the equation giving the scenario earthquake magnitude with the fault segment approach is given in Table 1.

Table 1. The a and b coefficients in the equation giving the scenario earthquake magnitude with the fault segment approach [4].

Fault Type	a coefficient	b coefficient
Straight Slip Fault	5,16	1,12
Normal Fault	4,86	1,32
Reverse Fault	5.00	1,22
All Fault Types	5,08	1,16

SDS; the short period is the acceleration coefficient (dimensionless) and can be evaluated by;

$$SDS = SS \times FS \quad (2)$$

where; SS: Short period spectral acceleration value; FS: Local Ground Effect Coefficient for the short period region.

SDS is calculated from the Earthquake Hazard Map of Turkey according to the earthquake ground motion level, local soil class, latitude, and longitude and is taken from the website of AFAD Presidency (www.tdth.afad.gov.tr).

Vertical soil stress (σ_{vo}) is the vertical soil stress of the depth taken from SPT with a unit of kN/m².

$$\sigma_{vo} = \gamma \times h \quad (3)$$

γ : The natural unit weight of the soil (If the soil is saturated with water, the saturated unit weight, γ_d, is used). Its unit is kN/m^3, h : SPT depth (m).

Effective Vertical Stress (σ'_{vo}): It is the effective vertical soil stress at SPT depth. Its unit is kN/m^2.

$$\sigma'_{vo} = \sigma_{vo} - (\gamma_{water} \text{ x } h_{water}) \quad (4)$$

σ_{vo}:Vertical soil streess (kN/m^2), γ_{water}:Unit volume weight of water (kN/m3), h_{water}:Groundwater level height (m).

C_N: It is the geological stress (depth) correction coefficient applied in cohesionless soils. If the calculated C_N value is greater than 1.70, the maximum value of 1.70 should be taken.

$$C_N = 9.78\sqrt{(1/\sigma'_{vo})} \leq 1.70 \quad (5)$$

C_R: SPT is the rod length correction coefficient, C_S: SPT is the sampler type correction coefficient, C_B: SPT is the drill diameter correction coefficient, C_E: SPT is the energy ratio correction coefficient. SPT correction coefficients are given depending on the depth and the relevant coefficients are used in the calculations (TSC-2018).

Adjusted SPT Hit Count ($N_{1.60)}$: Corrected SPT beat count without units. $N_{1,60}$ is always used in liquefaction analysis. The N_{60} has no C_N correction.

$$N_{60} = N \text{ x } C_R \text{ x } C_S \text{ x } C_B \text{ x } C_E$$

$$N_{1,60} = N_{60} \times C_N \quad (6)$$

Here; N : SPT impact number obtained from the field, C_N : Cover load correction coefficient, C_R : Rod length correction coefficient, C_S: Sample receiver correction coefficient, C_B : Borehole diameter correction coefficient, C_E : Energy efficiency correction coefficient, and $N_{1,60}$: Adjusted SPT stroke count.

$N_{1,60f}$: The number of SPT hits corrected for the fines content is expressed using the α and β coefficients for the fines content.

$$N_{1,60f} = \alpha + \beta \, . \, N_{1,60} \quad (7)$$

$\alpha = 0$; $\beta = 1$ (IDI ≤ %5)
$\alpha = \exp[1.76-(190/IDI^2)]$; $\beta = 0.99 + IDI^{1,5}/1000$ (%5 < IDI < %35)
$\alpha = 5.0$; $\beta = 1.2$ (IDI≥%35)

CRRM7.5: It is the cyclic resistance ratio against an earthquake with a moment magnitude of 7.5.

$$CRRM7.5 = \frac{1}{34-N1,60f} + \frac{N1,60}{135} + \frac{50}{[10N1,60f+45]^2} - \frac{1}{200} \quad (8)$$

CM: It is the design earthquake moment magnitude correction coefficient.

$$CM = \frac{10^{2.24}}{Mw^{2.56}} \quad (9)$$

τR: It is liquefaction resistance. Its unit is kPa.

$$\tau R = CRRM7.5 \times CM \times \sigma'_{vo} \quad (10)$$

τdeprem: It is the average cyclic shear stress in the soil resulting from an earthquake. Its unit is kPa.

$$\tau_{deprem} = 0.65 \times \sigma_{vo} \times (0,4 \times SDS) \quad (11)$$

Safety Condition Against Liquefaction (τR / τdeprem):

$$FSL = \frac{\tau R}{\tau deprem} \geq 1,1 \quad (12)$$

If the FSL value is greater than 1.1, there is no risk of liquefaction, and if it is small, there is a risk of liquefaction in the soil.

2.2.2. *Liquefaction Calculation Steps According to Shear Wave Velocity*

Iterative or Shear Stress Ratio (KGO): It is expressed as the iterative stress ratio (KGO) of the soil material below the groundwater [5].

$$KGO = \frac{\tau ort}{\sigma vs'} = 0.65 \times \frac{\sigma vs \times amax \times rd}{\sigma vs' \times g} \quad (13)$$

Here;

τ_{ort}: It is the average value of the iterative shear stress caused by the earthquake and the coefficient of 0.65 is considered to be 65% of the maximum stress,

α_{max}: The largest (peak) acceleration,

g: gravitational acceleration,

σ_{vs}: The dynamic vertical stress at the investigated depth calculated from the shear wave velocity and the seismic wave period,

σ_{vs}': It is the effective dynamic vertical stress calculated with the same parameters and at the same depth.

Dynamic vertical stress and effective dynamic vertical stress are calculated in kPa units with the following mathematical expressions [5].

$$\sigma_{vs} = 2.45T\sum_{i=1}^{n} \Upsilon_i Vsi$$
$$\sigma_{vs}' = 2.45T\sum_{i=1}^{n} \Upsilon_i Vsi\text{-}9.81(z\text{-}z_w)(\Upsilon_{sa} - \Upsilon_i) \quad (14)$$

Here; Υ: unit volume weight (gr/cm3), Υ_h: unit volume weight saturated with water (gr/cm^3),

T: earthquake wave period (s), z: layer depth under investigation (m), and zw: groundwater depth (m).

Effective Stress Corrected Shear Wave Velocity Standard penetration test (SPT) can be corrected using the following equation with effective stress in Vs, similar to the equation known to correct the number of impacts with effective stress [6,7].

$$Vsc=Vs\left(\frac{Pa}{\sigma v'}\right)^{0.25} \quad (15)$$

Here; V_{sc} is the effective stress-corrected shear wave velocity and Pa is a reference stress known as atmospheric pressure.

Shear Resistance Ratio (KDO) For the corrected values of shear wave velocity (Vs) or SPT impact number obtained from field studies, the KDO value that separates liquefaction and non-liquefaction is called the shear resistance ratio. KDO is physically the natural resistance of the ground.

Andrus and Stokoe II (1997; 1999; 2000), and Uyanık (2002) proposes the following relationship between KDO and V_{sc} in their studies [8,9,10 and 11].

$$KDO=\left[a\left(\frac{VSc}{100}\right)^2+b\left(\frac{1}{VSmax-Vsc}-\frac{1}{VSmax}\right)\right]\times MSF \quad (16)$$

Here; V_{sc}: Corrected shear wave velocity, V_{smax}: Upper limit value of corrected shear wave velocity where liquefaction can occur, a and b: Curve-appropriate parameters and MSF: Magnitude scale factor.

$$MSF=\left(\frac{Mw}{7.5}\right)^n \quad (17)$$

Here; M_w is the moment magnitude and n is an exponential constant.

It varies between V_{smax}=220-250m/s depending on the fineness content of the ground. The relationship between V_{smax} and the fineness content (FC) of the soil is expressed below.

V_{smax}=250m/s	FC≤ %5 Sand
V_{smax}=250 – (FC-5)m/s	%5<FC<%35 Sand
V_{smax}=220m/s	FC≥%35 Sandand Silt

Factor of Safety (FS); The most common way of determining liquefaction hazard is the factor of safety.

$$FS=KDO/KGO \tag{18}$$

As a general rule, it indicates that liquefaction will occur when FS≤ 1.

2.2 Development of Soil Liquefaction Analysis with Visual Basic

The determination of the risk of liquefaction in soils takes place within a certain chain of rules, regardless of the regulation. Applying these rules again in each soil analysis takes time and invites mistakes to be made. For this reason, software has been developed in which all the rules are written and the data will be entered and the program will direct the program to the result, and thus calculations and analyzes are made possible both visually and without going beyond the rules, by entering the data.

The software developed in this study was developed with the VBA (Virtual Basic for Application) programming language working on Excel, which is frequently used by researchers in the field of engineering. There are 4 types of analysis possible in the developed software; 1. Liquefaction Risk Analysis According to TSC-2018 [12], 2. Liquefaction Risk Analysis According to TSC-2007, 3. Liquefaction Analysis According to Shear Wave Velocity, 4. Comparative Liquefaction Analysis Geotechnical Report.

The software is run by using the tables of the Excel application with the VBA programming language. For each new ground analysis, a new page is opened in the Excel application and named "Analysis_(AnalysisName)". All data related to the study are organized in tables on this page. For each soil analysis, it is possible to compare according to TSC-2018, according to TSC-2007, Shear Wave Velocity (an analysis method in accordance with TSC-2007 regulation), and a comparative module between them (Figure 1).

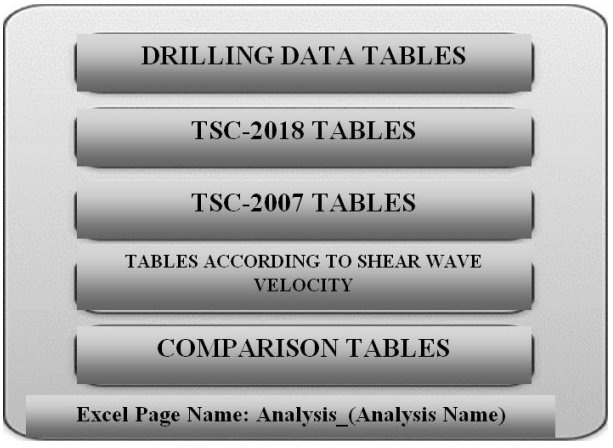

Figure 1. Arrangement of Analysis with Tables in the Developed Software.

Importing data belonging to other analyses recorded from the same Excel file, importing data belonging to other analyses recorded from another Excel file (produced with this program), and recording as a PDF file in a certain order according to the relevant analysis types are the features developed for this program. The operation of this program is done by creating tables, printing formulas, making controls, creating graphics, small code groups named module and interface forms named userform.

In addition, there is an Excel sheet called “data” to be used in all analyses and a list of analyses is kept. This page contains tables with a list of analyses, and options for soil types, DTS types, sampler types, borehole diameters, ram types.On the login screen of the software, what type of analysis should be done first is asked. This step is the first step of the software and starts with calling the userform named U1_GIRIS. For this, a shortcut (Ctrl+O) is defined so that the program can be started when Excel is first opened. As a first step, the login page is opened by using this shortcut (Figure 2). These 3 methods were preferred in order to compare the analyzes with the highest accuracy and the clearest results.

Figure 2. Start Page of Developed Software.

The flow chart of soil liquefaction analysis programmed with VBA language is given in Figure 3. In this context, liquefaction risk analysis according to TSC-2018 is selected on the login screen, respectively, and then "open analysis" should be selected in the analysis interface according to shear wave velocity or other methodologies.

Afterward, drilling data and soil parameters are entered into the relevant interface, in the meantime, SPT-N correction is made. In the next step, the liquefaction resistance is calculated and then the liquefaction risk safety factor is found and compared. Finally, the necessary information for the report is entered into the relevant interface and the analysis report is saved and retrieved.

3. RESULTS

The program prepared within the scope of the study takes the user step by step from the beginning to the end of the analysis. It is not possible to proceed to the next step without entering the desired data. It is not possible to

manually change the parameters (fixed coefficients, etc.) that should not be changed, so as a result of the analysis, the user cannot play with the results as he wishes. The reliability of the geotechnical evaluation is assured.

With the Import Data button, the user can directly transfer other analyzes in the program to the analysis to be created or export from another Excel. Likewise, with this button, it can mark the desired data and call only that data (SPT 15-30, Unit Volume Weight, etc.).

The program automatically provides access to the soil type according to the SPT-N60 value (Figure 4). The program automatically provides the α and ß values according to the fine grain content in the 2018 Earthquake Code (Figure 5). Based on the corrected SP-N value, the depth dependent ground plot is given in Figure 6.

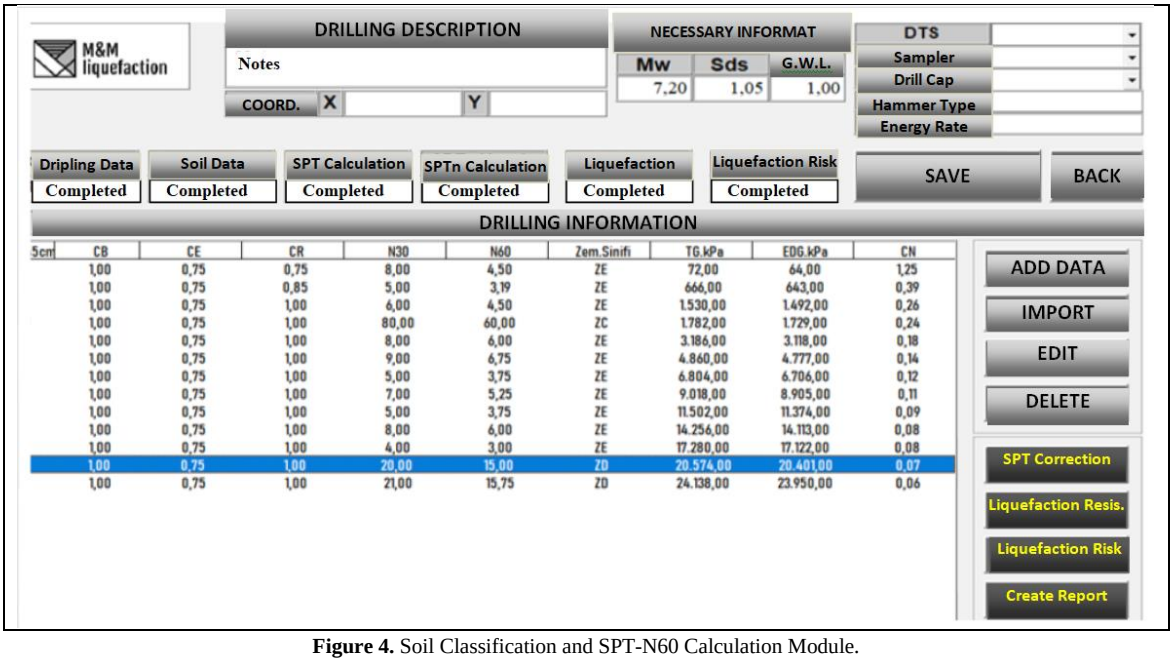

Figure 4. Soil Classification and SPT-N60 Calculation Module.

The program provides the user with results according to 3 different Liquefaction Analysis. For each analysis, the relationship between SPT-N and depth dependent graph can be observed separately and thus more precise engineering judgments can be made. Analyzes can be made by entering the data according to 2007 and 2018 and Shear Wave Velocity and the results can be obtained with the Comparative Liquefaction Analysis of Geotechnical Report button.

SPT N CORRECTION

Sample	Depth m	Soil Type	N1.60	TG.kPa	EDG.kPa	IDI	alfa	beta	N1.60F
1,00	1,80	Filling	7,65	30,60	22,60	90,00	5,00	1,20	14,18
2,00	3,30	Clay	3,89	90,00	67,00	90,00	5,00	1,20	9,67
3,00	4,80	Clay	3,83	176,40	138,40	99,00	5,00	1,20	9,59
4,00	6,30	Clay	3,41	289,80	236,80	99,00	5,00	1,20	9,09
5,00	7,80	Clay	3,15	430,20	362,20	56,00	5,00	1,20	8,78
6,00	9,30	Clay	2,98	597,60	514,60	57,00	5,00	1,20	8,57
7,00	10,80	Clay	1,42	792,00	694,00	57,00	5,00	1,20	6,71
8,00	12,30	Sand	1,75	1013,40	900,40	42,00	5,00	1,20	7,10
9,00	13,80	Sand	1,11	1261,80	1133,80	42,00	5,00	1,20	6,34
10,00	15,30	Sand	1,61	1537,20	1394,20	42,00	5,00	1,20	6,93
11,00	16,80	Sand	0,73	1839,60	1681,60	42,00	5,00	1,20	5,88
12,00	18,30	Sand	3,36	2169,00	1996,00	8,00	0,30	1,01	3,70
13,00	19,80	Sand	3,26	2525,40	2337,40	8,00	0,30	1,01	3,60
14,00	21,30	Clay	1,15	2908,80	2705,80	8,00	0,30	1,01	1,47
15,00	22,80	Clay	0,81	3319,20	3101,20	8,00	0,30	1,01	1,12
16,00	24,30	Clay	0,76	3756,60	3523,60	8,00	0,30	1,01	1,07

Figure 5. Module for Determination of α and ß values according to SPT-N Correction and Fine Grain Content.

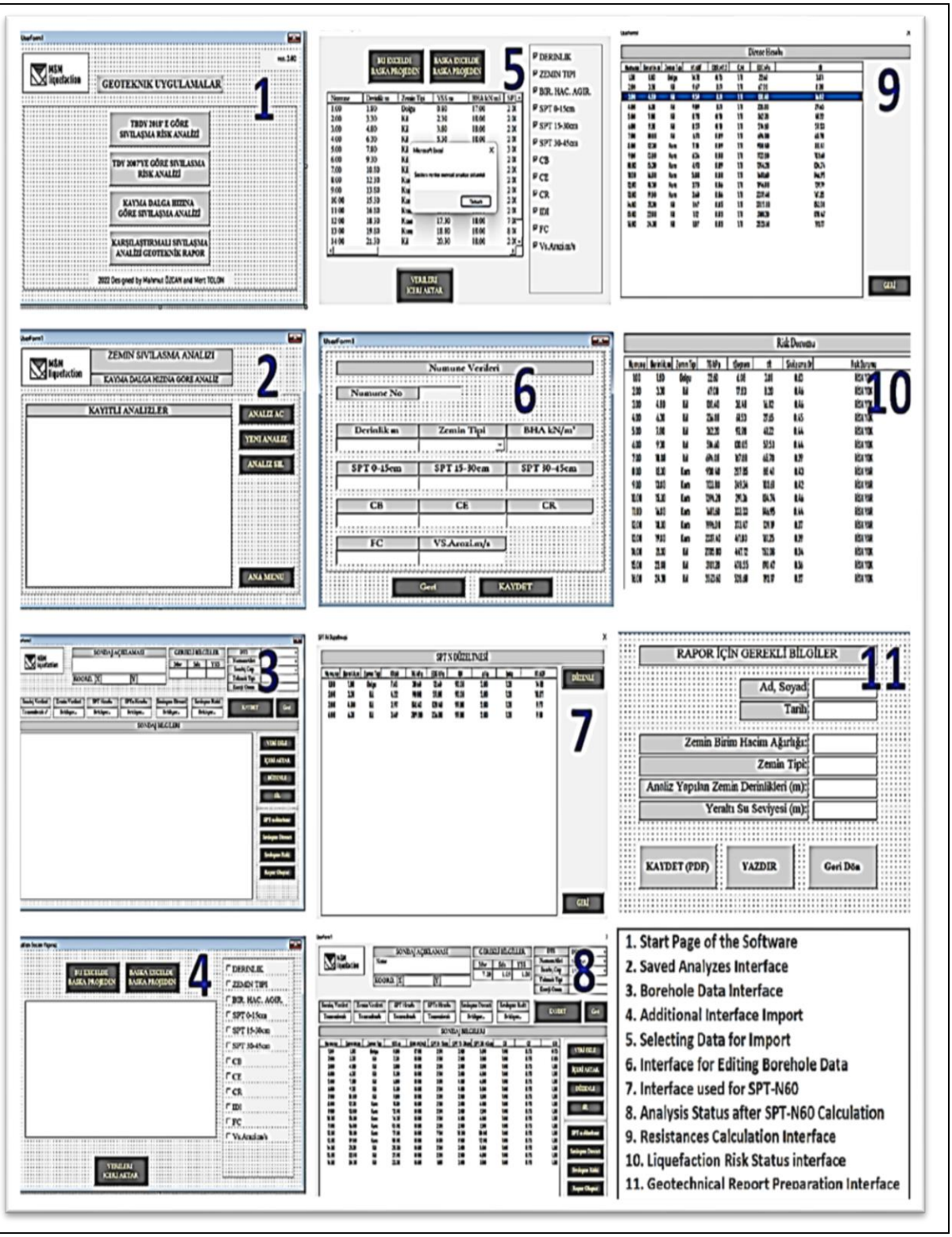

Figure 3. Flow chart of developed soil liquefaction analysis software based on VBA.

An example evaluation of the relationship of Depth - Corrected SPT-N Value Graph Obtained with the Developed Module is given in Figure 6.

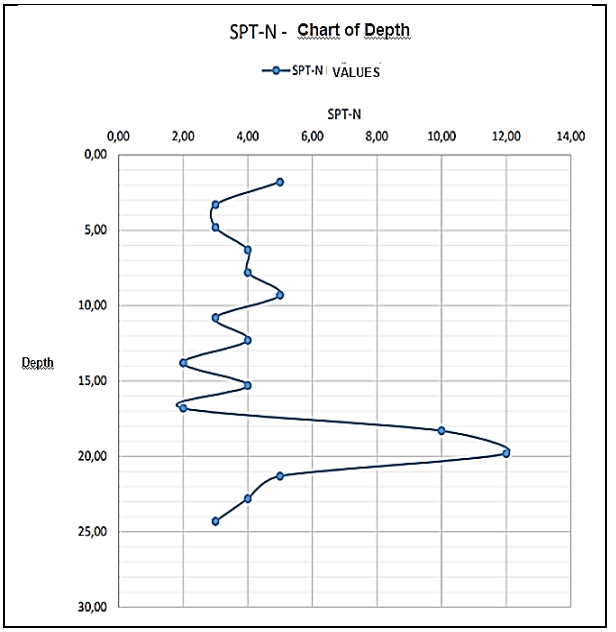

Figure 6. Depth - Corrected SPT-N Value Graph Obtained with the Developed Module.

A report can be obtained for each analysis and the information on the report can be entered and either automatically printed or saved in PDF format if desired. Thus, institutional memory will be provided with the relevant program and the existing geotechnical report database (Figure 7).

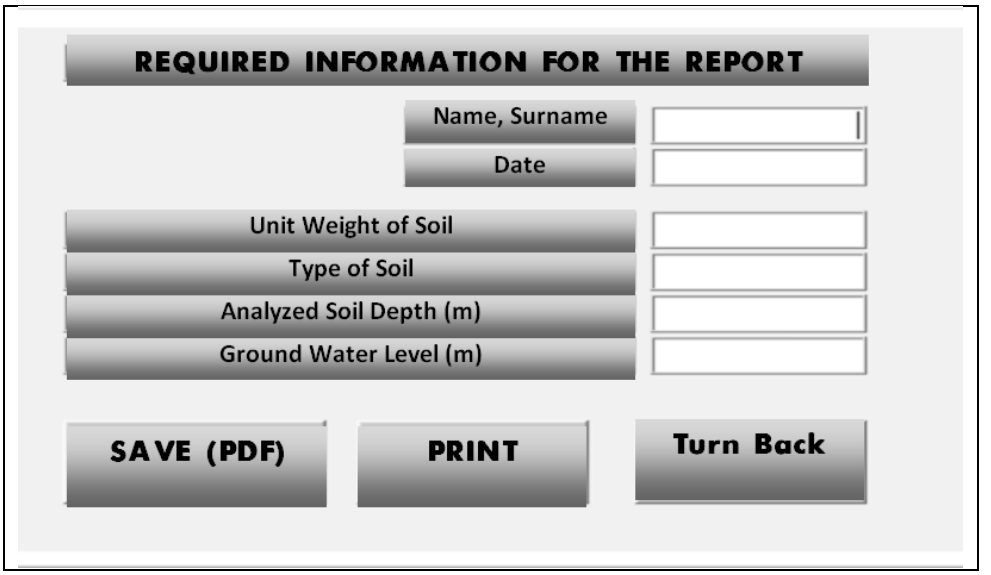

Figure 7. Geotechnical Report Saving and Printing Module.

The reliability of the results was compared with the program developed by comparing with traditional methods. In this sense, the graph of the variation of the liquefaction risk in the ground according to the TSC-2007, Shear

Wave Velocity methodology and TSC-2018, obtained with the program developed based on a sample case study, is presented in Figure 8. It has been seen that the results of the liquefaction risk safety factor required to be obtained according to the relevant regulations, both with simplified hand calculations and the values obtained from the program, are extremely significant and convergent.

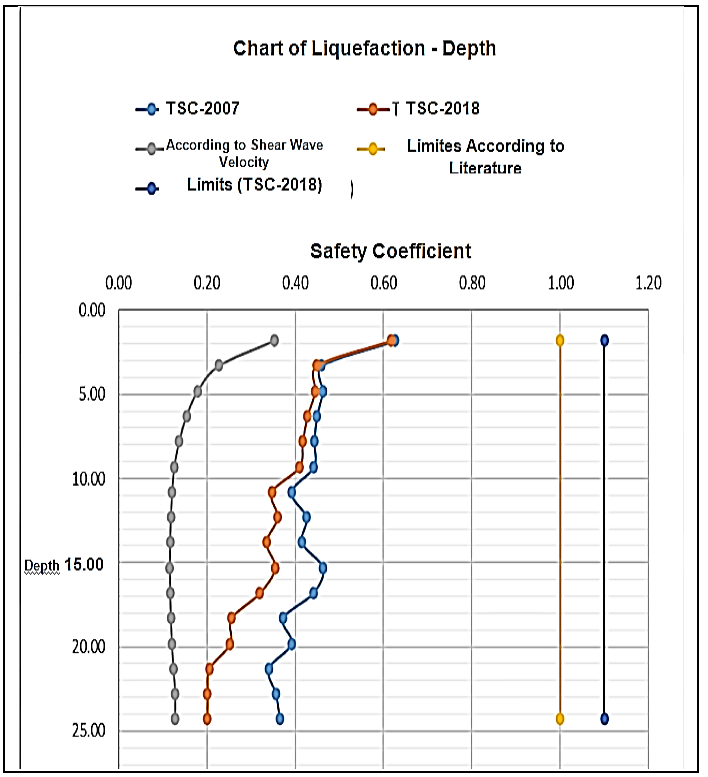

Figure 8. Liquefaction Risk – Depth Change Graph obtained with the Developed Program.

4. DISCUSSION AND RECOMMENDATIONS

With the program created within the scope of the study, it is possible to make an early intervention since the determination of soils at risk of liquefaction is made by examining certain parameters. Soil grouting, dynamic compaction etc. on soils that are found to be risky during soil surveys and studies. The intergranular spaces should be filled by using remediation methods, the injected material should be resistant to water and divert water from the environment, and should be of a type that will increase the resistance by tightening the ground, and in this way, the risk of liquefaction in the ground can be reduced.

By using this program, the decision-making mechanisms of field or office engineers in terms of liquefaction can be accelerated. An economical solution can be found by obtaining soil liquefaction analyses as a preliminary research at the beginning of the project, in accordance with the regulation, in a fast and reliable manner, and by making the risky-predicted soils safer with soil improvement methods. The development of the program by correcting itself will contribute to future studies. No comparison has been made with any other analysis method, and this is seen as a limitation of the study and is planned to be included in future studies.

When the developed program and the results obtained are examined, it is thought that a program that presents the results to the user more clearly in terms of the engineer's interpretation, since the program progresses in a more understandable and sequential manner compared to the previously developed liquefaction analysis programs based on MS Excel in the literature.

Given the increasing demand for safe and economically viable construction practices in earthquake-prone regions such as Turkey, the integration of the Visual Basic-based liquefaction analysis tool into the broader framework of the 2018 Turkish Seismic Code holds significant potential. The tool, designed to rapidly and accurately assess soil liquefaction risk using on-site data and laboratory tests, aligns well with the objectives of the 2018 Turkish Seismic Code by addressing the critical soil factors contributing to structural failures. Its application can be expanded to other geotechnical standards within the 2018 Turkish Seismic Code by incorporating additional parameters and methodologies relevant to diverse soil conditions and seismic responses. This approach not only facilitates early and effective interventions but also ensures that construction projects commence with realistic budgets and robust structural models. By continuously updating the tool with the latest regulatory requirements and incorporating comparative analyses with other existing methods, it can serve as a comprehensive and adaptive solution for geotechnical engineers, thereby enhancing the overall resilience and safety of new and existing buildings in seismic zones.

As a future work-study, the addition of other liquefaction analysis methods in the literature in the past and today and other methods that will be included in the following regulations will be added to the analysis model, and the development of the database with the existing different land data is considered as future studies.Also, as a future work plan to effectively expand this study within construction projects, several steps can be taken. First, integrating the Visual Basic-based liquefaction analysis program into a broader suite of geotechnical tools used by engineering firms can enhance its adoption and utility. By ensuring compatibility with other industry-standard software, the program can become a valuable component of a comprehensive geotechnical analysis toolkit. Additionally, conducting field trials across diverse geographical areas and soil types can validate the program’s accuracy and reliability in various conditions, encouraging wider use. Collaborating with regulatory bodies to update and refine the program based on the latest seismic codes and best practices will also ensure its relevance and compliance with evolving standards.

5. CONCLUSION

The findings demonstrate that the application can significantly improve the safety and reliability of construction projects by enabling early and precise intervention. By incorporating methods such as soil grouting and dynamic compaction, the risk of liquefaction can be mitigated, ensuring that new structures do not contribute to the existing stock of unsafe buildings. Furthermore, the study underscores the importance of considering soil-structure interaction in seismic design, as neglecting this aspect can lead to severe infrastructure damage.The program's ability to present results clearly and sequentially makes it a valuable tool for engineers, offering a more user-friendly experience compared to existing MS Excel-based liquefaction analysis programs. However, the study acknowledges its limitation in not comparing the developed method with other analysis techniques, which is an area for future research.

In conclusion, the integration of this innovative liquefaction analysis tool into geotechnical practice represents a significant advancement in earthquake risk mitigation. Future work should focus on expanding the program's database, incorporating additional liquefaction analysis methods, and continuously updating the model in line with evolving seismic regulations. By doing so, the program can further enhance its accuracy and applicability, contributing to safer and more resilient construction practices in seismic regions.

Acknowledgements

There are no Acknowledgements.

Funding

The authors have no financial interests, which may be considered as potential competing interests.

Declaration of Competing Interest

Competing interest statement declared by authors. This statement must also appear in your manuscript before the references.

References

[1]Yeşilce, Y. veDemirdağ O., 2020. DepremParametreleri, DepremSempozyumu.
[2]Dülger, M., 2015. UBCSAND model ilesıvılaşmadavranışınınincelenmesi, YüksekLisansTezi, Yıldız Teknik Üniversitesi Fen BilimleriEnstitüsü, İstanbul.
[3] TMMOB JeolojiMühendisleriOdası, 2019. "Türkiye Bina DepremYönetmeliği İle UyumluBasitleştirilmiş Zemin SıvılaşmaPotansiyeliAnaliziHesabı", Seminer, Ankara.
[4] Wells, D.L., ve Coppersmith, K.J., 1994. New empirical relationships among magnitude, rupture length, rupture width, rupture area, and surface displacement: Bulletin Seismological Society of America, v. 84, p. 974–1002.
[5] Seed, HB., Idriss, IM., 1971. Simplified Procedure for Evaluating Soil Liquefaction Potential, Journal of the Soil Mechanics and Foundations Division, 97, pp. 1249-1273.
[6] Sykora, D. W., 1987. Cretation of a Data Base of Seismic Shear Wave Velocities for Correlation Analysis. Geotechnical Laboratory Miscellaneous Paper GL87-26, U.S. Army Engineer Waterways Experiment Station, Vicksburg, MS.
[7] Robertson, P.K., Woeller, D.J., Finn, W.D.L., 1992. Seismic Cone Penetration Test for Evaluating Liquefaction Potential Under Cyclic Loading. Canadian Geotechnical Journal, Ottawa, 29, 686- 695.
[8] Andrus, R.D., Stokoe II, K.H., 1997. Liquefaction Resistance Based on Shear Wave Velocity. NCEER Workshop on Evaluation of Liquefaction Resistance Of Soils, Technical Report NCEER-97-0022, T.L.Youd and I.M. Idriss, (Eds.), Held (1996), Salt Lake City, UT, Buffalo, NY, 89-128.
[9] Andrus, R.D., Stokoe II, K.H., 1999. A Liquefaction Evaluation Procedure Based on Shear Wave Velocity. Wind and Seismic Effects US/Japan Natural Resources Devolopment Program Joint Meeting 31st Technical Memorandum of PWRI 3653 Proceedings 71-78.
[10] Andrus, R.D., Stokoe II, K.H., 2000. Liquefaction Resistance of Soils from Shear-Wave Velocity. Journal of Geotechnical and Geoenvironmental Engineering, (ASCE) 126, 1015-1025.
[11] Uyanık, O., 2002. KaymaDalgaHızınaBağlıPotansiyelSıvılaşmaAnalizYöntemi, DoktoraTezi, DEU. Fen BilimleriEnstitüsü, İzmir.
[12] TBDY (TBSC), 2018. Türkiye Bina DepremYönetmeliği 2018: DepremEtkisiAltındaBinalarınTasarımıçinEsaslar", TürkiyeCumhuriyeti, Ankara.

September 2024, Vol:2, Issue:2

International Journal of New Findings in Engineering, Science and Technology

journal homepage: *https://ijonfest.gedik.edu.tr/*

The Current Progress in the Application of Friction Stir Welding in Transportation Industries

Gürel Çam[a]

[a] *Iskenderun Technical University, Faculty of Engineering and Natural Sciences, Iskenderun, Hatay, TÜRKİYE e-mail:gurel.cam@iste.edu.tr*

Abstract

The use of the friction stir welding (FSW) process as a relatively new solid-state welding technology in the transport industries has pushed forward several developments in different related aspects of these strategic industries. Due to the geometric limitations involved in the conventional FSW process, many variants have been required in recent years to suit the different types of geometries and structures. As a result, numerous variants such as refill friction stir spot welding (RF-SSW), stationary shoulder friction stir welding (SS-FSW), and bobbin tool friction stir welding (BT-FSW) have been developed. The RF-SSW variant eliminates the hole left at the end of the weld line where the stirring tool is pulled out. This facilitates the use of FSW process in component welding. The SS-FSW is low heat input process compared to conventional FSW which offers several advantages such as narrower HAZ and reduced microstructural and mechanical variation across the weld region. Similarly, BT-FSW process eliminates weld root defects and penetration defects and achieves a full penetration weld. Thus, these developments have led to a wider application of FSW technology in various transport industries, such as automobile, shipbuilding, high-speed trains, and aerospace industries. The main aim of this review article is to summarize the state of knowledge regarding the application of the FSW process in the aerospace industry and to make suggestions for future work.

Keywords: Joining, friction stir welding, refill friction stir spot welding, stationary shoulder friction stir welding, bobbin tool friction stir welding.

1. INTRODUCTION

Welding is a unique manufacturing method that allows the production of complex parts from materials that are difficult to shape or not economical. In these cases, individual parts are manufactured separately and then assembled using a suitable joining technique. In addition, welding technology is generally a complementary process, not an alternative to other manufacturing methods. Weldability is therefore one of the most important factors determining the widespread application of new materials. In recent years, the demand for complex products that cannot be produced in one piece or are very costly to produce, especially in the transportation industry, has increased due to developing technology. Electric vehicles, high-speed trains, jumbo jets and cruisers (large passenger ships) where fuel consumption is important are examples of such products.

https://doi.org/10.61150/ijonfest.2024020208

The progress made in the weldability of materials used in engineering applications with the development of new welding technologies such as friction stir welding (FSW) further increases the importance of welding technology. FSW, which was developed and patented by The Welding Institute (TWI) in England in the early 1990s, is generally used in longitudinal welding processes of sheets and plates both in butt or overlap configurations [1]. The application of the friction stir welding method is shown schematically in Figure 1 [2]. FSW is still considered the most important development in the welding of materials in the last 30 years [2-26]. Nowadays, this welding technique is used commercially for joining Al-alloys in many industries such as the maritime industry [27-29], high-speed train manufacturing [27,29], and the aviation industry [27,30,31]. Standard length Al-extrusion panels used on high-speed cruise ships are currently joined by this method. In addition, this method is also used successfully in the welding of fuel tanks used in aviation applications [31]. This welding technique is also used to make the butt joining of hollow Al extrusions used in the construction of high-speed train carriages in Japan [30]. The method has recently begun to be widely used in battery carrier systems of electric vehicles. Additionally, some FSW variants have been developed in recent years to improve welded joint performance. For example, the recently developed friction stir spot welding (FSSW) is a candidate to replace the traditional resistance spot welding in overlap welding applications of Al-alloy sheets where sealing is not required [32]. As a matter of fact, this method is successfully used in overlap welding operations of Al-alloy sheets, which is difficult by resistance spot welding. Thus, this variant, together with conventional FSW, will enable the use of lightweight Al-alloys in the manufacture of electric vehicles. This technique is currently on the brink of industrial use in the lap jointing of Al alloy sheets in the automobile industry. The method also presents itself as a potential candidate to replace riveting.

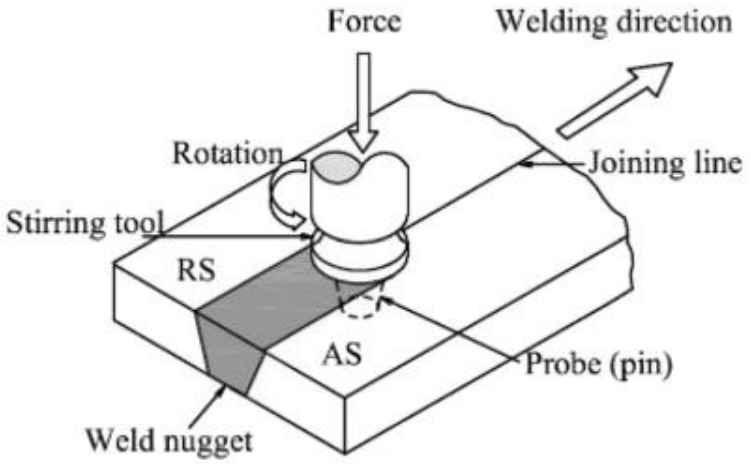

Figure 1. Schematic presentation of friction stir welding [2].
(AS: advancing side and RS: retreating side).

Although the FSW technique was initially developed for Al alloys [2-26,33-37], it also has great potential for use in the joining of Mg alloys [8,14,38-40], Cu alloys [8,41-43], Ti-alloys [8,17,18].], Al-alloy matrix composites [44-46], lead [47], steels [8,48-53], and thermoplastics [54-56]. In addition, it has also potential for joining different Al-alloys with similar behavior such as similar melting temperatures and hot workability [4,57-60] as well as for welding Al-alloys with Mg-alloys [61-64] and for joining different types of steel [65-70]. Various joint types such as butt, overlap, and T-joints can be produced with friction stir welding (Figure 2). However, cost-effective stirring tools are needed to join metal matrix composites and metals with high melting temperatures, such as steels and Ti-alloys, by friction stir welding [8, 12].

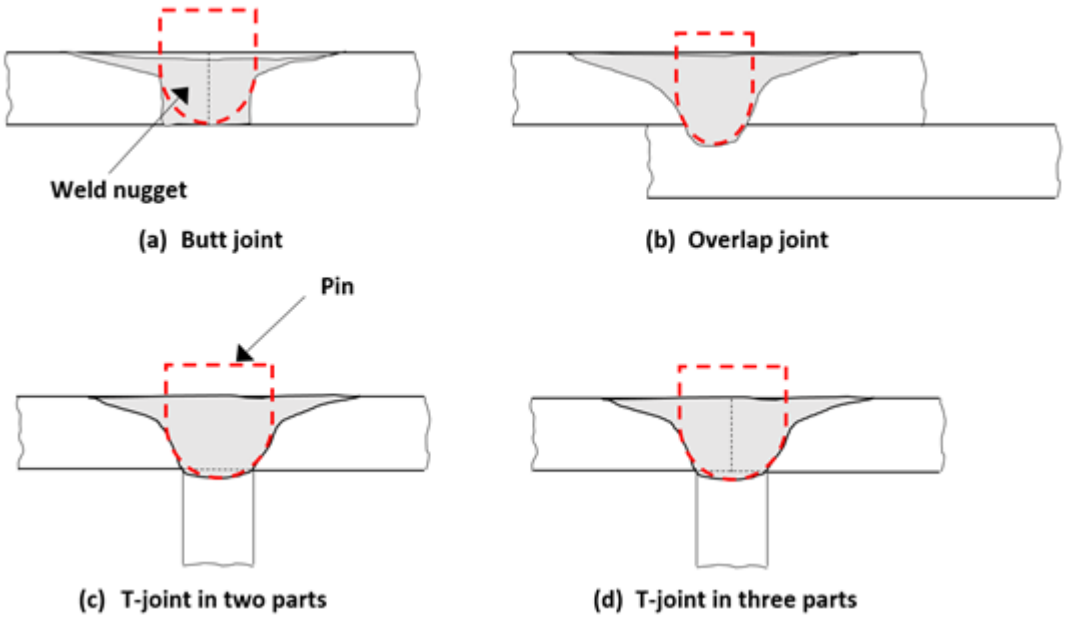

Figure 2. Joint types obtained by the FSW method: (a) butt joint, (b) overlap joint, (c) T-connection with two pieces of plate, and (d) T-connection with three pieces of plate [6].

The traditional FSW method does not give good results in cases where the mechanical properties of welded joints are inadequate as a result of high heat input, or to obtain joints that require high performance, especially in welding processes of different metals. For this reason, new FSW variants such as external cooling-assisted FSW [71-73] such as underwater FSW, and ultrasonic vibration-assisted FSW [74-77] have also been developed to reduce heat input thus to achieve high-performance joints and to prevent or minimize the formation of brittle intermetallic compounds in the welding of different metals, respectively. In recent years, in addition to external cooling-assisted and ultrasonic vibration-assisted FSW applications, new FSW variants have also been developed as a result of intensive research on the application of the method to different geometries and structure types. The most important of these new FSW variants are refill friction stir spot welding (RF-FSSW), stationary shoulder friction stir welding (SS-FSW), and bobbin tool friction stir welding (BT-FSW). These relatively new FSW variants will be discussed in the following section.

2. NEW FRICTION STIR WELDING VARIANTS

2.1 Refill Friction Stir Spot Welding

One of the new friction stir welding variants is friction stir spot welding (FSSW). The application of the friction stir spot welding technique is schematically illustrated in schematically in Figure 3 [4,78]. This joining process is done in three stages: plunging, stirring and tool withdrawal. After spot welding is achieved with this FSW variant, a gap is formed as a result of the tool withdrawal, as seen in Figure 3. In addition to the formation of voids, this process has other disadvantages such as a reduction in top plate thickness and hook-shaped joining [79]. As a result

of efforts to prevent these weld defects, a new variant of this technique has also been developed in recent years. This new version of FSSW is called refill friction stir welding (RF-FSSW). Figure 4 schematically shows the refill friction stir spot welding process [3,80].

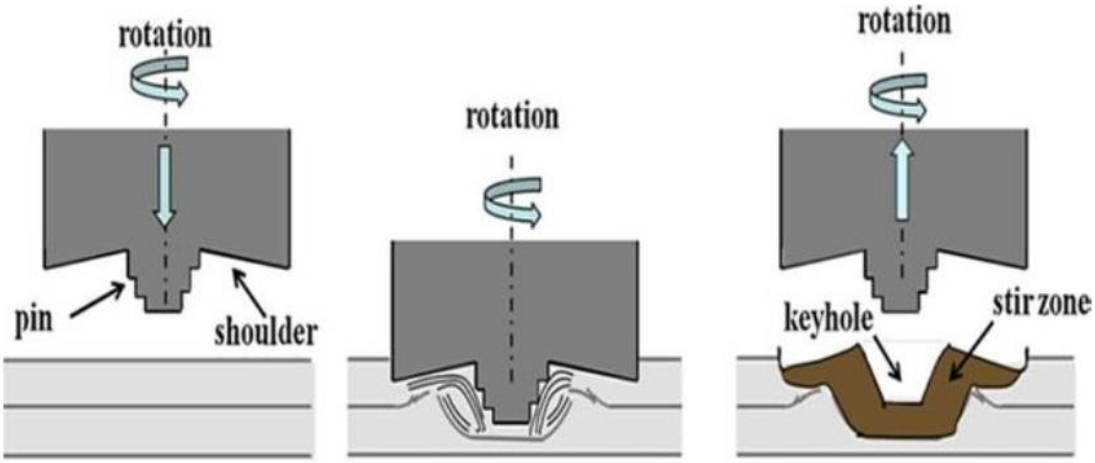

Figure 3. Schematic presentation of the stages of friction stir spot welding (FSSW) [78].

In the first stage of the RF-FSSW process, a preheating phase is initiated while the probe and shoulder are aligned at the same level on the top sheet surface. The friction effect at this stage softens the workpiece, allowing the stirring tool to rotate at high speed to begin plunging with alternating motion between the probe and the shoulder. In the second stage, the shoulder begins to plunge, causing further softening of the material so that the plasticized material is injected into the pin slot. In the third stage, the probe begins plunging to re-inject the displaced material. In the final stage, the shoulder and probe are again aligned parallel to each other on the top surface to create a void-free spot weld [81]. The RF-FSSW technique was successfully used by Boldsaikhan et al. [81] to weld sheets of aerospace aluminum alloys AA7075-T6 and AA2024-T3. In this study, AA2024-T3 was used as the lower plate representing the outer skin of the aircraft structure and AA7075-T6 was used as the upper plate representing the stiffener side of the aircraft's external skin-stiffening structure. Recently, this FSW variant has also been successfully employed to produce defect-free lap joints in Al-alloys such as Al 6061 for the production of cellular I-beams [82] and dissimilar joints such as between different Al-alloys for battery applications [83] and Al-Cu for battery tab-to-busbar applications [84].

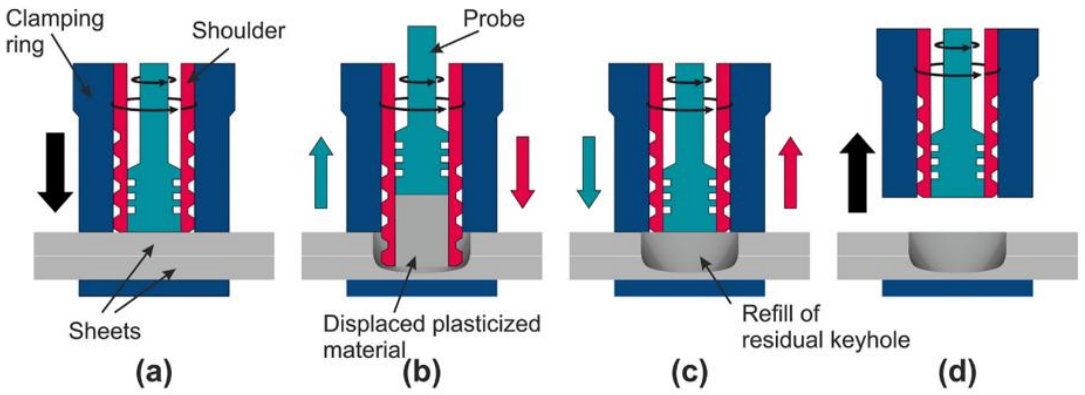

Figure 4. Schematic presentation of the stages of refill friction stir spot welding (RF-FSSW):

(a) clamping of sheets, (b) tool plunging and withdrawal of probe, (c) c) shoulder and probe reaching back to the sheet's surface and refilling the keyhole, and (d) release of the clamping force and tool withdrawal [3,80].

2.2 Stationary Shoulder Friction Stir Welding

The use of the FSW process in joining titanium-based alloys such as Ti-6Al-4V, which is widely used in aerospace applications, is limited due to their poor thermal conductivity. When using conventional FSW tools, heat is generated mainly at the top surface, resulting in a significant temperature gradient across the thickness of the welded plate, especially in thick plates. This problem, together with the limited but relatively high hot working range of alloys such as Ti-6Al-4V, makes it almost impossible to join titanium without defects with conventional FSW [85]. The Welding Institute (TWI) has developed the stationary shoulder friction stir welding (SS-FSW) variant to overcome this problem and weld titanium alloys using FSW [86]. The SS-FSW technique is shown schematically in Figure 5 [87]. In the SS-FSW process, the shoulder of the stirring tool moving along the weld does not rotate, only the pin of the stirring tool rotates within this fixed shoulder. Having the shoulder fixed significantly reduces the contribution of the shoulder to heat production and affects the heat distribution throughout the weld depth. Therefore, in the SS-FSW process, since the shoulder is stationary, a highly focused heat input is produced around the tool pin (i.e., probe) and excessive surface heating does not occur [88]. The SS-FSW technique was successfully applied by Russell et al. [88] in the welding of 6.35 mm thick Ti-6Al-4V plates and it was reported that the stationary shoulder provided more uniform heating throughout the thickness. As a result, it was observed that the microstructure was uniform throughout the entire weld cross-section. Additionally, the SS-FSW approach has also been used in welding aluminum alloys to develop uniform microstructure and crystallographic texture throughout the plate thickness [89].

In addition to porosity formation in fusion welding techniques, the most challenging obstacle in fusion welding and conventional FSW of high strength aerospace Al-alloys is extreme strength loss in the HAZ due to overaging resulting from the relatively high heat input [6-8,57,58,90-93]. The strength loss in the weld region is called strength undermatching and this leads to failure in this area [94-97]. Thus, it should be eliminated or at least minimized. The SS-FSW variant offers an advantage in this respect due to the stationary shoulder which reduces the heat input experienced by the workpieces during the joining process. For example, Wu et al. [87] conducted a detailed research to compare the SS-FSW method with the traditional FSW technique in welding high-strength aerospace Al-alloy AA7050-T765 sheets. In this study, they aimed to examine the effect of FSW welding parameters on power consumption by using the same stirring tool geometry in both conventional FSW and SS-FSW processes. The results obtained showed that the required heat input in the SS-FSW technique was 30% lower than in the traditional FSW technique. Additionally, the use of the SS-FSW technique has been determined to offer many advantages. These are:

- Formation of narrower and parallel heat affected zone (HAZ).

- Less variation in microstructure and other properties across the weld cross-section.
- Better cross-sectional tensile properties than traditional FSW method.
- Improvement in surface roughness due to the ironing effect of the non-rotating tool on the upper surface.

Similarly, the process has also been used to produce defect-free joints in Al-Li alloys (i.e., 2A97) in a recent study, and the best combination of strength and ductility was achieved at a rotational speed of 1000 rpm [98]. The SS-FSW process also offers an advantage in butt joining of dissimilar metals such as Al-alloys to Mg-alloys where a low heat input is required in order to reduce brittle intermetallic formation. However, the insufficient heat input may result in unfavorable material mixing in the weld zone which reduces the weld strength. Therefore, the process is usually used in combination with ultrasonic vibration, i.e. ultrasonic-assisted SS-FSW [99-102]. For instance, Hu et al. [101] employed an ultrasonic vibration and stationary shoulder-assisted hybrid FSW method to obtain dissimilar Al-Mg joints, and a maximum UTS of 161 MPa was achieved by this hybrid technology. Similarly, You et al [102] achieved a high-quality dissimilar Al-Cu joint by the ultrasonic vibration-assisted stationary shoulder FSW process.

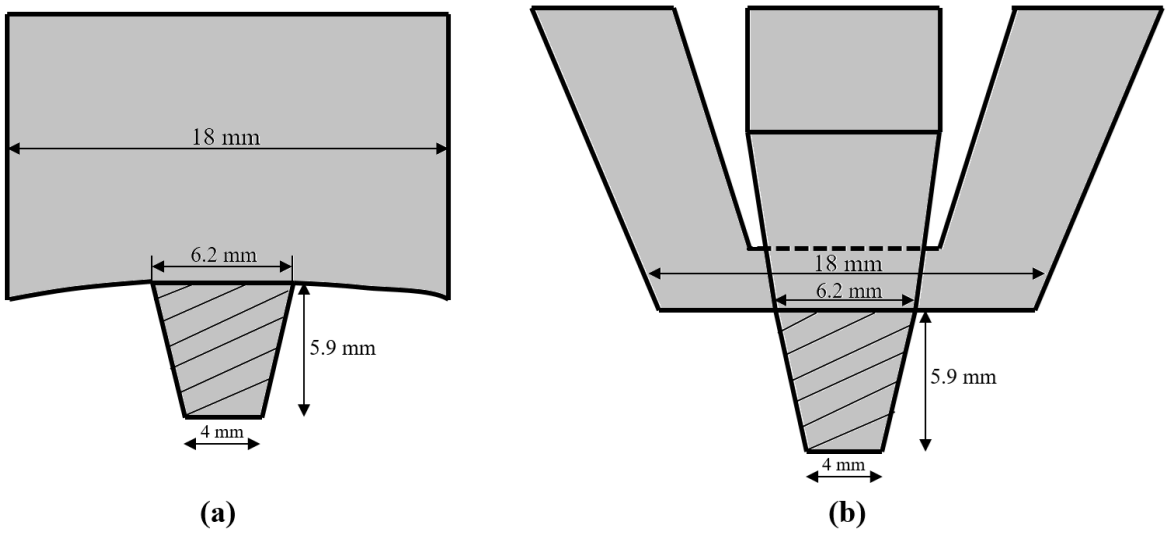

Figure 5. Comparison of the traditional FSW stirring tool and the stirring tool used in the SS-FSW method: (a) Traditional FSW and (b) SS-FSW [87].

On the other hand, it has been reported that when very high tool traverse and rotation speeds are used, a negative effect such as "speed cracking", which is observed in hot extrusion, may occur [87]. Owing to relatively low heat input compared to conventional FSW, the SS-FSW method has also been widely used to join some different and similar aluminum alloy sheets with high strength employed in aerospace applications [103-108]. These results indicate that the SS-FSW technique is one of the promising FSW variants for aerospace applications.

2.3 Bobbin Tool Friction Stir Welding

The use of double-shoulder (top and bottom shoulder) FSW tools, known as bobbin tools, represents one of the new developments of FSW technology, which has many advantages in terms of welded joint quality as well as machine flexibility and capacity [109-116]. The advantages of the bobbin tool friction stir welding (BT-FSW) method are:

- Since full penetration weld is achieved, weld root defects and penetration defects do not occur.
- Low Z forces on fixture and machine.
- No support plate required due to lower shoulder use.
- Low distortion due to low Z forces applied.
- Thickness variation tolerance ability.
- Ability to join closed profiles such as hollow extrusions.
- More homogeneous mechanical properties throughout the thickness of the weld section.

Figure 6 (a) shows a schematic representation of FSW with two shoulder (upper and lower) bobbin tools and (b) shows an example of the fixture setup used in the BT-FSW process [115]. A support plate is not needed in the BT-FSW method. This feature makes the method ideal for welding hollow profiles, and at the same time, since the applied vertical forces are low, less buckling and less distortion occur in the welded parts.

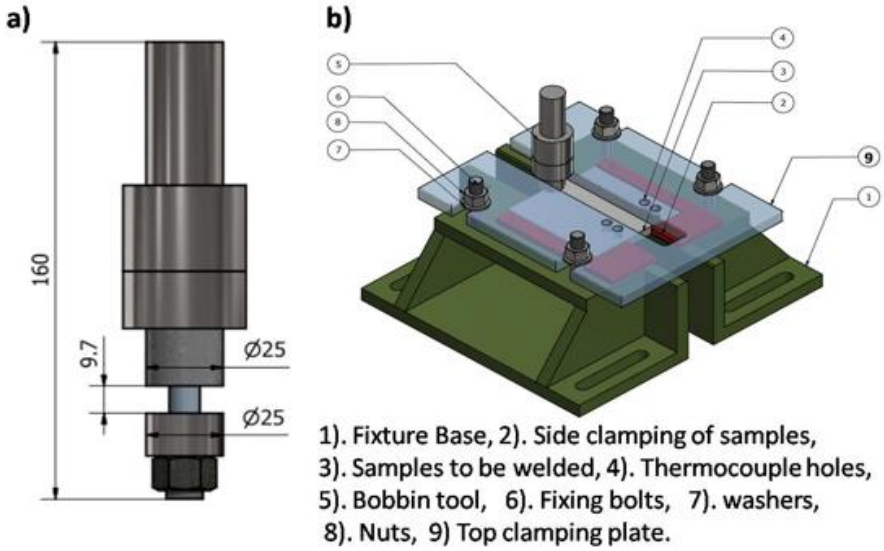

Figure 6. Schematic representation of the bobbin tool FSW technique: (a) an FSW bobbin tool used for welding 10 mm thick aluminum and (b) an example fixing setup used in the bobbin tool FSW process [115].

For example, Threadgill et al. [109] joined AA6082-T6 thick plates with FSW using both a bobbin tool and a conventional tool and reported that successful welded joints were obtained with both tools. However, they demonstrated that when the bobbin tool is used, the net axial force on the workpiece is almost zero, which has significant beneficial effects on machine design and cost. Similarly, Xu et al. [112,113] examined the welding of 12 mm thick AA7085-T7452 aluminum alloy sheets with both BT-FSW and conventional FSW and reported that successful joints were obtained in both methods. However, the joints obtained with the BT-FSW technique showed lower welding performance due to the presence of a Lazy S defect resulting from a larger amount of heat input [113]. On the other hand, Yang et al. [114] reported in a comparative study on AA6061-T4 sheets with BT-FSW and traditional FSW that similar welding performance values (approximately 93%) were obtained in both methods. Moreover, Wang et al. [110] investigated the weldability of 3.2 mm thick high-strength Al-alloy (AA2198) sheets used in aviation with BT-FSW and reported that strong welded joints (welding efficiency = 80%) were produced with different FSW parameters. Similarly, Ahmed et al. [116] conducted a study investigating the effect of tool pin profile and feed rate on the mechanical properties of aluminum alloy sheets welded by BT-FSW. The findings showed that the mechanical properties of the base plate can be preserved in the weld zone by optimizing the BT-FSW parameters.

However, the macrostructure of the stir zone obtained by the BT-FSW is governed by the refill behaviour of the plasticised metal. The refill occurs preferentially near the upper and lower shoulders, creating a triangular gap at the mid-thickness level. A recent study by Li et al [117] reported that tapering the stirring probe reduces the volume of displaced metal, leaving a smaller gap to be refilled during welding which leads to defect-free joints. More recently, a bobbin tool concept having one rotating and one stationary shoulder has been proposed [118]. This technique is known as semi-stationary shoulder bobbin-tool FSW. For instance, Goebel et al. [119] achieved flawless joints of AA2198 alloy by this variant and reported 30% less heat input and improved joint tensile properties as compared to conventional BT-FSW method. Similarly, Scupin [120] performed the semi-stationary shoulder BT-FSW to AA6082 alloy. They claimed that high welding speeds up to 2900 mm/min could be achieved, and the joint exhibited superior tensile properties close to those of the base metal. Furthermore, Li et al [121] very recently applied this technique to join AZ31B Mg-alloy. They reported that the use of semi-stationary BT-FSW method led to reduced forces as well as torque, enabling higher welding speeds up to 1500 mm/min.

3. GENERAL REMARKS

This review article clearly shows that defect-free butt joints can be obtained with the FSW process in Al-alloys and many other metals, particularly by employing the FSW variants. In addition, defect-free lap joints (spot welding) are readily achieved with refill FSSW while full penetration butt-joints can be obtained by the bobbin tool FSW process. However, the influence of welding conditions on joint performance has been determined to date only for Al-, Mg- and Cu-alloys. Today, friction stir welding (butt and lap welding applications) is currently used industrially to join Al alloys in the manufacture of ships, aircraft and space shuttles, trains and other vehicles. Although there is some work conducted particularly on SS-FSW of Ti-alloys and the application of the FSW variants such as SS-FSW in combination with ultrasonic vibration assistance to join Al-alloys with Mg-alloys, there is a need for further research on the applicability of the FSW variants in other structural alloys such as Mg-alloys and dissimilar metal combinations. The progress to be made in the welding of Al and Mg alloys in both similar and different combinations by friction stir welding variants will enable the mass production of light transportation systems, thus providing a significant reduction in fuel consumption. As a result, the application of this new welding method will increase in the coming days, especially in shipbuilding, aircraft and aerospace industry, automotive industry and other manufacturing sectors.

However, since high precision and high-quality part production is needed in the transportation industries, especially in the aviation industry, FSW variants suitable for the part geometry to be produced should be used and advanced NDT techniques such as special ultrasonic method (phased array ultrasonic method) must be employed to

control the welded parts throughout production to determine whether the friction stir welded joints contain weld defects. Moreover, appropriate methods need to be developed in parallel to repair these defects to the highest standard and feasibility. Provided these shortcomings are overcome, the FSW technology in combination with the laser beam welding (LBW) process will enable significant weight savings in the aviation industry as well as in other transportation systems.

References

[1] Thomas, W.M., et al., International Patent Application No. PCT/GB92/02203 and GB Patent Application No. 9125978.8 and US Patent Application No. 5,460,317, Dec.1991.
[2] Ahmed, M.M.Z., El-Sayed Seleman, M.M., Fydrych, D., Çam G., A review on friction stir welding of dissimilar Al- and Mg-alloys: Scientometric analysis and strategies for achieving high-quality joints, Journal of Magnesium and Alloys, 2023, 11, 4082-4127.
[3] Ahmed, M.M.Z., El-Sayed Seleman, M.M., Fydrych, D., Çam G., Friction stir welding in the aerospace industry: The current progress and state-of-the-art review, Materials, 2023, Vol. 16, Article Number: 2971.
[4] Çam, G., Javaheri, V, Heidarzadeh, A., Advances in FSW and FSSW of dissimilar Al-alloy plates, J. Adhes. Sci. Technol., 2023, 37 (2), 162-194.
[5] Khaliq, U.A., Yusof, F., Chen, Z., Mohd Isa, M.S., Çam, G., A comprehensive review on friction stir welding of aluminum with magnesium: A new insight on joining mechanisms by interfacial enhancement, J. Mater. Res. Technol., 2023, 27, 4595-4624.
[6] Kashaev, N., Ventzke, V., Çam, G., Prospects of laser beam welding and friction stir welding processes for aluminum airframe structural applications, J. Manuf. Proces., 2018, 36, 571-600
[7] Çam, G. and İpekoğlu, G., Recent developments in joining of aluminium alloys, Int. J. Adv. Manuf. Technol., 2017, 91 (5-8), 1851-1866.
[8] Çam, G., Friction stir welded structural materials: Beyond Al-alloys, Int. Mater. Rev., 2011, 56 (1), 1-48.
[9] Mishra, R.S. and Ma, Z.Y., Friction stir welding and processing, Mater. Sci. Eng. R, 2005, 50, 1-78.
[10] Threadgill, P.L., Leonard, A.J., Shercliff, H.R., Withers, P.J., Friction stir welding of aluminium alloys, Int. Mater. Rev., 2009, 54, 49-93.
[11] Nandan, R., Debroy, T., Bhadeshia, H.K.D.H., Recent advances in friction-stir welding – Process, weldment structure and properties. Prog. Mater. Sci., 2008, 53, 980-1023.
[12] Thomas, W.M., Johnson, K.I., Wiesner, C.S., Friction stir welding - Recent developments in tool and process technologies, Adv. Eng. Mater., 2003, 5, 485-490.
[13] Mishra, R.S. and Mahoney, M.W., Eds., 'Friction Stir Welding and Processing', ASM International, Materials Park, Ohio, USA, 2007.
[14] Singh, K., Singh, G., Singh, H., Review on friction stir welding of magnesium alloys, J. Magnes. Alloy., 2018, 6 (4), 399-416.
[15] Padhy, G.K., Wu, C.S., Gao, S., Friction stir based welding and processing technologies – process, parameters, microstructures and applications – A review, J. Mater. Sci. Technol., 2018, 34 (1), 1-38.
[16] Wahid, M.A., Khan, Z.A., Siddiquee, A.N., Review on underwater friction stir welding: A variant of friction stir welding with great potential of improving joint properties, Transactions of Nonferrous Metal Society of China, 2018, 28 (2), 193-219.
[17] Mironov, S., Sato, Y.S., Kokowa, H., Friction-stir welding and processing of Ti-6Al-4V titanium alloy: A review, J. Mater. Sci. Technol., 2018, 34 (1), 58-72.
[18] Gangwar, K. and Ramulu, M., Friction-stir welding of titanium alloys: A review, Materials & Design, 2018, 141 (5), 230-255.
[19] Venkatesh, K.M., Arivarsu, M., Manikandan, M., Arivazhagan, N., Review on friction stir welding of steels, Materials Today: Proceedings, 2018, 5 (5), 13227-13235.
[20] Liu, F.C., Hovanski, Y., Miles, M.P., et al., A review of friction stir welding of steels: Tool, material flow, microstructure, and properties, J. Mater. Sci. Technol., 2018, 34, 39-57.
[21] Yang, X.W., Fu ,T., Li, W.Y., Friction stir spot welding: A review on joint macro- and microstructure, property, and process modelling, Adv. Mater. Sci. Eng., 2014, 1, 1-11.
[22] İpekoglu, G. and Çam, G., Farklı Al-alaşımı levhaların (AA6061/AA7075) sürtünme karıştırma kaynağına temper durumunun etkisi', Mühendis ve Makina, 2012, 53 (629), 40-47.
[23] İpekoglu, G., Akçam, Ö., and Çam, G., Farklı kalınlıktaki AA6061-T6 levhaların sürtünme karıştırma kaynağı için uygun kaynak parametrelerinin belirlenmesi, Afyon Kocatepe Üniversitesi Fen ve Mühendislik Bilimleri Dergisi, 2018, 18 (1), 324-335.
[24] Çam, G., Sürtünme karıştırma kaynağı (SKK) – Al-alaşımları için geliştirilmiş yeni bir kaynak teknolojisi, Mühendis ve Makina, 2005, 46 (541), 30-39.
[25] Yavuz, H. and Çam, G., Yeni bir kaynak teknolojisi: Sürtünme karıştırma kaynağı, Endüstri ve Otomasyon, 2001, 51, 18-20.
[26] Çam, G., Al-alaşımları için geliştirilen yeni kaynak yöntemleri, Kaynak Teknolojisi III. Ulusal Kongresi ve Sergisi, 19-20 October 2001, İstanbul, 2001, 267-277.
[27] Thomas, W.M. and Nicholas, E.D., Friction stir welding for the transportation industries, Mater. Des., 1997, 18 (4-6), 269-273.
[28] Dawes, C.J. and Thomas, W.M., Friction stir process welds aluminum alloys, Weld. J., 1996, 75, 41-45.
[29] Kallee, S.W., Davenport, J., Nicholas, E.D., Railway manufacturers implement friction stir welding, Weld. J., 2002, 81, 47-50.
[30] Johnsen, M.R., Friction stir welding takes off at Boeing, Weld. J., 1999, 78, 35-39.
[31] Ding, J., Carter, R., Lawless, K., et al., Friction stir welding flies high at NASA, Weld. J., 2006, 85, 54-59.
[32] Kawasaki Heavy Industries, Ltd., 'A new method for light alloy joining - Friction spot joining, 2006-2014. www.kawasakirobot.com.

[33] Von Strombeck, A., Çam, G., dos Santos, J.F., et al., 'A comparison between microstructure, properties, and toughness behavior of power beam and friction stir welds in Al-alloys', Proc. of the TMS 2001 (Louisiana, USA, February 12-14, 2001), eds: S.K. Das, J.G. Kaufman, and T.J. Lienert, pub.: TMS, Warrendale, PA, 2001, pp. 249-264.
[34] İpekoğlu, G., Erim, S., Gören Kıral, B., Çam, G., Investigation into the effect of temper condition on friction stir weldability of AA6061 Al-alloy plates, Kovove Mater., 2013, 51 (3), 155-163.
[35] İpekoğlu, G., Gören Kıral, B., Erim, S., Çam, G., Investigation of the effect of temper condition friction stir weldability of AA7075 Al-alloy plates, Mater. Tehnol., 2012, 46 (6), 627-632.
[36] Çam, G., Güçlüer, S., Çakan, A., Serindağ, H.T., Mechanical properties of friction stir butt-welded Al-5086 H32 plate, Mat.-wiss. u. Werkstofftech., 2009, 40 (8), 638-642.
[37] İpekoğlu, G., Akçam, Ö., Çam, G., AA6061-T6 Al-alaşımı levhaların sürtünme karıştırma kaynağında levha kalınlığının kaynak hızına etkisi, Kaynak Teknolojisi X. Ulusal Kongre ve Sergisi (KAYKON 2017), 17-18 Kasım 2017, Ankara, 63-75.
[38] Lee, W.B., Yeon, Y.M., Jung, S.B., Joint properties of friction stir welded AZ31B-H24 magnesium alloy, Mater. Sci. Technol., 2003, 19 (6), 785-790.
[39] Afrin, N., Chen, D.L., Cao, X., Jahazi, M., Microstructure and tensile properties of friction stir welded AZ31B magnesium alloy, Mater. Sci. Eng. A, 2008, 472 (1-2), 179-186.
[40] Xie, G.M., Ma, Z.Y., Geng, L., Effect of microstructural evolution on mechanical properties of friction stir welded ZK60 alloy, Mater. Sci. Eng. A, 2008, 486 (1-2), 49-55.
[41] Çam, G., Serindağ, H.T., Çakan, A., et al., The effect of weld parameters on friction stir welding of brass plates, Mat.-wiss. u. Werkstofftech., 2008, 39 (6), 394-399.
[42] Çam, G., Mistikoglu, S., Pakdil, M., Microstructural and mechanical characterization of friction stir butt joint welded 63%Cu-37%Zn brass plate, Weld. J., 2009, 88 (11), 225-232.
[43] Küçükömeroğlu, T., Şentürk, E., Kara, L., et al., Microstructural and mechanical properties of friction stir welded nickel-aluminum bronze (NAB) alloy, J. Mater. Eng. Perform., 2016, 25 (1), 320-326.
[44] Avettand-Fenoel, M.-N. and Simar, A., A review about friction stir welding of metal matrix composites, Mater. Charact., 2016, 120, 1-17.
[45] Nami, H., Adgi, H., Sharifitabar, M., Shamabadi, H., Microstructure and mechanical properties of friction stir welded Al/Mg2Si metal matrix cast composite, Mater. Des., 2011, 32, 976-983.
[46] Ceschini, L., Boromei, I., Minak, G., et al., Effect of friction stir welding on microstructure, tensile and fatigue properties of the AA7005/10 vol.% Al2O3p composite, Compos. Sci. Technol., 2007, 67, 605-615.
[47] Günen, A., Kanca, E., Demir, M., et al., Microstructural and mechanical properties of friction stir welded pure lead, Indian J. Eng. Mater. Sci., 2018, 25 (1), 26-32.
[48] Küçükömeroğlu, T., Aktarer, S.M., İpekoğlu, G., Çam, G., Investigation of mechanical and microstructural properties of friction stir welded dual phase (DP) steel, IOP Conf. Series: Materials Science and Engineering, 2019, 629, 012010.
[49] İpekoğlu, G., Küçükömeroğlu, T., Aktarer, S.M., et al., Investigation of microstructure and mechanical properties of friction stir welded dissimilar St37/St52 joints, Materials Research Express, 2019, 6 (4), 046537.
[50] Reynolds, A.P., Tang, W., Gnaupel-Herold, T., Prask, H., Structure, properties, and residual stress of 304L stainless steel friction stir welds, Scr. Mater., 2003, 48 (9), 1289-1294.
[51] Meran, C., Kovan, V., Alptekin, A., "Friction stir welding of AISI 304 austenitic stainless steel, Mat.-wiss. u. Werkstofftech., 2007, 38 (10), 829-835.
[52] Çam, G., İpekoğlu, G., Küçükömeroğlu, T., Aktarer, S.M., Applicability of friction stir welding to steels, J. Achiev. Mater. Manuf. Eng. (JAMME), 2017, 80 (2), 65-85.
[53] Çam, G. and Meran, C., Çeliklerin sürtünme karıştırma kaynağı, Mühendis ve Makina, 2009, 50, (599), 24-32.
[54] Forcellese, A., Mancia, T., Pieralisi, M., Vita A., Friction stir welding of additively manufactured blanks in thermoplastic polymer, Procedia CIRP, 2022, 112, 448-453.
[55] Pirizadeh, M., Azdast, T., Ahmadi, S.R., et al., Friction stir welding of thermoplastics using a newly designed tool, Mater. & Des., 2014, 54, 342-347.
[56] Jaiganesh, V., Maruthu, B., Gopinath, E., Optimization of process parameters on friction stir welding of high density polypropylene plate, Procedia CIRP, 2014, 97, 1957-1965.
[57] İpekoğlu, G. and Çam, G., Effects of initial temper condition and postweld heat treatment on the properties of dissimilar friction-stir-welded joints between AA7075 and AA6061 aluminum alloys, Metall. Mater. Trans. A, 2014, 45A (7), 3074-3087.
[58] Çam, G., İpekoğlu, G., Tarık Serindağ, H., Effects of use of higher strength interlayer and external cooling on properties of friction stir welded AA6061-T6 joints, Sci. Technol. Weld. Join., 2014, 19 (8), 715-720.
[59] Ouyang, J.H. and Kovacevic, R., Material flow and microstructure in the friction stir butt welds of the same and dissimilar aluminum alloys, J Mater Eng Perform., 2002, 11, 51-63.
[60] Zhang, C., Cao, Y., Huang, G., et al., Influence of tool rotational speed on local microstructure, mechanical and corrosion behavior of dissimilar AA2024/7075 joints fabricated by friction stir welding, J. Manuf. Processes, 2020, 49, 214-226.
[61] Shah, L.H., Othman, N.H., Gerlich, A., Review of research progress on aluminium-magnesium dissimilar friction stir welding, Sci. Technol. Weld. Joining, 2018, 23, 256-270.
[62] Kwon, Y.J., Shigematsu, I., Saito, N., Dissimilar friction stir welding between magnesium and aluminum alloys, Mater. Lett., 2008, 62, 3827-3829.

[63] Firouzdor, V. and Kou, S., Al-to-Mg friction stir welding: effect of material position, travel speed, and rotation speed, Metall. Mater. Trans. A, 2010, 41, 2914-2935.
[64] Sameer, M.D. and Birru, A.K., Mechanical and metallurgical properties of friction stir welded dissimilar joints of AZ91 magnesium alloy and AA 6082–T6 aluminium alloy, J. Magnesium Alloys, 2019, 7 (2), 264-271.
[65] Küçükömeroğlu, T., Aktarer, S.M., İpekoğlu, G., Çam, G., Mechanical properties of friction stir welded St 37 and St 44 steel joints, Materials Testing, 2018, 60 (12), 1163-1170.
[66] İpekoğlu, G., Küçükömeroğlu, T., Aktarer, S.M., et al., Investigation of microstructure and mechanical properties of friction stir welded dissimilar St37/St52 joints, Mater. Research Express, 2019, 6 (4), 046537.
[67] Jafarzadegan, M., Feng, A.H., Abdollah-Zadeh, A., et al., Microstructural characterization in dissimilar friction stir welding between 304 stainless steel and st37 steel, Mater. Charact., 2012, 74, 28-41.
[68] Logan, B.P., Toumpis, A.I., Galloway, A.M., et al., Dissimilar friction stir welding of duplex stainless steel to low alloy structural steel, Sci. Technol. Weld. Joining, 2016, 21, 11-19.
[69] He, B., Cui, L., Wang, D., et al., The metallurgical bonding and high temperature tensile behaviors of 9Cr-1W steel and 316L steel dissimilar joint by friction stir welding, J. Manuf. Processes, 2019, 44, 241-251.
[70] İpekoğlu, G., Küçükömeroğlu, T., Aktarer, S.M., et al., Sürtünme karıştırma kaynağıyla birleştirilen St37/St52 levhaların mikroyapı karakterizasyonu ve mekanik özellikleri, Fen ve Müh. Dergisi, Dokuz Eylül Üniv., 2018, 20 (59), 471-480.
[71] Mehta, K.P., Carlone, P., Astarita, A., et al., Conventional and cooling assisted friction stir welding of AA6061 and AZ31B alloys, Mater. Sci. Eng. A, 2019, 759, 252-261.
[72] Zhao, Y., Lu, Z., Yan, K., Huang, L., Microstructural characterizations and mechanical properties in underwater friction stir welding of aluminum and magnesium dissimilar alloys, Mater. Des., 2015, 65, 675-681.
[73] Zhao, Y., Jiang, S., Yang, S., et al., Influence of cooling conditions on joint properties and microstructures of aluminum and magnesium dissimilar alloys by friction stir welding, Int. J. Adv. Manuf. Technol., 2016, 83, 673-679.
[74] Liu, Z., Meng, X., Ji, S., et al., Improving tensile properties of Al/Mg joint by smashing intermetallic compounds via ultrasonic-assisted stationary shoulder friction stir welding, J. Manuf. Processes, 2018, 31, 552-559.
[75] Ji, S., Meng, X., Liu, Z., et al., Dissimilar friction stir welding of 6061 aluminum alloy and AZ31 magnesium alloy assisted with ultrasonic, Mater. Lett., 2017, 201, 173-176.
[76] Lv, X., Wu, C., Yang, C., Padhy, G.K., Weld microstructure and mechanical properties in ultrasonic enhanced friction stir welding of Al alloy to Mg alloy, J. Mater. Process. Technol., 2018, 254, 145-157.
[77] Jiang, X.Q., Liu, Y.Y., Yuan, T., et al., Enhanced mechanical properties of dissimilar Al and Mg alloys fabricated by pulse current assisted friction stir welding, J. Manuf. Proces., 2022, 76, 123-137.
[78] Patrick, M.M., Akinlabi, E., Makhatha, M.E., 'Microstructure and electrical resistivity properties of copper and aluminium friction stir spot welds', 8th International Conference on Mechanical and Intelligent Manufacturing Technologies (ICMIMT), Feb. 2017, 42-47.
[79] Sun, Y., Fujii, H., Zhu, S., Guan, S., Flat friction stir spot welding of three 6061-T6 aluminum sheets, J. Mater. Process. Tech., 2019, 264, 414-421.
[80] De Castro, C.C., Shen, J., Plaine, A.H., et al., Tool wear mechanisms and effects on refill friction stir spot welding of AA2198-T8 sheets, J. Mater. Res. Technol., 2022, 20, 857-866.
[81] Boldsaikhan, E., Fukada, S., Fujimoto, M., et al., Refill friction stir spot welding of surface-treated aerospace aluminum alloys with faying-surface sealant, J. Manuf. Process., 2019, 42, 113-120.
[82] Derlatka, A. and Lacki, P., Experimental study and numerical simulation of cellular I-beam manufactured using refill friction stir spot welding technology, Thin–Walled Structures, 2024, 200, 111890.
[83] Gera, D., Fu, B.-L., Suhuddin, U.F.H.R., et al., Microstructure, mechanical and functional properties of refill friction stir spot welds on multilayered aluminum foils for battery application, Journal of Materials Research and Technology, 2021, 13, 2272-2286.
[84] Kim, D.-J., Baek, S.-Y., Nishijima, M., et al., Toward defect-less and minimized work-hardening loss implementation of Al alloy/high-purity Cu dissimilar lap joints by refill friction stir spot welding for battery tab-to-busbar applications, Materials Science & Engineering A, 2024, 892, 146089.
[85] Wynne, B.P., Threadgill, P.L., Davies, P.S., et al., Microstructure and texture in static shoulder friction stir welds, In Proceedings of the 7th International Friction Stir Welding Symposium; TWI, Awaji Island, Japan, 2008, pp. 1-8.
[86] Russell, M.J. and Blignault, C., In Proceedings of the Proc 6th Int. Symp. on Friction Stir Welding; P L Threadgill, Ed., TWI, Saint Sauveur, Quebec, Canada, 2007.
[87] Wu, H., Chen, Y., Strong, D., Prangnell, P., Stationary shoulder FSW for joining high strength aluminum alloys, J. Mater. Process. Tech., 2015, 221, 187-196.
[88] Russell, M.J., Threadgill, P.L., Thomas, M.J., Wynne, B.P., Static Shoulder Friction Stir Welding of Ti-6Al-4V: Process and Evaluation, In Proceedings of the 11th World Conference on Titanium (Ti-2007), (JIMIC - 5); Kyoto, Japan, 2007.
[89] Ahmed, M.M.Z., Wynne, B.P., Rainforth, W.M., Threadgill, P.L., Through-thickness crystallographic texture of stationary shoulder friction stir welded aluminium. Scr. Mater., 2011, 64, 45-48.
[90] İpekoğlu, G. and Çam, G., Formation of weld defects in cold metal transfer arc welded 7075-T6 plates and its effect on joint performance, IOP Conf. Series: Materials Science and Engineering, 2019, 629, 012007.
[91] Çam, G., Prospects of producing aluminum parts by wire arc additive manufacturing (WAAM), Materials Today: Proceedings, 2022, 62(1), 77-85.
[92] Çam, G. and Günen, A., Challenges and opportunities in the production of magnesium parts by directed energy deposition processes, Journal of Magnesium and Alloys, 2024, 12, 1663-1686.

[93] Güler, S., Serindağ, H.T., Çam, G., Tel ark eklemeli imalat: Son gelişmeler ve değerlendirmeler, TMMOB Makina Mühendisleri Odası, Kaynak Teknolojisi 12. Ulusal Kongre ve Sergisi (KAYKON 2021), 19-20 Kasım 2021, Ankara, S. 9-40.
[94] Çam, G., Ventzke, V., dos Santos, J.F., et al., Characterization of laser and electron beam welded Al-alloys, Prakt. Metallogr., 1999, 36 (2), 59-89.
[95] Çam, G., Koçak, M., Dobi, D., et al., Fracture behaviour of diffusion bonded bimaterial Ti-Al joints, Sci. Technol. Weld. Join., 1997, 2 (3), 95-101.
[96] Çam, G., Sürtünme karıştırma kaynağındaki gelişmeler, TMMOB Makina Mühendisleri Odası, Kaynak Teknolojisi IV. Ulusal Kongre ve Sergisi, 24-26 Ekim 2003, Kocaeli, S. 47-64.
[97] Çam, G., Sürtünme karıştırma kaynağı ve uygulamaları, 9. Malzeme Sempozyumu Bildiriler Kitabı, 8-10 Mayıs 2002, Pamukkale Üniversitesi, Denizli, 2002, S. 450-458.
[98] Sun, G.D., Zhou, L., Liu, Y.N., et al., Microstructure characterization and evaluation of mechanical properties in 2A97 aluminum-lithium alloys welded by stationary shoulder friction stir welding, Journal of Materials Research and Technology, 2022, 16, 416-432.
[99] Sen, M. and Puri, A.B., Formation of intermetallic compounds (IMCs) in FSW of aluminum and magnesium alloys (Al/Mg alloys) - A review, Materials Today Communications, 2022, 33, 105017.
[100] Song, Q., Wang, H., Ji, S., et al., Improving joint quality of hybrid friction stir welded Al/Mg dissimilar alloys by RBFNN-GWO system, J. Manuf. Process., 2020, 59, 750-759.
[101] Hu, W., Ma, Z., Ji, S., et al., Improving the mechanical property of dissimilar Al/Mg hybrid friction stir welding joint by PIO-ANN, J. Mater. Sci. Technol., 2020, 53, 41-52.
[102] You, J.-Q., Zhao, Y.-Q., Dong, C.-L., Su, Y.-H., Improving the microstructure and mechanical properties of Al-Cu dissimilar joints by ultrasonic dynamic-stationary shoulder friction stir welding, Journal of Materials Processing Tech., 2023, 311, 117812.
[103] Hammad, A.S., Ahmed, M.M.Z., Lu, H., et al., An investigation on mechanical and microstructural evolution of stationary shoulder friction stir welded aluminum alloy AA7075-T651, Proc. Inst. Mech. Eng. Part C J. Mech. Eng. Sci., 2022, 236, 6665-6676.
[104] Barbini, A., Carstensen, J., dos Santos, J.F., Influence of a non-rotating shoulder on heat generation, microstructure and mechanical properties of dissimilar AA2024 / AA7050 FSW joints, J. Mater. Sci. Technol., 2018, 34, 119-127.
[105] Li, D., Yang, X., Cui, L., et al., Investigation of stationary shoulder friction stir welding of aluminum alloy 7075-T651, J. Mater. Process. Tech., 2015, 222, 391-398.
[106] Sun, T., Roy, M.J., Strong, D., et al., Weld zone and residual stress development in AA7050 stationary shoulder friction stir T-joint weld, J. Mater. Process. Tech., 2019, 263, 256-265.
[107] Sun, Z., Yang, X., Li, D., Cui, L., The local strength and toughness for stationary shoulder friction stir weld on AA6061-T6 alloy, Mater. Charact., 2016, 111, 114-121.
[108] Ji, S.D., Meng, X.C., Liu, J.G., et al., Formation and mechanical properties of stationary shoulder friction stir welded 6005A-T6 aluminum alloy, Mater. Des., 2014, 62, 113-117.
[109] Threadgill, P.L., Ahmed, M.M.Z., Martin, J.P., et al., The use of bobbin tools for friction stir welding of aluminium alloys, Mater. Sci. Forum, 2010, 642, 1179-1184.
[110] Wang, F.F., Li, W.Y., Shen, J., et al., Effect of tool rotational speed on the microstructure and mechanical properties of bobbin tool friction stir welding of Al-Li alloy, Mater. Des., 2015, 86, 933-940.
[111] Wang, G.Q., Zhao, Y.H., Tang, Y.Y., Research progress of bobbin tool friction stir welding of aluminum alloys: A review, Acta Metall. Sin. (English Lett.), 2020, 33 (1), 13-29.
[112] Xu, W.F., Luo, Y.X., Fu, M.W., Microstructure evolution in the conventional single side and bobbin tool friction stir welding of thick rolled 7085-T7452 aluminum alloy, Mater. Charact., 2018, 138, 48-55.
[113] Xu, W.F., Luo, Y.X., Zhang, W., Fu, M.W., Comparative study on local and global mechanical properties of bobbin tool and conventional friction stir welded 7085-T7452 aluminum thick plate, J. Mater. Sci. Technol., 2018, 34, 173-184.
[114] Yang, C., Ni, D.R., Xue, P., et al., A comparative research on bobbin tool and conventional friction stir welding of Al-Mg-Si alloy plates, Mater. Charact., 2018, 145, 20-28.
[115] Lohwasser, D., Friction stir welding of aerospace alloys, In Proceedings of the Proc. 4th Int. Symp. on 'Friction stir welding; TWI, Park City, UT, USA, 2003; Vol. 48, pp. 37-46.
[116] Ahmed, M.M.Z., Habba, M.I.A., El-Sayed Seleman, M.M., et al., Bobbin tool friction stir welding of aluminum thick lap joints' properties, Materials, 2021, 14 (16), 4584.
[117] Li, G.-H., Gao, S.-K., Luo, S.-F., et al., Tailoring macrostructure and texture in bobbin-tool friction stir weld via manipulation of deformation behaviour of plasticised metal during welding enabled by modifying tool profile, International Journal of Machine Tools & Manufacture, 2024, 201, 104198.
[118] Russell, M.J., Nunn, M.E., Martin, J., Recent developments in the stationary shoulder FSW of titanium alloys. In: Proceedings of Seventh Int. Symp. on Friction Stir Welding. 2008, TWI, Japan.
[119] Goebel, J., Reimann, M., Norman, A., dos Santos, J.F., Semi-stationary shoulder bobbin tool friction stir welding of AA2198-T851, J. Mater. Process. Technol., 2017, 245, 37-45.
[120] Scupin, P., Semi-stationary shoulder bobbin tool (S3BT): A new approach in high speed friction stir welding, Ph.D. Thesis, Helmholtz-Zentrum Geesthacht, Germany, 2015.
[121] Li, G.-H., Chen, T., Fu, B.-L., et al., Semi-stationary shoulder bobbin-tool: A new approach in tailoring macrostructure and mechanical properties of bobbin-tool friction stir welds in magnesium alloy, Journal of Materials Processing Tech., 2023, 317, 117984.